



UNIVERSITY OF
LIVERPOOL

Raman spectroscopy of molecular electronic junctions

Thesis submitted in accordance with the requirements of the University of Liverpool for the degree of Doctor of Philosophy by

Nungnit Wattanavichean

October 2016

Department of Chemistry

University of Liverpool

Abstract

Molecular Electronics uses molecules sandwiched between two metals as a model system to create tailored solutions for applications such as energy harvesting and sensing. Electrons tunnelling across such a junction are affected by the properties of the molecule itself as well as the interaction between metal and molecule. In particular, charge transport is known to couple to molecular vibrations, which can act both to dissipate energy as well as increase conductance. This thesis therefore applies in-situ vibrational spectroscopies, surface-enhanced Raman scattering and vibrational sum frequency generation, to investigate molecular junctions.

As a model system, 4-mercaptopyridine sandwiched between a gold surface and an electrochemically deposited second metal layer is used. Four aspects are studied in detail in this thesis. Chapter 3 presents a detailed study of surface enhanced Raman spectra of 4-mercaptopyridine on gold. All experimental vibrational modes are assigned and related to the symmetry of the adsorbed molecule with the help of density functional calculations. In particular, the effect of hydrogen bonding on the ring breathing modes of adsorbed mercaptopyridine is revealed for the first time. In chapter 4, surface-enhanced Raman spectroscopy is used to identify a spectroscopic signature of a successfully formed metal-molecule-metal junction after electrochemical deposition of a transition metal layer. Chapter 5 then addresses the use of surface-enhanced Raman spectroscopy to identify charge transfer states of 4-mercaptopyridine by changing bias potential and excitation wavelength. A charge transfer state is found for protonated 4-mercaptopyridine at about 1.7 eV above the Fermi level, while the corresponding state for unprotonated 4-mercaptopyridine must lie at least 0.8 eV higher. Chapter 6 then explores the use of ultrafast vibrational sum frequency generation. The pyridine ring stretching modes are detected and metallisation of the 4-mercaptopyridine layer is seen to decrease the local order of the molecular layer. The influence of the mercaptopyridine charge transfer state can be seen in ultrafast pump - sum frequency probe spectroscopy of the gold substrate. This opens the prospect of investigating coupling between molecular vibrations and charge transfer in these junctions on a timescale of a picosecond or less. Keywords: Raman spectroscopy, 4-mercaptopyridine, Metal-molecule-metal junctions

Acknowledgements

Firstly, I would like to thank my family and friends in Thailand for their supports and encouragements over the four years as well as Mahidol and Liverpool university for funding.

Thanks to all my friends in Liverpool who decorate my PhD life to be such an unforgettable time in my life. With their friendships and supports, I found everything here is lots of fun and impressive. It is unbelievable that I have met that many true friends here.

Thanks to all my friends in chemistry in both Chemistry and Physics departments. In particular, Sergio and Takuma who gave me some lectures about laser and molecular electronic states at my beginning state of PhD. Thanks for Shah who always talk to me as well as to made a lot of discussions about our experiments together. Thanks to Bob and Wei for all of suggestions about electrochemistry. Thanks to Iain and Laura to any advises in Raman spectroscopy. Thanks to Sam who help me about nanoparticle synthesis. Thanks to Matthew and Thanchanok who allowed me to use their labs occasionally. I also would like to thanks to all master student who did join part of my project, Rachel, Cintya, and Lisa.

I would like to express my gratitude to my secondary supervisor, Prof. Richard Nichols who gave me tons of great suggestions, which always work!!! I really appreciate his offer to let me be a part of his electrochemical lab for the last two years.

Lastly, but is the most important person is my super supervisor, Dr. Heike Arnolds who opens my eyes to the world of spectroscopy and molecular electronics. She always support and give many useful advises to me over my last four years here. Her suggestions not only for sorting out the problems for that particular point of time, but it also grows me up academically and makes me realise how 'scientific people' think. Day by day, I absorb that kind of 'culture' which makes me ready to an academic role in the near future as a lecturer in Thailand. In addition, she gave me opportunities to attend many conferences across Europe which broaden my horizons completely. Apart from the academic point of view, she always offer me the warm hospitality and generosity which make me feel the most comfortable to work with her. With all of these, I cannot agree more to acknowledge her as my 'super' supervisor. Thanks a lot, Heike.

Publications

1. *The influence of hydrogen bonding on the Raman spectra of 4-mercaptopyridine adsorbed on gold*

Nungnit Wattanavichean, Richard Nichols, Heike Arnolds, *in preparation*

2. *The vibrational signature of a molecular electronic junction*

Nungnit Wattanavichean, Richard Nichols, Heike Arnolds, *in preparation*

Contents

1	Introduction	20
1.1	Molecular electronics	20
1.2	Vibrational transition and relation to electron transfer	22
1.3	Gold	25
1.4	Self-assembled monolayers	26
1.5	4-Mercaptopyridine	27
1.6	Metallisation	28
1.7	Overview of this thesis	28
2	Experimental	30
2.1	Electrochemistry	30
2.1.1	Charge transfer at interfaces	30
2.1.2	Cyclic voltammetry	32
2.1.3	Surface reactions	33

2.2	Vibrational spectroscopy	35
2.2.1	Molecular vibration	35
2.2.2	Raman spectroscopy	38
2.2.3	Surface-enhanced Raman spectroscopy	41
2.2.4	Sum frequency generation	45
2.3	Experimental setup	48
2.3.1	Glassware cleaning	48
2.3.2	SERS measurement	48
2.3.3	Electrochemical characterisation	49
2.3.4	Gold nanoparticles and SHINs synthesis	52
2.3.5	Mercaptopyridine adsorption	52
2.3.6	Metallisation	53
3	Mercaptopyridine adsorption	54
3.1	Overview	54
3.2	Experimental	56
3.3	Adsorption of mercaptopyridine on gold surfaces	56
3.4	Surface-enhanced Raman spectroscopy of mercaptopyridine on gold	61
3.5	The influence of hydrogen bonding	72
4	Metallisation	82

4.1	Metallisation of self-assembled monolayers	82
4.2	Metal-molecule-metal junctions in confined spaces	86
4.3	Large-scale junctions	89
5	Electronic resonances in SERS	103
5.1	Probing electronic states by SERS	103
5.2	Experimental	105
5.3	Results	106
5.4	Discussion	113
6	SFG of 4-mercaptopyridine on gold	117
6.1	Introduction	117
6.2	Molecular vibrations and relation to electron transfer	117
6.3	SFG of 4MP on gold	119
6.4	Pump-probe	122
7	Conclusions and future work	125
8	Appendices	127
8.1	Spartan calculations	127
8.2	Electrochemistry of gold	128
8.3	Sulfur contamination upon pyS adsorption	131

8.4 SHINs	135
-----------------	-----

List of abbreviations

A.C.	Alternating Current
AFM	Atomic force microscopy
CT	Charge transfer
CV	Cyclic voltammogram
DFT	Density functional theory
DOS	Density of states
E_F	Fermi energy
EM	Enhancement mechanism
FTIR	Fourier transform infrared spectroscopy
HOMO	Highest occupied molecular orbital
IETS	Inelastic tunneling spectroscopy
IR	Infrared
LFIEF	Local field intensity enhancement factor
LUMO	Lowest unoccupied molecular orbital
ML	Monolayer
MMM	Metal-molecule-metal
PyS	4-Mercaptopyridine
PySSPy	4,4-dipyridyl disulfide
SAM	Self-assembled monolayer
SCE	Saturated calomel electrode
SERS	Surface-enhanced Raman spectroscopy
SFG	Sum frequency generation
SHE	Standard hydrogen electrode
SHINs	Shell-isolated gold nanoparticles
STM	Scanning tunneling microscopy
TERS	Tip enhanced Raman spectroscopy
UHV	Ultra high vacuum
XPS	X-ray photoelectron spectroscopy

List of Figures

1.1	Example of a molecular junction formed by 4,4'-bipyridine between a gold surface and a gold tip. The conductance changes with molecular configuration from a low value (left) to a high value (right).	21
1.2	Schematic illustration of the 1-step process electron tunneling mechanism (a) and the 2-step electron hopping mechanism (b) through molecular wire bridges sandwiched between two electrodes.	23
1.3	Illustration of how a self-assembled monolayer of thiols forms from solution on a gold surface.	27
1.4	4-mercaptopyridine.	27
2.1	Models of the electric double layer: Helmholtz, Gouy-Chapman, and Stern. . . .	31
2.2	(A) an electrical potential applied to a metal increases or decreases the Fermi level. (B) A molecule can be reduced if the potential shifts the Fermi level enough to transfer electrons to the LUMO.	32
2.3	The typical voltammograms for a reversible electron transfer reaction at different scan rates.	33
2.4	Voltammogram for an ideal surface reaction of A to B.	34

2.5	Cyclic voltammogram showing first cycle of oxidation (1100-1400 mV) and reduction (850 mV) of a freshly annealed polycrystalline gold electrode in 0.1 M H_2SO_4 , scan rate is 50 mV/s and gold geometric surface area is $2.5 \times 10^{-5} \text{ m}^2$	35
2.6	Common terms used to describe molecular vibrations	36
2.7	Symmetry elements of pyridine - the two mirror planes are shown shaded in blue and pink and the two-fold axis is along Z.	37
2.8	Electronic transitions in Rayleigh and Raman scattering	39
2.9	A plasmon is a local electron density oscillation.	42
2.10	Schematic illustration of resonant Raman transitions in an adsorbed molecule. (A) molecule-to-metal, (B) metal-to-molecule, and (C) molecule-to-molecule.	44
2.11	Image dipole created into a metal surface. E_0 is the external field and E_{ind} is the induced field by the image dipole at the location of the original dipole.	45
2.12	The effect of a femtosecond laser pulse on the electron distribution at a metal surface. Nascent electrons are found up to 100 fs after the pulse, and then form a hot electron bath, which equilibrates with the metal lattice on a timescale of 1 ps. The hot lattice cools down on a timescale of 100 ps.	47
2.13	Schematic setup of a Raman spectrometer. Light from laser (black) is focused onto a sample by a lens or microscope objective. The Raman shifted light (red) is collected by the same lens, passes through a dichroic beamsplitter (reflects only the laser, transmits other wavelengths) and further filters and is detected in a grating spectrometer with CCD.	49
2.14	SERS background intensity change during electrochemical roughening process of gold polycrystalline foil (A) and a comparison of SERS background changes in various solutions (data intensity at 400 cm^{-1}) (B)	50

2.15	Electrochemical cleaning of Au-pyS surface by cyclic voltammetry in 0.1 M NaOH solution	51
2.16	Setup of three-electrodes electrochemical cell used in experiment	51
3.1	A typical metal-pyS-metal junction.	54
3.2	(A)(B) STM image of pyS on Au(111) showing domains and details of the ($5\times\sqrt{3}-R30^\circ$) structure (C) Calculated ($5\times\sqrt{3}-R30^\circ$) arrangement of pyS on Au(111) (D)(E) different orientations of adsorbed pyS: upright (C_{2v} symmetry; Au-S-C plane perpendicular to ring plane and surface plane; Au-S-C plane parallel to ring plane and perpendicular to surface plane (both C_s symmetry)).	57
3.3	CV of the double layer region of a polycrystalline gold disc (encased) electrode without (black) and with adsorbed pyS (red) in 0.1 M H_2SO_4 , scan rate 50 mV/s.	58
3.4	Reductive desorption of pyS from an encased polycrystalline gold electrode in 0.1 M NaOH from pyS and pySSpy adsorption, scan rate 50 mV/s.	60
3.5	Raman spectra of crystalline and adsorbed pyS on Au with the main modes assigned.	61
3.6	Comparison between a typical adsorbed spectrum and a DFT calculation of pyS (red) and pyS- H^+ (blue) bound to a Au atom. The background is coloured according to the symmetry of the vibrational modes.	64
3.7	Raman spectra of typical Au-pyS and exceptional conditions, (eg. double-ended link and surface contamination.	70
3.8	A rough gold surface might lead to pyS binding to gold with both the thiol and the nitrogen lone pair.	71
3.9	SERS spectra of pyS adsorbed at a variety of gold surfaces - (A) rough, (B) gold nanoparticles linked to flat gold with a dithiol, (C) in pinholes of SHIN particles or (D) adsorbed on flat gold with a layer of bare gold nanoparticles above.	72

3.10	SERS spectra of Au-pyS in aqueous solution, pH adjusted with H ₂ SO ₄ or NaOH.	73
3.11	Thiol-thione tautomerism of pyS and protonation at low pH.	74
3.12	SERS spectra acquired in-situ during adsorption of 1mM pyS.	75
3.13	SERS spectral change with adsorption period.	76
3.14	Dependence of ring breathing and stretching frequencies on H-bond distance from simulated species.	77
3.15	SERS intensity ratio of (A) 988 cm ⁻¹ , 1002 cm ⁻¹ , and 1017 cm ⁻¹ to 1093 cm ⁻¹ (trigonal ring deformation and (B) 1575 cm ⁻¹ to 1609 cm ⁻¹	78
3.16	SERS spectra of Au-pyS in superacid solution at ring breathing region.	80
3.17	Frequency shifts in the ring breathing region (A) and ring stretching region (B) observed during sequential pH changed in 0.1 M H ₂ SO ₄ , phosphate buffer, milli-Q water, and 0.1 M NaOH. The spectra were taken after immersion in each solution for 3 min.	80
4.1	Metal-molecule-metal formation in SHIN pinholes. The blue trace shows a SER spectrum of mercaptopyridine adsorbed on a layer of SHINs dried on a silicon wafer. The red trace shows the same layer after complexation in PdSO ₄ solution and washing. Spectra are scaled relative to the trigonal ring deformation.	87
4.2	Calculated Raman spectra of deprotonated and protonated pyS adsorbed on Au-pyS and a Au-pyS-Au cation.	88
4.3	Cyclic voltammogram of Pd reduction in 0.1 M H ₂ SO ₄ for two different complexation periods of Au foil-pyS in Pd salt solution.	90

4.4	AFM image of surface topography and phase of Au-pyS (A,C) and Au/pyS/Rh (B,D). Measurement conducted in KFM mode, tip PPP NCH-Pt, fq 160 kHz. Image size $5\mu\text{m} \times 5\mu\text{m}$	92
4.5	Comparison of the SER spectra of successful Au-pyS-metal junctions formed for three different metals.	93
4.6	Identification of successful (A), unsuccessful (B) metallisation of a pyS-Au layer by Pd. (A) shows SER spectra with final reduction in 1 mM PdSO ₄ , (B) shows SER spectra with final reduction in 0.1 M H ₂ SO ₄ . (C) corresponding cyclic voltammograms of Pd reduction in Pd-containing solution and H ₂ SO ₄	95
4.7	Averaged normalised spectra of Au-pyS SAM, after complexation to Rh ions and after electrochemical reduction.	96
4.8	(A) Maps of the intensity of the trigonal ring deformation and background Raman scattering and of the peak ratio between ring breathing and trigonal ring deformation. Each pixel represents a $5 \times 5\mu\text{m}$ area. (B) Plot of peak intensity versus background intensity for each pixel, showing the wide range of field enhancement factors across the surface. (C) Plot of the peak ratio versus background intensity.	97
4.9	Correlation between two peak ratios in ring breathing and trigonal ring deformation regions which commonly used for local pH determination in literatures.	98
4.10	Correlation between two new peak ratios in ring breathing and trigonal ring deformation regions which justified by our assignment for complexation and metallisation of metal on pyS layer	99
4.11	Correlation between peak ratios in the trigonal ring deformation. The black dots show the relation between ratio after metallisation (y-axis) and ratio after complexation (x-axis), and the red dots show the relation between ratio after metallisation (y-axis) and ratio of pyS SAM (x-axis)	100

4.12	Ratio $1580\text{ cm}^{-1}/1620\text{ cm}^{-1}$ of Au-pyS, Au/pyS/Pd ion, and Au/pyS/Pd metal which was electrodeposited in Pd ion containing solution (black) and metal ion free solution (red).	101
5.1	Experimental scheme of SERS measurement of Au-pyS molecular electronic state.	105
5.2	Electrochemical cell and SERS setup for LUMO determination experiment	106
5.3	SERS spectra of Au-pyS as a function of applied potential. Background has been subtracted and peaks normalised by the background value at 800 cm^{-1} . Peaks are labelled with the Gardner notation introduced in Chapter 3	107
5.4	Change in the SERS background at 800 cm^{-1} for excitation at 785 nm and 633 nm during the potential scan (lines and markers) and after the potential is returned to + 600 mV (markers).	108
5.5	Spectra recorded before and after the potential scan at 600 mV vs Ag/AgCl. . .	109
5.6	Intensity changes of SERS peaks grouped by excitation-dependent and independent types. The Gardner labels refer back to 5.3	110
5.7	Potential dependent intensity of the ring breathing mode measured with 785 nm and 633 nm. The latter trace was shifted down by the difference in photon energies between the two Raman lasers.	111
5.8	The ratio between deprotonated and protonated C=C stretching peak intensities measured with both 785 nm and 633 nm excitation.	112
5.9	Stark frequency shifts of ring breathing and trigonal ring deformation modes measured with both 785 nm and 633 nm excitation. 633 nm data have been shifted by + 2.5 cm^{-1} to account for a difference in wavelength calibration.	115

6.1	4-mercaptopyridine LUMO (A) and HOMO (B) orbitals. The LUMO orbital lies across C=C, therefore if charge transfer occurs via the LUMO, it should couple to the C=C stretching vibration. On the other hand, the HOMO orbital has a node on the C=C bond, so transfer via the HOMO should not couple to the C=C vibration.	118
6.2	Sum frequency spectra of the C-H stretching region for a pyS SAM without and with Pd overlayer.	120
6.3	Comparison between SFG and SERS spectra of the C=C stretching region of pyS-Au. The thin line shows the intensity envelope of the IR probe pulse.	121
6.4	SFG spectrum of pyS-Au recorded at different infrared center wavelengths.	122
6.5	Transient reduction at 0 ps as a function of the SFG photon energy.	123
6.6	Change in the nonresonant background of a pyS-Au sample as a function of time delay between an 800 nm pump pulse and an SFG probe. Data points were acquired in sequence from red to blue, the step at 8 ps time delay is probably caused by a change in alignment during the scan.	124
8.1	Correlation plots compare our experiment to published papers	128
8.2	Cyclic voltammogram of a Au(111) bead crystal and polycrystalline gold foil in the region of the sulfuric acid phase transition.	129
8.3	Cyclic voltammogram of the reduction-oxidation region of gold foil before and after annealing.	130
8.4	Cyclic voltammogram of gold oxidation-reduction comparing between smooth gold foil and rough gold foil.	130
8.5	AFM of (A) Au(111) (1 micron x 1 micron) and (B) roughening gold polycrystalline (5 microns x 5 microns).	131

8.6	Cyclic voltammogram of pyS desorption from smooth gold encase electrode and rough gold foil.	132
8.7	Cyclic voltammogram of encased gold electrode soaked in Na ₂ S.	133
8.8	Cyclic voltammogram shows pyS desorption from encase gold electrode for various adsorption conditions.	134
8.9	Cyclic voltammogram of gold oxidation-reduction of encased gold electrode with different adsorption conditions.	135
8.10	The core-shell structure of SHINs and their absorbance spectrum.	135
8.11	Cyclic voltammogram of AuNPs, pinhole-SHINs, and pinhole-free SHINs.	136
8.12	SER spectra determining pinholes on SHINs.	137
8.13	SER spectra of contaminated SHINs.	137

List of Tables

2.1	Character table for C_{2v} symmetry group	38
3.1	The dominant vibrational modes of adsorbed mercaptopyridine and their typical frequencies	62
3.2	Symmetry changes of vibrational modes between C_{2v} and C_s molecular symmetry	66
3.3	Summary of all experimental and calculated pyS-Au Raman peaks, their Gardner and Wilson mode numbers and vibration pattern	67
4.1	Frequency comparison of key peaks of Au-pyS, Au-pySH ⁺ , and Au/pyS/Au junctions	89

Chapter 1

Introduction

1.1 Molecular electronics

Molecular electronics is defined as "a field of science that investigates the electronics and thermal transport properties of circuits in which individual molecules (or an assembly of them) are used as basic building blocks" [1].

In brief, molecular electronics was an assembly of a discrete number of molecular components designed to perform a specific function. One model of a molecular electronic junction is shown in Figure 1.1. The word molecular electronics was first mentioned back in the 1950s by von Hippel, surprisingly, as an aim for the US Air Force Molecular electronics conference. At that time, molecular electronics was envisaged as a silicon-based material, where its properties are determined by its inherent molecular structure. In the 1970s, the first detailed research in this area was conducted by a Swiss chemist named Hans Kuhn. He fabricated Langmuir-Blodgett films onto a metal electrode, which created a so-called "junction", and measured the junction conductivity. The first use of a molecule as an electronic component was in 1974 when Ari Aviram synthesized and modified a charge-transfer salt to operate as a traditional diode [2]. It was in 1997 when the first charge transfer experiment on a single molecule was performed by the groups of Mark Reed and James Tours [3]. They used the mechanically controllable break

junction (MCBJ) of a benzenedithiol molecule between a gold electrode and a retractable metal tip. Nowadays, molecular electronics is seen as a potential technology for future electronic circuits and devices for instance, wires, switches, memory and gain elements [4].

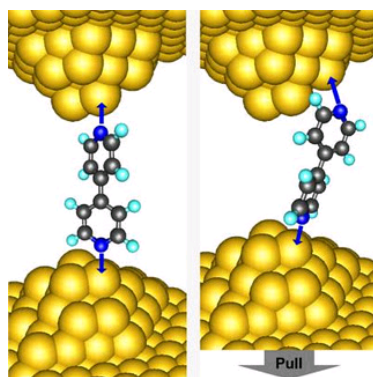


Figure 1.1: Example of a molecular junction formed by 4,4'-bipyridine between a gold surface and a gold tip. The conductance changes with molecular configuration from a low value (left) to a high value (right). Source: Reproduced with permission from [5]. ©Nature Publishing Group 2009.

In order to provide more specific properties for electronic elements, molecular electronics focuses on the behaviour of individual organic molecules or groups of molecules, as well as the precise three-dimensional positional control of individual atoms or molecules by using a "bottom-up" concept of self-assembly of elementary pieces to form a more complicated structure [6]. A large variety of molecules have been used for molecular electronics, ranging from simple alkanes and alkenes to aromatics, dye molecules such as porphyrins or redox-active species [4] and a wide range of methods has been used for self-assembly [7]. From the technological point of view, there are also good reasons to investigate the use of molecules as electrically active elements. In comparison with silicon-based technology, which is already a nanotechnology in the sense that the structure sizes are in the range of nanometers, molecular electronics could in principle offer the following major advantages. The first one is size. The reduced size of small molecules (between 1 and 10 nm) could lead to a higher packing density of devices with the subsequent advantages in cost, efficiency, and power dissipation. Imagine the first electronic computer which was made from 18000 valves, weighed 30 tons, occupied an entire room, and lasted an average of 5.6 h between

repairs [8] and compare it to a state-of-art computer in the present which is composed of more than 40 millions transistors [9], with numbers set to increase in the future. The miniaturization of electronic devices not only means smaller size and increasing power, but it also leads to the emergence of new technologies [10–12]. The second advantage is speed. Although most molecules are poorly conductive, good molecular wires could reduce the transit time of typical transistors ($\approx 10^{-14}$ s), thus reducing the time needed for a computational operation. The third advantage is assembly and recognition. One can exploit specific intermolecular interactions to form structures by nanoscale self-assembly. Molecular recognition can be used to modify electronic behavior, providing both switching and sensing capabilities on a single-molecule scale. The fourth advantage is new functionality. Special properties of molecules, like the existence of distinct stable geometric structures or isomers, could lead to new electronic functions that are not possible to implement in conventional solid state devices. The last advantage is synthetic design. By choice of composition and geometry, one can widely vary a molecule's charge transport, bonding, optical, and structural properties. The tools of molecular synthesis are highly developed. Of course, molecules have also obvious disadvantages such as instabilities at high temperatures. Moreover, the fabrication of reliable molecular junctions requires us to control matter at an unprecedented level, which can not only be difficult, but also slow and costly. The advantages described above however have been sufficient to motivate the exploration of molecule-based electronics [1].

Although molecular electronics has a bright role in the near future, moving it from a theoretical concept to a practical device is difficult. The history of science teaches us that the exploration of novel territories and phenomena leads to fascinating technological applications. However, new technology requires fundamental knowledge to realise it and this thesis sets out to provide such fundamental understanding.

1.2 Vibrational transition and relation to electron transfer

Since the beginning of molecular electronics, two different mechanisms of electron transfer have been discussed, the so-called 1-step and 2-step processes [13] as shown in Figure 1.2. In the

1-step transport, an electron tunnels elastically from one electrode to the other without any interaction with the molecule in the middle of the junction. In this case, the molecule just determines the width of the tunneling barrier. In the superexchange mechanism, the presence of empty molecular orbitals increases the efficiency of the tunneling, but the electron does not reside on the molecule [14]. Both mechanisms are referred to as coherent charge transport. In the 2-step process, or incoherent charge transport, the electron first hops onto the molecule and then transfers to the other electrode in a second step; for very long molecules the electron can even hop from one place within the molecule to the next. During this time, the electron can lose energy to molecular or environmental vibrations. This energy dissipation is affected by many factors including temperature, size and complexity of the molecular bridge [15,16]. The different

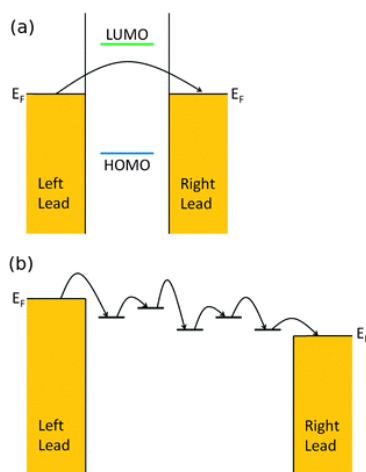


Figure 1.2: Schematic illustration of the 1-step process electron tunneling mechanism (a) and the 2-step electron hopping mechanism (b) through molecular wire bridges sandwiched between two electrodes. Source: Reproduced with permission from [13]. © PCCP Owner Societies 2015.

transport mechanisms can be distinguished by their dependence of tunneling current on bias voltage and the majority of experiments carried out on molecular junctions have used a scanning tunneling microscope.

A popular technique for example is the mechanically controlled break junction technique [17–21]. Here, the conductance of the molecule is measured as a scanning tunneling microscope tip pulls up a molecule on a surface and measures the current at a fixed bias until the junction

breaks. While the molecule is in the junction, the conductance takes a specific value, which is generally only determined by the nature of the bond to the surface and the nature of the molecule. When the conductance is plotted as a function of bias voltage, different characteristic behaviours can be seen, for example an "off-on-off" curve can be seen for redox-active molecules, where the "on" state corresponds to the redox potential of the molecule. For example for a molecular bridge containing a viologen moiety, it was shown that internal fluctuations and vibrations of the bridge strongly influence the conductance [22]. It has also been shown that the conductance of a molecular bridge can be changed by the presence of a solvent [23]. Both observations show that molecular and environmental vibrations play a key role in molecular electronics, but to access any direct information is difficult.

One approach has been inelastic tunneling spectroscopy. Once the bias voltage between a substrate and a conducting second electrode is above the threshold of a vibrational transition, the tunneling current increases by a small amount as there are now two channels available for tunneling - an elastic and an inelastic one. This process creates a small step-like increase in the current at a bias voltage corresponding to a molecular vibrational mode. Not all vibrations are seen in this mechanism, but generally only those where the vibrational coordinate is along the molecular bridge rather than perpendicular to it. A different approach, which is also suited to study single molecules, is tip-enhanced Raman spectroscopy [24], which gains sufficient sensitivity, because the small distance between a metal tip and a flat surface leads to a very large electromagnetic field enhancement of a laser beam illuminating the junction. This has been used to see the change of vibrational spectra as a function of bias voltage. For example, the appearance and disappearance of certain vibrational modes of dimercaptoazobenzene has been associated with charge transport across the molecular bridge [25].

However, neither of the methods described above are suited to accessing information on the dynamics of electron transfer across such junctions even though it underlies the resulting electrical behavior of the junction. There are no standard electrochemical measurements that can capture ultrafast processes such as charge transfer onto the molecular bridge, vibrational excitation and relaxation of the bridge, which occur on a timescale of femto- to picoseconds. Even novel ultrafast a.c. electrical measurements of molecular electronic junctions can only

probe charge transfer kinetics on the submicrosecond timescale and cannot capture the dynamic coupling between electronic and nuclear degrees of freedom [26, 27].

The initial idea for this thesis was to access charge transfer dynamics by optically exciting electrons in the bottom electrode with a femtosecond laser pulse. This pump pulse generates a range of excited electrons which can transfer onto the molecule within a much shorter time than can ever be achieved by voltammetry or a.c. electrical measurements. The effect of the excited electron on the molecular vibrations could then be probed with a time-delayed femtosecond probe pulse. By changing the time delay between pump and probe pulses, we might be able to follow the interaction between electrons and molecular vibrations in real time. The price to pay for the improvement in time resolution is sensitivity. The most sensitive vibrational spectroscopy which can operate on a femtosecond time scale is vibrational sum frequency generation, which still needs about 10^{12} molecules per cm^2 for a detectable signal [28]. As a result, the initial focus of this thesis was on how to make molecular electronic junctions on a cm^2 scale and how to spectroscopically detect whether a junction had been formed. The various ingredients for large scale junctions are therefore introduced next.

1.3 Gold

Gold is a transition metal with a filled 5d shell and a single valence electron in the 6s orbital. It behaves like a free electron metal, because the Fermi level is found within the s-band, where the electrons are highly delocalised [29, 30]. The d-band made of the much more localised 5d orbitals is found about 2 eV below the Fermi level. Gold is an attractive substrate for a number of reasons. Firstly, since gold is an inert metal, it will not form a stable oxide on its surface at room temperature and it resists atmospheric contamination [31–33]. Despite this general inertness, it can easily form Au-S bonds with thiols. Electrons can be easily excited into empty s-states above the Fermi level by photons in the near-IR or visible range. It can support relatively strong plasmon resonances, because this resonance can occur before damping by electronic transitions between the filled d-band and the empty portion of the s-band sets in, which makes it a useful

substrate for surface-enhanced Raman spectroscopy [29, 30]. Moreover, it is a widely studied metal, so its chemical, physical, and electronic properties are well-known and it can be easily obtained commercially in high purity.

1.4 Self-assembled monolayers

Since the 1980's, a technique called self-assembled monolayers (SAMs) has been widely used [34]. Self-assembly is the process of organic molecules in solution or gas phase spontaneously ordering on a solid surface [35]. The molecules are generally thought of as bifunctional containing an active terminal, which binds to a solid surface, and a head group which determines the chemical properties of the newly formed surface [36], shown in Figure 1.3. The most well-known SAMs on gold are alkanethiols which form a $\sqrt{3} \times \sqrt{3}$ R30 degree structure with the alkane chain tilted by 30 degrees from the surface normal [37–40]. The adsorption has two driving forces. The affinity of sulfur to gold with a bonding energy of about 190 kJ/mol, which is low compared to a typical C-C bond strength of 350 kJ/mol, but often strong enough to produce layers that are stable for weeks or months. The second driving force is lateral interactions between adsorbates, which can take the form of Van-der-Waals interactions, hydrogen bonds, hydrophobic forces or aromatic interactions. These lower the overall surface energy and maximise the interaction between molecules. The ideal SAM for this thesis has to fulfil three requirements. Firstly, there has to be a strong interaction between the active head group of the molecule and the metal surface. Secondly, the molecule has to easily form a monolayer which is well ordered and densely packed to avoid any electrical shorts between the top and the bottom electrode. Finally, the SAM needs to have a tail group which can chemically bind to a second electrode.

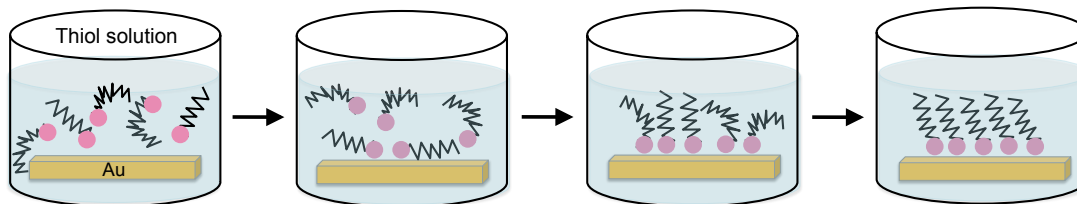


Figure 1.3: Illustration of how a self-assembled monolayer of thiols forms from solution on a gold surface.

1.5 4-Mercaptopyridine

This thesis uses 4-mercaptopyridine (pyS), an organosulfur compound C_5H_5N , to form a self-assembled monolayer as part of a molecular electronic junction. The main structure of pyS is a heterocyclic aromatic ring with a nitrogen atom at the fourth position on the ring and a thiol group attached to the opposite carbon (Figure 1.4). The thiol bond cleaves upon adsorption to metal surfaces and has a particularly strong affinity to gold [41]. The lone pair on the nitrogen can bind to other metals [42,43] and thus a molecular electronic junction is formed. The delocalised

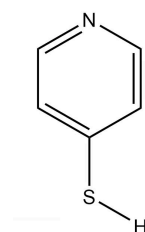


Figure 1.4: 4-mercaptopyridine.

electrons in the aromatic ring make it an excellent Raman scatterer and can enhance the binding between Au and thiol, which consequently results in the formation of compact and impermeable SAMs. Coordination to the nitrogen lone pair tunes the electron density on the aromatic ring which makes pyS generally interesting as an electron transfer promotor and pH sensor.

1.6 Metallisation

Metal-molecule-metal (MMM) junctions formed by self-assembly have raised much interest in recent years. Various junctions have been fabricated such as Pd/thiazole/Au [33], Pd/aminothiophenol/Au [44], Pd/(mercaptophenyl)pyridine/Au [45], and Pd/terpyridine/Au [46]. The breakthrough came from work in Kolb's group at the University of Ulm on the electrochemical deposition of a transition metal layer on top of pyS self-assembled monolayers [42, 43, 47], shown by cyclic voltammetry, scanning tunneling microscopy and photoelectron spectroscopy. Particular interest was raised by Pd overlayers with an altered density of states at the Fermi level [48]. Even though metal-pyS-gold junctions have been quite thoroughly studied by a range of methods including surface-enhanced Raman spectroscopy, to date no clear spectral signature of junction formation is known.

1.7 Overview of this thesis

This thesis focusses on gold/4-mercaptopyridine/metal junctions. Chapter 2 "Experimental" provides the background knowledge on characterisation techniques and junction preparation. The adsorption of mercaptopyridine on gold is discussed in chapter 3, "Mercaptopyridine adsorption". In this chapter, the vibrational modes of 4-mercaptopyridine detected by surface-enhanced Raman spectroscopy are assigned, typical spectra of clean and contaminated layers identified and the influence of hydrogen bonding discussed. Chapter 4, "Metallisation" describes how molecular junctions are made electrochemically and how success can be identified by Raman spectroscopy. In chapter 5, "Electronic resonances in SERS", charge transfer states are identified by Raman spectroscopy and the LUMO level of adsorbed mercaptopyridine is determined. Chapter 6, "Sum frequency generation of 4-mercaptopyridine on gold" shows the potential of nonlinear optical vibrational spectroscopy to detect the coupling between a vibrational resonance and laser-excited electrons. The "Future work" chapter proposes further opportunities to study electron transfer through molecular electronic junctions. Finally, the appendix collects background knowledge

relevant to this research and important experimental observations accumulated during my PhD.

Chapter 2

Experimental

2.1 Electrochemistry

2.1.1 Charge transfer at interfaces

Charge transfer is at the heart of electrochemistry and plays an important role in many areas of science, ranging from catalysis to biology. Charge transfer occurs at the interface between an electrode (often a metal) and species in solution, which undergo a general reaction of:



where *Ox* and *Red* refer to the oxidised and reduced forms of the species. As electrons are transferred from the metal to species in solution, a potential drop develops at the interface. At equilibrium, this is given by the Nernst equation

$$E = E^0 + \frac{RT}{nF} \ln\left(\frac{Ox}{Red}\right) \quad (2.2)$$

Several models have been proposed to describe how the potential changes with distance (Figure 2.1).

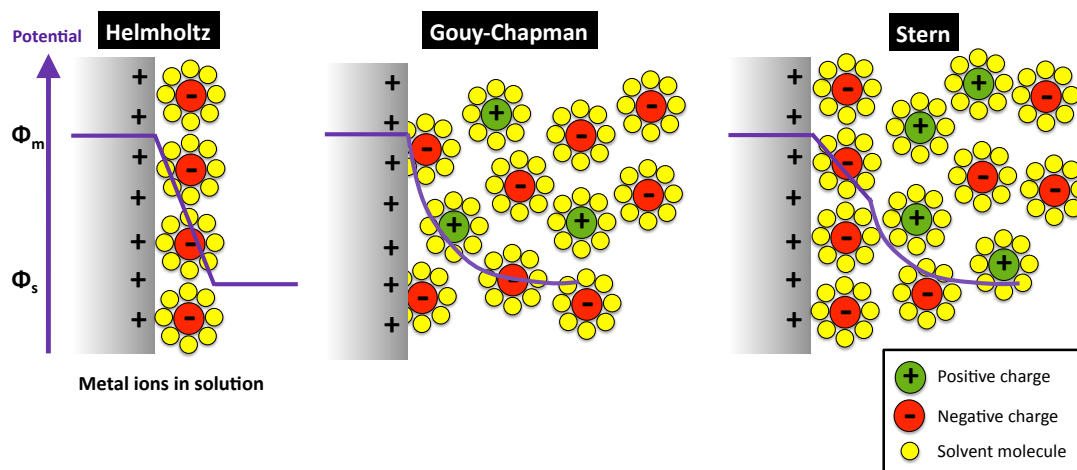


Figure 2.1: Models of the electric double layer: Helmholtz, Gouy-Chapman, and Stern.

In the simplest model by Helmholtz, the charge on the metal electrode is compensated by a layer of ions (including hydration shells). The potential changes linearly from inside the metal to within the solution, but on too short a length scale. To improve this, Gouy and Chapman developed a diffuse layer model, where the potential changes gradually. This model overestimates the capacitance of the interface, because the potential changes too slowly. Stern finally combined both models, since some ions will adsorb at the interface which leads to an initial linear change in potential. Beyond this inner layer, the potential changes more slowly in a diffuse solution of ions.

It is possible to control the kinetics of charge transfer by applying an external potential. The highest occupied state in a metal is the Fermi level and the application of a potential can shift the Fermi level up or down as shown schematically in Figure 2.2 A. If a reactant has a LUMO initially above E_F , such that electron transfer would be unfavorable, an external potential can shift the Fermi level up and allow electron transfer for reduction into the reactant LUMO (Figure 2.2 B).

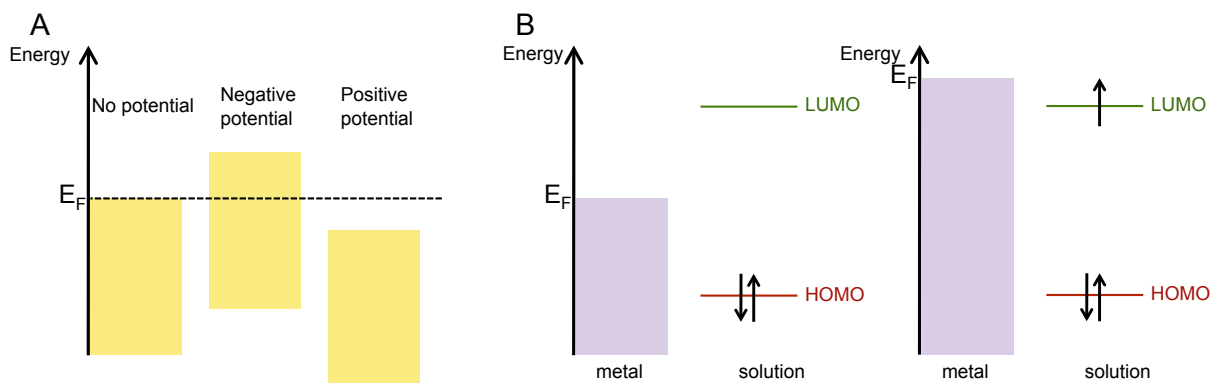


Figure 2.2: (A) an electrical potential applied to a metal increases or decreases the Fermi level. (B) A molecule can be reduced if the potential shifts the Fermi level enough to transfer electrons to the LUMO.

2.1.2 Cyclic voltammetry

One of the most popular electrochemical techniques for monitoring charge transfer is cyclic voltammetry. It uses the electrode of interest (called working electrode) and measures current flow to a counter electrode, while the electrode potential is changed linearly in time and cycles between a minimum and a maximum value. Since the potential drop at the interfaces of the working and counter electrodes depends on the concentration of species in solution, a third electrode, called reference electrode, is used, where the potential drop is constant. Only a very small current flows through the reference electrode in order to measure the potential of the working electrode in relation to the reference potential. Potentials are often expressed compared to the standard hydrogen electrode (SHE), a Pt electrode with the following half cell reaction:



The potential of the SHE is arbitrarily set at 0 V. Its absolute potential (equivalent to the work function) is 4.44 eV at 25°C. This thesis used both silver/silver chloride (Ag/AgCl) and mercury/mercurous sulfate (Hg/HgSO₄) as reference electrodes with potentials of +0.197 and +0.64 V compared to SHE, respectively. The counter electrodes used were both Au straight wire and Pt coiled wire electrodes. Their role is to supply a sufficient number of electrons and

therefore they should have a larger surface area than the working electrode.

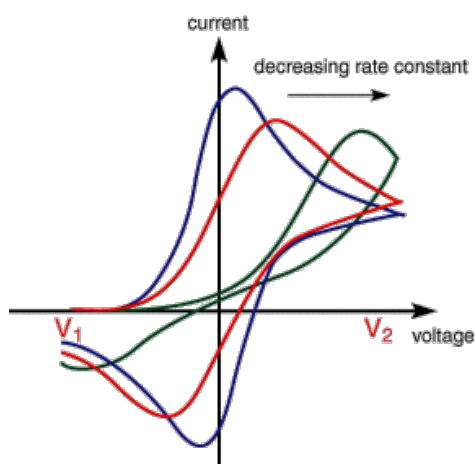


Figure 2.3: The typical voltammograms for a reversible electron transfer reaction at different scan rates [49].

Figure 2.3 shows a typical cyclic voltammogram for a reversible electron transfer to species in solution, eg. $\text{Fe}_{aq}^{3+} + e^- \rightleftharpoons \text{Fe}_{aq}^{2+}$. Where peaks occur depends on the scan rate, the electrolyte concentration and the diffusion coefficient. As the potential moves beyond the value where electron transfer is allowed, the reaction rate increases exponentially initially but then peaks as the region near the interface is depleted from reactants. Beyond the peak, the depletion region gradually becomes larger, so reactants take longer to get to the surface and the current drops. For a reversible reaction, the same will occur when the potential is swept in opposite direction. The peak potential is independent of the scan rate and the potential difference between oxidation and reduction peak at room temperature is given by

$$|E_p^{\text{Ox}} - E_p^{\text{Red}}| = \frac{59 \text{ mV}}{n}. \quad (2.4)$$

2.1.3 Surface reactions

Cyclic voltammograms of adsorbed species look very different (Figure 2.4). If A undergoes a reversible electron transfer to B and B stays adsorbed, then the shape of the CV is only determined by electron transfer, not by diffusion from solution. This produces symmetric peaks with forward

and reverse peaks occurring at the same potential. The area under the peak is a measurement of the surface coverage. This is true even for non-ideal reactions involving desorption and has been used here to determine both the effective area of the working electrode and the amount of mercaptopyridine adsorbed.

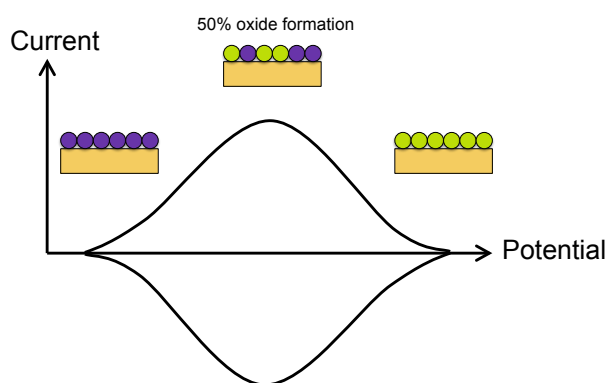


Figure 2.4: Voltammogram for an ideal surface reaction of A to B.

Figure 2.5 shows the typical polycrystalline gold oxidation and reduction peaks in 0.1 M H_2SO_4 . The polycrystalline gold oxidation potential is between 1.0 to 1.4 V vs SCE. This region actually varies depending on the presence of facets such as Au(111), Au(110), or Au(100). Here, it shows two distinct peaks around 1.03 V and 1.25 V vs SCE. These two peaks are characteristic for oxidation of Au(111), which is the most stable crystal face of gold [50]. The gold monolayer reduction peak is located around 0.85 V vs SCE. It normally appears as a strong sharp peak and the charge transferred during this reduction can be converted to the accessible surface area of the Au electrode. The standard value used for polycrystalline gold is $386 \mu\text{C}/\text{cm}^2$ [51]. This value assumes a single layer of gold oxide and the actual value therefore depends on the turning potential and the sweep rate, which both influence the thickness of the oxide layer formed.

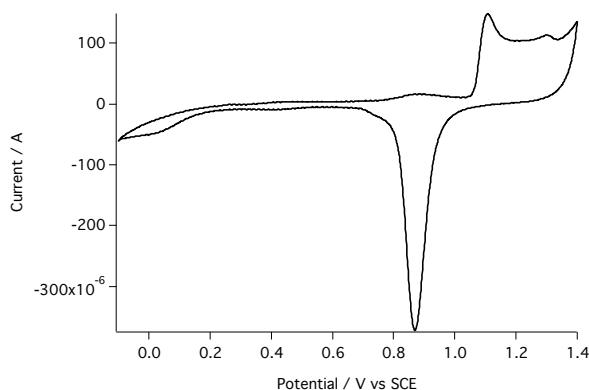


Figure 2.5: Cyclic voltammogram showing first cycle of oxidation (1100-1400 mV) and reduction (850 mV) of a freshly annealed polycrystalline gold electrode in 0.1 M H₂SO₄, scan rate is 50 mV/s and gold geometric surface area is $2.5 \times 10^{-5} \text{ m}^2$

2.2 Vibrational spectroscopy

2.2.1 Molecular vibration

Molecular vibration is a kind of nuclear motion in which an atom or group of atoms in the molecule is in periodic motion. The frequency of this periodic motion is known as vibrational frequency and typically ranges from $3 \times 10^{12} \text{ Hz}$ to $3 \times 10^{14} \text{ Hz}$, corresponding to wavenumbers from 100 cm^{-1} to 10000 cm^{-1} . In a molecule, energy levels are quantised and transitions between them are seen in spectroscopy. Vibrations are generally described as an anharmonic motion since the corresponding bond can break, which means transitions between all energy levels are allowed. In practice, mostly the transition between the vibrational ground state ($\nu=0$) and first excited state ($\nu=1$) is seen as the probability of occupying higher states is small for typical frequencies and temperatures. A molecule with N atoms will have $3N$ degrees of freedom to move. Translations account for 3 degrees of freedom and rotations for 2, respectively 3, for a linear or non-linear molecule. This leaves $3N-5$ respectively $3N-6$ degrees of freedom for vibrations of linear and non-linear molecules.

Vibrational motions are described by a variety of terms, such as stretching, bending, etc., which are summarized in Figure 2.6. Vibrations are commonly detected using either infrared

Vibration mode	Description	Molecular configuration
Stretching	Change in bond length	
Bending	Change in angle between two bonds	
Rocking	Change in angle between a group of atoms and rest of the molecule	
Wagging	Change in angle between the plane of a group of atoms and the rest of the molecule	
Twisting	Change in the angle between the planes of two groups of atoms	
Ring breathing	Characteristic vibration of an aromatic ring compressing and releasing	

Figure 2.6: Common terms used to describe molecular vibrations

or Raman spectroscopy. Each spectroscopy imposes its own selection rules - infrared detects a vibration if the vibration changes the dipole moment of the molecule while Raman requires a change in the polarisability. Which vibrational mode is seen in which spectroscopy can be deduced from the symmetry of the molecule and the symmetry of the vibrational motion. I will explain this for the example of a pyridine molecule, shown in Figure 2.7. The symmetry properties of pyridine are summarised in the notation C_{2v} - it possesses a twofold rotation axis and two mirror planes as shown in Figure 2.7.

There are four possible symmetry operations for this molecule, called E (identity), C_2

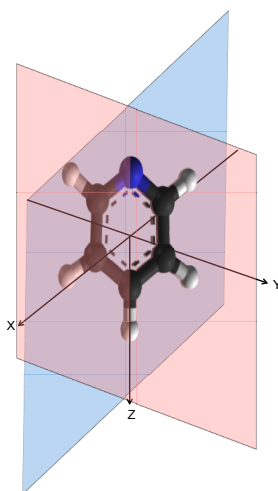


Figure 2.7: Symmetry elements of pyridine - the two mirror planes are shown shaded in blue and pink and the two-fold axis is along Z.

(rotation around the symmetry axis by 180°), $\sigma_v(xz)$ (mirror plane perpendicular to molecular plane) and $\sigma_v(yz)$ (mirror plane parallel to molecular plane).

In spectroscopy, the motions of C_{2v} molecule are normally described by a_1 , a_2 , b_1 , and b_2 modes. An a_1 vibration keeps all symmetry elements intact, for example the ring breathing mode or a C-H stretching mode where all C-H bonds move in unison. This type of motion is called totally symmetric. A b_1 vibration keeps the mirror plane perpendicular to the molecular plane, and is called an out-of-plane vibration. A b_2 vibration keeps the yz mirror plane and is called in-plane vibration. Finally, an a_2 motion breaks all symmetry elements in the molecule. These properties are summarised in table 2.1, where an entry of "1" means no change under this symmetry operation and "-1" means a change.

The table 2.1 contains two further columns which show whether a mode is infrared and/or Raman active. For example, a_1 vibrations lead to a dipole moment change in the z direction and are IR active. Raman activity corresponds to the response of the molecular electron cloud in one direction under the influence of an electric field in a different direction and is represented by a product such as z^2 or xy . For the example of pyridine, all vibrations are Raman active, while a_2 vibrations are not IR active.

Table 2.1: Character table for C_{2v} symmetry group

C_{2v}	E	C_2	$\sigma_v(xz)$	$\sigma_v(yz)$	linear	quadratic
a_1	1	1	1	1	z	x^2, y^2, z^2
a_2	1	1	-1	-1		xy
b_1	1	-1	1	-1	x	xz
b_2	1	-1	-1	1	y	yz

2.2.2 Raman spectroscopy

Raman scattering was discovered in India by Chandrasekhara Venkata Raman in the 1920s. Condensing sun light with the help of an 18 cm reflecting telescope, he could observe by eye that light scattered from many liquids contained wavelengths different from the light source [52]. First published in 1928 under the title "A new type of secondary radiation", it gained him the physics Nobel prize in 1930 [53]. We now call the effect Raman scattering. The new wavelengths observed arise from inelastic scattering of light, which exchanges a quantum of energy with vibrations in a molecule or solid.

Scattering is the process in which the incident photon is absorbed and as a consequence another photon is emitted, called scattered photon. If the incident and scattered photon have the same energy, scattering is elastic and called "Rayleigh scattering". Inelastic or Raman scattering occurs when the incident light causes transitions between vibrational/rotational levels of the molecule. This is illustrated in Figure 2.8.

After the molecule absorbs the incident photon, it is excited to a higher energy level which can be a virtual or a real electronically excited state. In the Stokes process, a molecule is excited from the vibrational ground state ($v = 0$) and returns to the vibrationally excited state ($v = 1$). The emitted photon has a lower energy or longer wavelength than the incident one. In the anti-Stokes process, the molecule is in the excited vibrational state ($v = 1$) in the first place and then relaxes to its ground state ($v = 0$). The emitted photon then has a higher energy

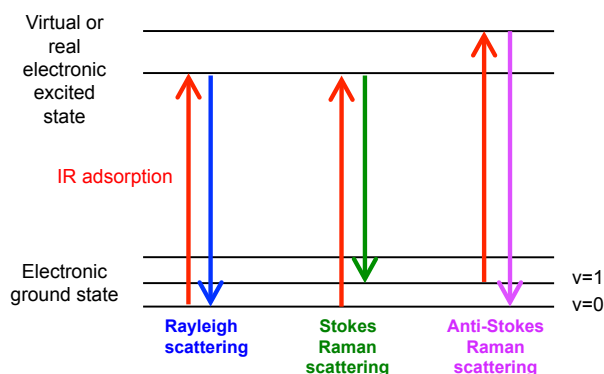


Figure 2.8: Electronic transitions in Rayleigh and Raman scattering

than the incident one. Anti-Stokes scattering is weaker than Stokes scattering because fewer molecules are in the excited state than in the ground state. The intensity ratio of anti-Stokes Raman scattering to Stokes Raman scattering is given by the Boltzmann factor: $\exp(-h\nu_v/k_B T)$, where $h\nu_v$ is the transition frequency between $v = 0$ and $v = 1$. The energy lost by the photons in the scattering process is called Raman shift, defined as

$$\Delta E_R = E_L - E_S, \quad (2.5)$$

where ΔE_R is the Raman shift and E_L and E_S are the energies of incident and scattered photons, respectively. According to the equation, the Stokes process gives a positive Raman shift, while the anti-Stokes process corresponds to a negative shift. The Raman shift is normally expressed in wavenumbers, cm^{-1} . The modulus of the Raman shift corresponds to the frequency of the vibrational mode which is involved in the scattering process. Not all vibrational modes are Raman active, a vibrational mode has to change the molecular polarisability. To explain this, we look at how the molecule interacts with light.

A molecule in an electric field becomes polarized and the induced dipole moment is given by

$$P = \alpha E, \quad (2.6)$$

where E is the electric field, in NC^{-1} or Vm^{-1} , and α is the polarizability, in m^3 . A beam of light of frequency ν is described by an oscillating field

$$E = E_0 \cos 2\pi\nu t \quad (2.7)$$

and thus the induced polarisation also oscillates:

$$P = \alpha E_0 \cos 2\pi\nu t. \quad (2.8)$$

This oscillating dipole is the source of the emitted Rayleigh scattered light. If the molecule carries out periodic motion which changes the polarisability, we can write

$$\alpha = \alpha_0 + \alpha' \cos 2\pi\nu_{vib}t. \quad (2.9)$$

The term α' is the rate of change of the molecular polarisability with the vibration:

$$\alpha' = \frac{\partial\alpha}{\partial q}. \quad (2.10)$$

If equations 2.9 and 2.10 are combined with equation 2.8, it results in

$$P = \alpha E = (\alpha_0 + \alpha' \cos 2\pi\nu_{vib}t) E_0 \cos 2\pi\nu t. \quad (2.11)$$

Since

$$\cos A \cdot \cos B = \frac{1}{2}[\cos(A + B) + \cos(A - B)]$$

we obtain

$$P = \alpha_0 E_0 \sin 2\pi\nu t + \frac{1}{2} \alpha' E_0 \cos 2\pi(\nu - \nu_{vib})t - \cos 2\pi(\nu + \nu_{vib})t \quad (2.12)$$

The first term is elastic Rayleigh scattering. The second is Stokes Raman scattering and the third is anti-Stokes Raman scattering [54]. Actually, the polarizability derivative is a tensor, in component form:

$$P_x = \alpha'_{xx} E_x + \alpha'_{xy} E_y + \alpha'_{xz} E_z \quad (2.13)$$

$$P_y = \alpha'_{yx} E_x + \alpha'_{yy} E_y + \alpha'_{yz} E_z \quad (2.14)$$

$$P_z = \alpha'_{zx} E_x + \alpha'_{zy} E_y + \alpha'_{zz} E_z \quad (2.15)$$

The tensor character of α' becomes important when we consider the symmetry of the molecule and surface-enhanced Raman scattering later. The intensity of the Raman scattered light, I_{RS} is often reported as a cross section,

$$I_{RS} = \sigma_{RS} \cdot I_0. \quad (2.16)$$

Here I_0 is the incoming flux of photons (photons $s^{-1}cm^{-1}$), and I_{RS} is the number of scattered photons per second. The efficiency of the Raman scattering process is averaged over all random orientations of the molecule. The Raman cross section (I_{RS}) has units of cm^2 and is proportional to the square of the polarizability derivative for the vibrational transition, $\alpha' = (\partial\alpha/\partial Q)_0$, and the fourth power of the scattering frequency (ω_S), $\sigma_{RS} = C\omega_S^4 |\alpha'_{mn}|^2$, where C is a numerical constant.

2.2.3 Surface-enhanced Raman spectroscopy

Raman scattering is a weak process. With a typical cross section of $10^{-29} cm^2$, it is 8 orders of magnitude weaker than infrared absorption and normally too weak to detect the typical $10^{14} - 10^{15}$ molecules/ cm^2 in a SAM. However, in 1974, Fleischmann *et al.* managed to detect the Raman spectrum of pyridine adsorbed at a roughened silver electrode, thinking that roughening would simply enhance the surface area and thus the signal [55]. Over several years, it became clear that the enhancement was caused by excitation of localised surface plasmons. The incident light induces an oscillation of metal electrons, which enhances both the incident and the scattered electric fields. This leads to an enhancement which is proportional to the fourth power of the electric field. The cross section of SERS is around $10^{-16} cm^2$, which is around a thousand times stronger than fluorescence. Silver and gold are the most frequently used substrates for SERS, as their surface plasmons are only weakly damped by interband transitions. Since the 1970s, SERS has progressed strongly and has been introduced to many scientific areas in physics, chemistry, biology, engineering, and all forms of nanoscience and nanotechnology [56, 57]. SERS can even be used as a tool for single-molecule detection, either on nanostructured surfaces or in the high field area between a metallic tip and a flat surface (Tip enhanced Raman Spectroscopy, TERS).

SERS selection rules

The surface enhancement is often described by the local field intensity enhancement factor (LFIEF), which represents the electromagnetic field intensity change on the surface,

$LFIEF(r) = |E(r)^2| / |E_0(r)^2|$. $E(r)$ is the electric field amplitude at point r and $E_0(r)$ is the intensity of incoming field at the same point [58].

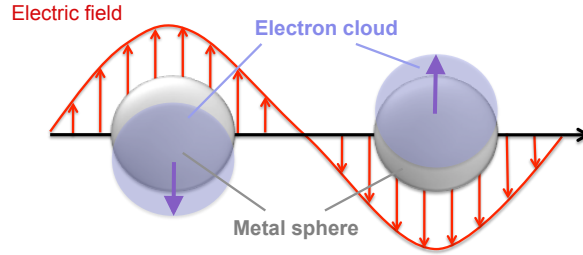


Figure 2.9: A plasmon is a local electron density oscillation. Source: Reprinted with permission from [59]. © American Chemical Society 2003.

Figure 2.9 shows how an incoming electric field excites an electron density oscillation on a metal sphere. This generates a local field parallel to the incoming one and the LFIEF is largest in radial direction and smallest in tangential direction of the sphere. Creighton derives the enhancement factors in radial and tangential direction as [60]

$$LFIEF_{rad} = \frac{(1 + 2g(\nu_0))^2}{3} \quad (2.17)$$

$$LFIEF_{tan} = \frac{(1 - 2g(\nu_0))^2}{3} \quad (2.18)$$

The function $g(\nu_0)$ is related to the dielectric constant ($\epsilon(\nu_0)$) of the metal and of the surrounding medium (ϵ_m);

$$g(\nu_0) = \frac{\epsilon(\nu_0) - \epsilon_m}{\epsilon(\nu_0) + 2\epsilon_m}. \quad (2.19)$$

At the plasmon resonance, $g(\nu_0) \gg 1$, so the radial LFIEF is about $4 \times$ larger than the tangential LFIEF. Far from resonance, $g(\nu_0) \approx 1$, and the tangential component is close to zero. The different enhancement of radial and tangential electric fields forms the basis of the selection rules of SERS. Returning to the example of a molecule with C_{2v} symmetry, the different Raman tensor components shown in eqn. 2.15 are enhanced to different degrees, depending on their symmetry (see table 2.1). In the totally symmetric class, we have α'_{zz} with

$$P_Z = \alpha'_{zz} E_Z \quad (2.20)$$

The incident field (E_z) is enhanced by $\approx \frac{4}{3}g(\nu_0)^2$. The scattered field which is re-radiated by the induced dipole (P_z) is enhanced by $\approx \frac{4}{3}g(\nu_S)^2$. The total enhancement is therefore $\frac{16}{9}g(\nu_0)^2g(\nu_S)^2$. For the symmetry classes b_1 and b_2 , we have

$$P_x = \alpha'_{xz}E_z \text{ and } P_y = \alpha'_{yz}E_z \quad (2.21)$$

with a total enhancement of $\frac{4}{9}g(\nu_0)^2g(\nu_S)^2$. Vibrations of a_2 symmetry with

$$P_x = \alpha'_{xy}E_y \quad (2.22)$$

only experience an enhancement of $\frac{1}{9}g(\nu_0)g(\nu_S)^2$. Therefore, one expects that in this case totally symmetric modes are enhanced 4x as much as (b_1, b_2) type modes, which are in turn enhanced 4x compared to a_2 modes. The discussion is similar for other orientations and symmetries and results in general surface selection rules for SERS. Since the symmetry of a mode is related to the local orientation of the molecule, the rule can be difficult to apply. For example, if the C_2 axis of a molecule with C_{2v} symmetry is tilted with respect to the direction, the local symmetry becomes C_S . Totally symmetric modes in C_S are those which had a_1 and b_1 symmetry in C_{2v} . The application of the selection rule is complicated by the existence of other enhancement mechanisms.

Chemical enhancement

Two further enhancement mechanisms exist at a surface, which are commonly referred to as chemical enhancement. The first type is a form of resonant Raman scattering where the exciting laser matches an electronic transition in the molecule. In the gas phase, this would be the HOMO to LUMO transition, but at a surface two further transitions are allowed. The laser can excite an electron from the Fermi level to the LUMO (metal-to-molecule charge transfer) or it can excite an electron from the HOMO to the Fermi level (molecule-to-metal charge transfer). These transitions are shown schematically in Figure 2.10. Since the Fermi level lies in between the HOMO and LUMO, resonance Raman scattering can occur at far lower energies than in the gas phase. The direction of charge transfer can be determined by applying a potential and shifting E_F with respect to the molecular orbitals [61].

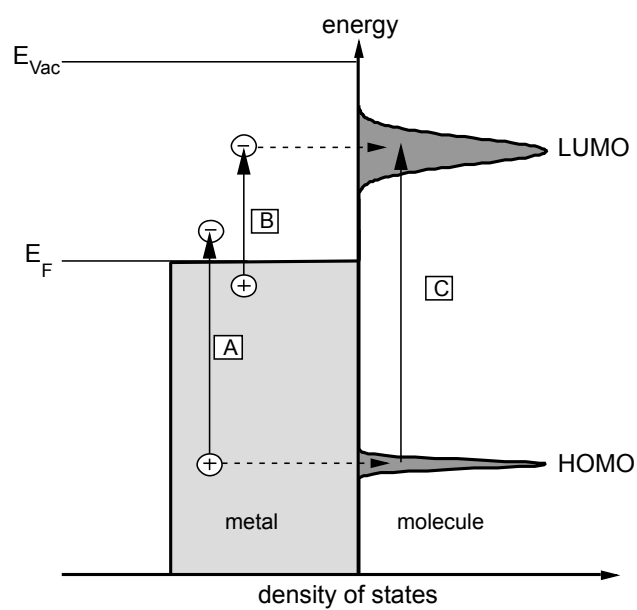


Figure 2.10: Schematic illustration of resonant Raman transitions in an adsorbed molecule. (A) molecule-to-metal, (B) metal-to-molecule, and (C) molecule-to-molecule. Source: Reprinted with permission from [62]. © Elsevier 2011.

A second chemical enhancement mechanism discussed in the literature is the interaction between an adsorbate and the conduction electrons of the metal. A molecular dipole close to a metal surface generates an image dipole as shown in Figure 2.11. This image dipole enhances the polarisability (α_0) of the adsorbate, depending on its distance (d) to the surface. The effective polarisability near the metal surface is then given by [63]

$$\alpha = \frac{\alpha_0}{1 - \frac{\alpha_0}{4\pi\epsilon_0(2d)^3}}. \quad (2.23)$$

When the distance between metal and molecule is small, the polarisability increases drastically. Therefore, the metal is a key for gaining polarisability for this mechanism, shown in Figure 2.11 [63].

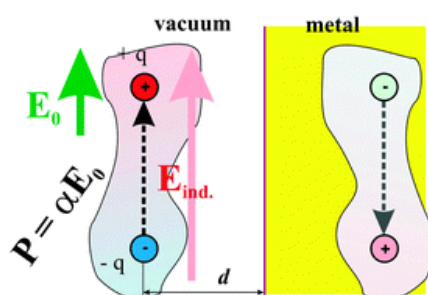


Figure 2.11: Image dipole created into a metal surface. E_0 is the external field and E_{ind} is the induced field by the image dipole at the location of the original dipole. Source: Reproduced with permission from [63] © PCCP Owner Societies.

An alternative model for how surface electrons enhance the Raman response was proposed by Zayak [64]. Certain vibrational modes of benzenethiol adsorbed on Au, such as the ring stretching and trigonal ring deformation, were found to induce large localised changes in the electron density near the Fermi level. This can also be understood as an increase in the polarisability as the vibration affects a larger electron cloud than that surrounding the molecule.

2.2.4 Sum frequency generation

One of the biggest challenges in surface science is the scarcity of molecules at the interface relative to large numbers in the bulk, and this results in poor sensitivity. Sum frequency generation (SFG)

offers intrinsic advantages in this regard. It is a nonlinear optical technique used to study the details of molecular structure, orientation and dynamics at surfaces and interfaces. The extremely high surface selectivity of the SFG process allows researchers to focus on a layer of a few atoms or molecules near the interface, without detecting the bulk media. The theory of SFG can be briefly outlined as follows. When light interacts with a medium without permanent polarization, the induced polarization in the the electric-dipole approximation is as follows [65]:

$$P = \varepsilon_0(\chi^{(1)} : E + \chi^{(2)} : EE + \dots) \quad (2.24)$$

Here, P is the polarization vector, E is the electric field vector, and $\chi^{(1)}$ and $\chi^{(2)}$ are the first- and second-order electric susceptibility tensors of the medium. The $\chi^{(1)}$ term is responsible for linear optical-processes such as Rayleigh and Raman scattering. Second and higher order effects are observed only when the medium is subjected to high electric fields from high intensity pulsed lasers. In an infrared-visible SFG experiments, the medium is simultaneously subjected to two intense electric fields, one in the IR and in the visible; then the induced second order polarization is as follows:

$$P = \varepsilon_0\chi^{(2)} : (E_{vis}E_{IR}) \quad (2.25)$$

In SFG, the molecule absorbs an infrared photon followed by an anti-Stokes Raman process. SFG is therefore related to Raman spectroscopy, with one important difference: while Raman is spontaneous, incoherent scattering, SFG is a coherent optical process in which each transition is driven by an optical field and the signal is emitted in a well-defined phase-matched direction [65]. This leads to much bigger signals generated from a surface, making even sub-monolayer coverages detectable [66]. The surface selectivity of SFG can be easily explained by thinking about the phase of the emitted light - a molecule pointing up at an interface will emit light that is 180° out of phase from a molecule pointing down. Therefore, a bulk medium (no net orientation of molecules) will lead to an overall zero signal, while an ordered interface leads to a large signal. It thus provides more information from an interface than pure infrared or Raman spectroscopy. The advantages of using SFG is that it can be applied in situ to all interfaces accessible by light, is nondestructive, and offers unprecedented time resolution when the exciting laser pulses are tens to hundreds of femtoseconds long [67].

In order to follow electron transfer in real time, SFG can be used in a pump-probe setup, where the femtosecond pump pulse excites electrons in the surface and the effect on vibrations is probed with a delayed pair of SFG probe pulses. As shown in Figure 2.12, after the metal surface is exposed to a short-pulse laser source, so-called nascent electrons are created above E_F up to the photon energy. Within 100 fs, they form an equilibrated hot electron bath, which then equilibrates with surface photons within ≈ 1 ps. In such a pump-probe experiment, changes in the vibrational spectrum within about 1 ps following the pump pulse can be attributed to the hot excited electrons, while a response at much longer delay times indicates just a thermal response [28].

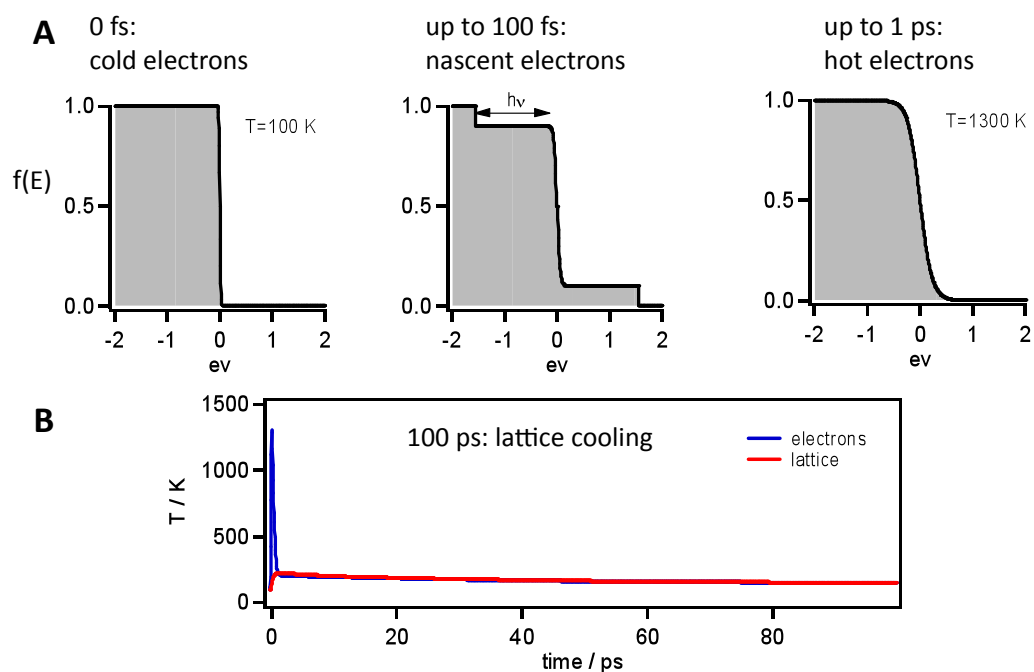


Figure 2.12: The effect of a femtosecond laser pulse on the electron distribution at a metal surface. Nascent electrons are found up to 100 fs after the pulse, and then form a hot electron bath, which equilibrates with the metal lattice on a timescale of 1 ps. The hot lattice cools down on a timescale of 100 ps.

2.3 Experimental setup

2.3.1 Glassware cleaning

All glassware was soaked in 70 °C Piranha solution (30 % H₂O₂ + 70 % H₂SO₄) for an hour to eliminate all organic residues. After cleaning, the glassware was rinsed with Milli Q water (18.2 MΩ, Merck Millipore, UK) and dried with nitrogen gas.

2.3.2 SERS measurement

Raman spectroscopy was carried out using either a Mini Ram II (B&W Tek, USA) with BWSpec software or a Renishaw inVia microscope with 50x objective. Figure 2.13(A) shows the schematic light path of both Raman spectrometers. The Mini RamII uses a 785 nm diode laser with maximum power of 300 mW. The Renishaw microscope employs both a 785 nm diode laser as well as a 633 nm HeNe laser with maximum powers of 71 mW and 4.5 mW respectively at the sample position. Most Raman spectra were obtained using a laser at 785 nm (Mini Ram II) and some experiments shown in chapters 4 and 5 used a 633 and 785 nm laser (Renishaw). The laser power of the Mini Ram was typically between 150 mW and 300 mW with a focal point diameter of 75 μm, corresponding to an intensity of $3.4 \times 10^7 \text{ Wm}^{-2}$. The microscope produced a spot size of 10 μm and typical power used was 0.4 mW, corresponding to $0.5 \times 10^7 \text{ Wm}^{-2}$. For SERS, spectra were acquired with a typical accumulation time of 30 s. SERS was measured both in air or in solution with the sample inside a quartz cuvette. For post data analysis of SERS spectra, the original spectra was processed with background correction by fitting the background with a polynomial, which is then subtracted to get only the peaks.

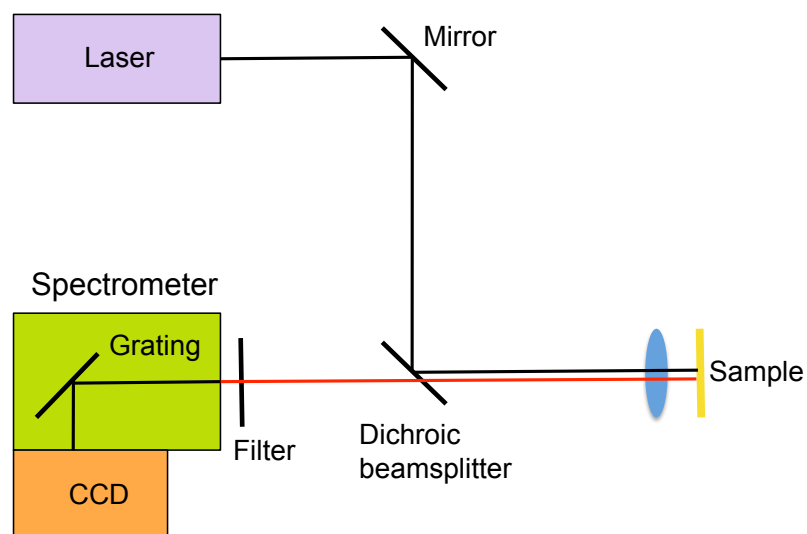


Figure 2.13: Schematic setup of a Raman spectrometer. Light from laser (black) is focused onto a sample by a lens or microscope objective. The Raman shifted light (red) is collected by the same lens, passes through a dichroic beamsplitter (reflects only the laser, transmits other wavelengths) and further filters and is detected in a grating spectrometer with CCD.

2.3.3 Electrochemical characterisation

Cyclic voltammetry was used in many aspects including cleaning, roughening, and characterization processes. In the initial stages of this work, I used a well known electrochemical roughening method with Cl^- -salt solution. The Cl^- ions form a Au^+Cl^- complex at positive potentials, and when the potential scan is reversed, Au is reduced and redeposited again on the gold electrode to make the gold surface rough [68]. Figure 2.14 B shows a comparison of the effect of roughening on Raman intensity using 0.1 M NaCl and KCl salt solutions. NaCl gave the better result after roughening for 100 cycles, scanning from -0.3 to +1.22 V at a scan rate of 500 mV/sec. However, this method is very time consuming and the SERS background intensity is not well maintained. SERS background intensity is used as an indicator because it related directly to peak signal intensity, since it is the product of electron-hole pair formation when the surface plasmon decays [69]. In some cases a sign of Cl^- contamination is seen in the form of a Cl-Au stretching vibration at 265 cm^{-1} (Figure 2.14 A- purple spectrum) [70]. The frequently observed peak around

553 cm^{-1} stems from gold oxide and could be diminished by running a gold reduction-oxidation cycle in 0.1 M H_2SO_4 . In the final stages of this work, an improved roughening procedure was

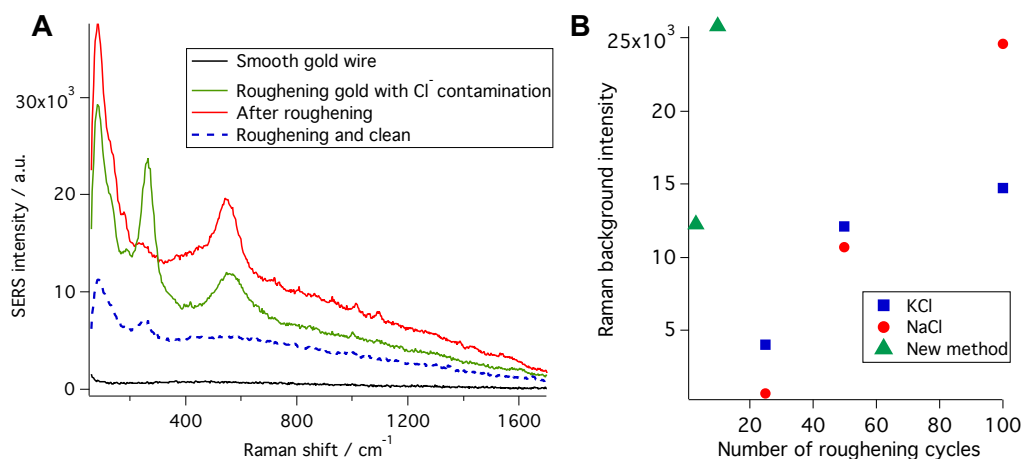


Figure 2.14: SERS background intensity change during electrochemical roughening process of gold polycrystalline foil (A) and a comparison of SERS background changes in various solutions (data intensity at 400 cm^{-1}) (B)

applied [71, 72]. The gold wire electrode was roughened electrochemically in 0.1 M KCl, by holding the potential at first at -1.16 V vs SCE for 10 min and stepping to -0.06 V vs SCE for 2 min. The potential was then swept from -0.06 to 1.44 V and back for 20 oxidation-reduction cycles at 750 mV/s. During each cycle, the potential was held at -0.06 V vs SCE for 30 s and then at 1.44 V vs SCE for 2 s. Finally, the potential was held at -0.36 V vs SCE for 2 min to desorb any adsorbed Cl^- ions and the gold electrode was rinsed thoroughly with milliQ water. Figure 2.14 A shows typical SERS background intensity changes during roughening. The efficiency of roughening methods as a function of the number of cycles is shown by the SERS background intensity at 400 cm^{-1} in Figure 2.14 B. The improved roughening procedure can be seen to give a very high intensity without requiring many roughening cycles.

To clean the gold sample after pyS adsorption, the sample was run as a working electrode with a gold counter electrode and Ag/AgCl reference electrode in 0.1 M NaOH. 20 cycles were run over a potential range between -1.2 to +1.4 V vs SCE at a scan rate of 10 mV/s [73]. Figure 2.15 shows the decrease of pyS characteristic peaks during the cleaning scans. For electrochemical

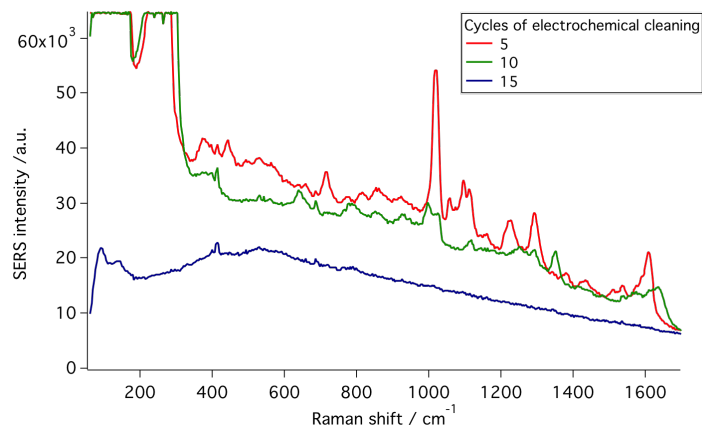


Figure 2.15: Electrochemical cleaning of Au-pyS surface by cyclic voltammetry in 0.1 M NaOH solution

characterization of adsorbed pyS, a standard three-electrode cell was used under nitrogen gas. A gold wire was used as working electrode. The counter electrode was a platinum wire, and the reference electrode was Hg/HgSO₄ (ALS Co. Ltd., Japan) to avoid any potential chloride contamination. The applied potential and electrolytes varied depending on experimental purposes. The cell used in our experiment is shown in Figure 2.16.

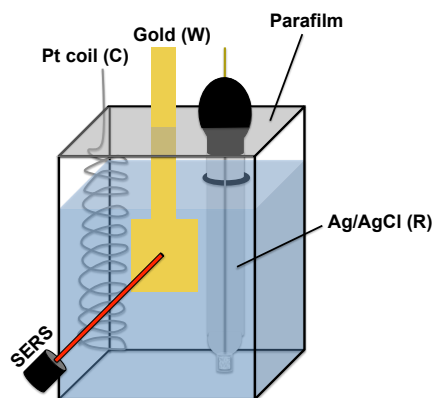


Figure 2.16: Setup of three-electrodes electrochemical cell used in experiment

2.3.4 Gold nanoparticles and SHINs synthesis

Shell-isolated gold nanoparticles (SHINs) to enhance the SERS signal were synthesised according to prior literature [74,75]. All chemicals were from Sigma-Aldrich as a 99.00 % purity substance. HAuCl_4 was obtained as a solid powder, and dissolved in Milli-Q water to 0.01 wt%. This gold solution was left at room temperature for more than 2 days before used. On the day of SHIN synthesis, 100 ml of the prepared HAuCl_4 solution was heated in a 250 ml round-bottom flask equipped with condenser and stirred for about half an hour until the solution reached boiling point. After that, 0.7 mL of 1 wt% sodium citrate solution in Milli-Q water was added to the HAuCl_4 solution quickly. This step is critical in this experiment, as the speed of the stirrer as well as concentration of sodium citrate and the speed of the addition affect the size and quality of gold nanoparticles. This mixture was left at this condition for half an hour, then removed from the hot plate and left to cool to room temperature. Then 30 mL of this gold nanoparticle solution was mixed with 0.4 mL of 1 mM 3-(aminopropyl) trimethoxysilane (APTMs) by stirring at room temperature for 15 min, before adding 3.2 mL of 0.54 wt% sodium silicate solution (NaSiO_2) with pH adjusted to 9-10. The stirred mixture was heated to 90° for an hour. The pH, temperature, and duration of reaction are very critical for SHINs synthesis. They determine the thickness of the silica shell around gold nanoparticles and the occurrence of pinholes. After finishing SHINs synthesis, the reaction was stopped suddenly by immersion in an ice bath for a few minutes [76]. SHINs were characterized via UV-vis spectroscopy to evaluate their size compared to bare gold nanoparticles. Moreover, eventual pinholes of SHINs were tested by Raman spectroscopy and cyclic voltammetry techniques. Then pyS was adsorbed on this dried SHINs layer, and observed with Raman spectroscopy.

2.3.5 Mercaptopyridine adsorption

In order to create a SAM of pyS molecules on the gold surface, either 4-mercaptopyridine (95 %) or 4,4'-dipyridyl disulfide (Aldrithiol-4 (98 % purity)) were used as supplied by Sigma-Aldrich (Poole, UK). A typical 40 μM 4-mercaptopyridine solution was first prepared in Milli-Q water

in a small glass vial, minimising headspace in order to avoid gradual oxidation from the air. Several publications report recrystallisation of 4-mercaptopyridine prior to use to reduce sulfur contamination. An easier choice is the use of an aqueous solution of aldrithiol, even though this only dissolves in water upon heating. Ethanol should not be used as a solvent, as it leads to pitting of the gold surface [77]. The roughened and cleaned polycrystalline gold foil (99.95 % purity) (Advent Research Materials) was then immersed in the solution and left for 5-15 minutes at room temperature to complete the adsorption. The sample was removed from solution with tweezers, rinsed with Milli-Q water, and finally dried with argon. The SERS spectrum of the sample was measured immediately after drying or the sample was kept in Milli-Q water during measurement. However, the pyS-Au surface was found to show a stable SERS spectrum for 3 months after adsorption. Note that for all adsorption experiments, all glassware used was cleaned with piranha solution to remove any contamination by organic molecules.

2.3.6 Metallisation

For further adsorption of metals on a pyS-Au surface, various metal salt solutions were prepared. For example, 0.1 mM PdSO₄ and 0.1 mM of K₂PtCl₄ were prepared in 0.1 M H₂SO₄, while 1 mM of RhCl₃ was prepared in 0.1 M HCl [43, 47, 78]. During the metal complexation process, the pyS-Au wire was immersed in metal solution for various periods ranging from 5 min to 3 days according to the purpose of each experiment. After complexation, the sample was removed from the solution carefully with tweezers and rinsed thoroughly with Milli-Q water, then dipped in the electrochemical cell to reduce the metal ion complex to solid metal. Finally, all samples were dried with nitrogen and were characterized by Raman spectroscopy and cyclic voltammetry immediately.

Chapter 3

Mercaptopyridine adsorption

3.1 Overview

The interest in 4-mercaptopyridine (pyS) as an adsorbate arises from a number of scientific areas, especially for the construction of metal-molecule junctions in molecular electronics. Self-assembly on noble metals generally occurs via the thiol group, which exposes the nitrogen lone pair to the solution and makes it available for coordination to metals or protons, as sketched in Figure 3.1.

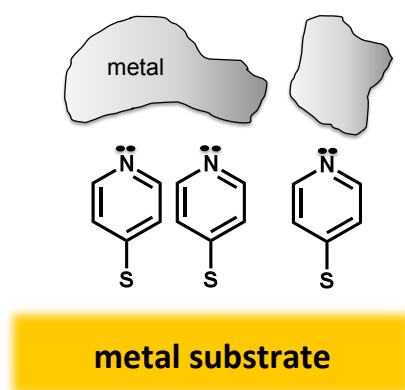


Figure 3.1: A typical metal-pyS-metal junction.

PyS has been used as a sensor for metal ions as it preferentially binds heavy metal ions such as mercury [79] or uranium [31]. Moreover, pyS also acts as an electron transfer promoter to macrocyclic compounds containing metal centres, such as porphyrins and phthalocyanines, for example the heme group in cytochrome c [80]. This also makes it useful as an electrochemical sensor, when surface-adsorbed pyS axially ligates to metallophthalocyanines or other metal complexes [81, 82]. Its use in the formation of metal-molecule-metal sandwich layers was pioneered by the Kolb group [47], who even created double-decker-type structures with pyS [83]. The concept was extended to other systems such as thiazole [33], pyridine-terminated araliphatic thiols [84], dimercaptoazobenzene [25], aminothiophenol [44], and dodecanethiol [85]. PyS is a popular molecule for Raman spectroscopy, as the aromatic ring structure makes it very polarizable. In acidic media, protonation leads to very clear spectral changes. Thus, many SERS studies have used pyS as a pH sensor, adsorbed on Ag and Au nanostructures and nanoparticles [86]. While pyS does not result in the most stable or most densely packed adlayers (the latter is particularly important for growing sandwich layers), its easy commercial availability in the form of 4-mercaptopyridine (pyS) or (4,4')-dipyridyldisulfide (pySSpy) have made it a much studied surface modifier. Despite numerous electrochemical and spectroscopic studies, and the frequent use of Raman spectra to diagnose coordination of the N lone pair to a metal ion or proton, there are still features of the spectra which are not understood well.

This chapter initially summarises what is known about adsorption of pyS on gold from techniques other than vibrational spectroscopy, in particular scanning tunneling microscopy and electrochemical studies. Then the surface-enhanced Raman spectrum of pyS is analysed in detail, with the help of recent theoretical work by Birke and Lombardi [87]. Of particular interest is whether the SER spectrum can be used to deduce the orientation or packing density of pyS on the surface. While typical contaminations can be discerned from the spectra, it will turn out that the pyS spectrum is largely independent of key parameters such as coverage, and cannot be used to predict whether metal sandwich formation will be successful (to be discussed in more detail in the next chapter). However, we find that hydrogen bonding to the N lone pair has a profound influence on the spectral appearance of the ring breathing vibration, although this has been surprisingly ignored in studies using pyS as a pH sensor.

3.2 Experimental

Gold foil was polished and electrochemically roughened in 0.1 M KCl solution prior to use. The gold foil was immersed in 40 μM of degassed PySSPy in milli-Q water to avoid sulfur contamination and left for 15 minutes. Gold disc electrode was used for electrochemical characterisation with Pt coil as a counter electrode and MSE as a reference electrode. The electrochemical setup is described in the experimental chapter. PyS was used as starting material in some data shown in Figure 3.4 and Figure 3.6. SERS spectra were taken in either air or in solution using 785 nm Mini Ram II (B&W Tek).

3.3 Adsorption of mercaptopyrindine on gold surfaces

The adsorption of pyS has been studied frequently on Au(111) by STM under various electrolytes and in UHV [90, 91]. A variety of ordered structures are observed, which depend on both the electrolyte and the applied potential. One of the most common structures, shown in Figure 3.2, is a rectangular ($5 \times \sqrt{3} - R30^\circ$) unit cell, which contains two pyS molecules. This structure has a coverage of 0.2 ML (with respect to the Au unit cell), corresponding to 0.46 nmol/cm² or 2.774×10^{14} molecules/cm² [82, 88, 92]. A slightly higher coverage of 0.58 nm/cm² is found on Au(100) [93]. The arrangement of molecules inside the unit cell has been simulated with DFT [89] and the theoretically most stable structure was found to be ($7 \times \sqrt{3} - R30^\circ$). In this structure, pyS is adsorbed on both three-fold hollow and bridge sites, being nearly upright on the former and with the ring plane tilted by about 50° towards the surface on the latter. In this configuration, the Au-S-C plane is perpendicular to the pyridine ring plane and to the surface plane (see Figure 3.2E). In the calculated ($5 \times \sqrt{3} - R30^\circ$) structure, some of the molecules are in a bridging position and the Au-S-C plane is now parallel to the ring plane with the two-fold axis of pyS rotated towards the surface (see Figure 3.2F). The rectangular unit cell can have three equivalent orientations with respect to the underlying lattice, therefore different domains are formed on the surface with a typical size of 20-30 nm [88]. The adsorption of pyS can cause

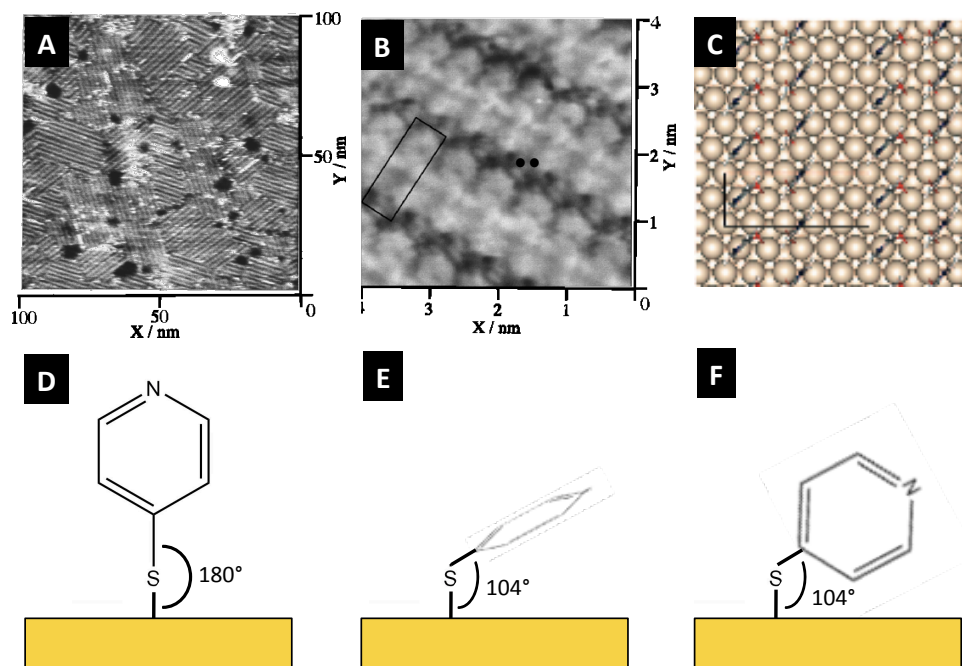


Figure 3.2: (A)(B) STM image of pyS on Au(111) showing domains and details of the $(5 \times \sqrt{3} - R30^\circ)$ structure (Adapted with permission from [88]. Copyright 1998 American Chemical Society.) (C) Calculated $(5 \times \sqrt{3} - R30^\circ)$ arrangement of pyS on Au(111) (Adapted with permission from [89]. Copyright 2008 American Chemical Society.) (D)(E) different orientations of adsorbed pyS: upright (C_{2v} symmetry; Au-S-C plane perpendicular to ring plane and surface plane; Au-S-C plane parallel to ring plane and perpendicular to surface plane (both C_s symmetry)).

the formation of small Au islands on both Au(111) [94] and Au(100) [93]. Thiols are known to interact so strongly with gold that they can lift a surface reconstruction and release gold atoms, although alkanethiols normally form depressions rather than islands on the gold surface.

Some of the earlier STM literature discussion centred around whether pyS adsorbed as thiolate or as disulfide, in particular when pySSpy was used as a starting material. The assignment of disulfide species was mainly based on observing bright protrusions at the typical S-S distance of 0.2 nm under electrolyte [88, 93] or in UHV [90]. While adsorption of pySSpy in UHV by sublimation could keep the S-S bond intact, more recent works casts doubt on the earlier interpretation in electrolyte. Zhou *et al.* carried out both STM and XPS [91], and observed the same sulfur binding energies for adsorption of pySSpy as for other thiolates, which indicates that the S-S bond is broken. The precise structure formed however does depend on the starting material. In H_2SO_4 , pyS forms a $(1 \times \sqrt{3})$ structure while pySSpy forms a $(7 \times \sqrt{3})$ structure. This could be caused by different adsorption sites for the molecules which are determined by the presence of sulfate and hydronium ions in solution. Sulfuric acid seems to play a special role as

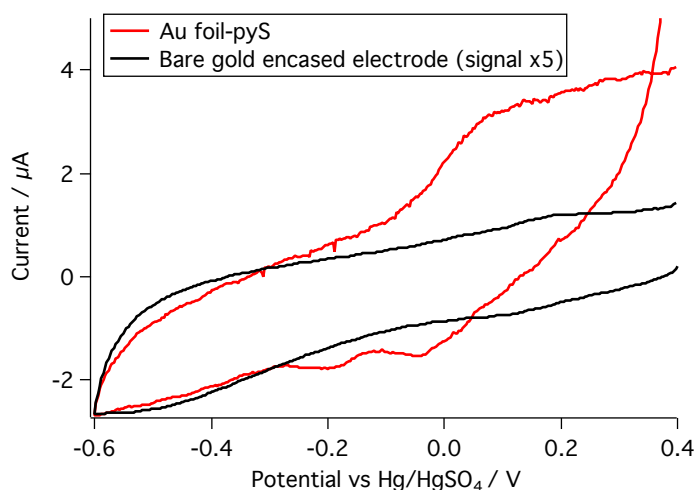


Figure 3.3: CV of the double layer region of a polycrystalline gold disc (encased) electrode without (black) and with adsorbed pyS (red) in 0.1 M H_2SO_4 , scan rate 50 mV/s.

an electrolyte as it is thought to be able to hydrogen bond to two pyS molecules simultaneously and encourage π - π interactions. As the potential is varied, a phase transition is seen in the cyclic

voltammogram in the form of a pair of quasi-reversible peaks around 0.4 V vs SCE specifically for H₂SO₄ as an electrolyte [91,95]. At the potential of +0.4 V vs SCE, the pyS layer forms a striped structure, where the distance between pyS molecules along the stripes was found to be 0.48 ± 0.05 nm, while the distance between stripes was 1.3 ± 0.13 nm or 2.9 ± 0.3 nm, corresponding to domains with $(5 \times \sqrt{3})$ and $(10 \times \sqrt{3})$ periodicity, respectively. The local coverage at this potential is around 0.2 ML. When the pyS layer was adsorbed at +0.15 V vs SCE, a more densely packed superstructure formed with a large number of defects. The distance between molecules was estimated to be 0.32 ± 0.05 nm and the distance between stripes was 0.55 ± 0.05 nm, which results in a local coverage of 0.5 ML. This phase transition only occurred in H₂SO₄ not in HClO₄ or a Na₂SO₄ solution at higher pH. In acidic solution, hydrogen can coordinate to the nitrogen lone pair, forming pyridinium cations. The authors speculated that the closer packing is caused by a bisulfate anion HSO₄⁻ bridging two pyridinium ions via hydrogen bonding. This could overcome the electrostatic repulsion between neighbouring pyridinium ions, forming a large hydrogen bonded network of molecules with enhanced ring interactions [95].

This phase transition in a pyS layer can even be seen on a rough surface as shown in Figure 3.3. The CV of the double layer region of pyS-Au was recorded in 0.1 M H₂SO₄ after 15 min adsorption in milliQ water, with the CV of bare rough gold shown for comparison. While the phase transition is not very pronounced, clear changes can be seen around 0.4 V vs SCE. A rough surface will not possess large-scale ordered pyS islands, so the effect should be reduced compared to Au(111).

Due to the gradient in the CV (possibly caused by a large contact resistance), it is difficult to estimate the double layer capacitance of the pyS layer. Bare gold has a capacitance of 24 μF/cm² and below the phase transition the pyS capacitance can be seen to be very similar to bare gold. This is also the case on Au(111). Normally, a densely packed SAM should block access of ions to the surface and reduce the capacitance, but perhaps the coordination of sulfate ions to pyS negates the blocking effect.

In order to obtain the coverage of adsorbed pyS, reductive desorption in alkaline solution

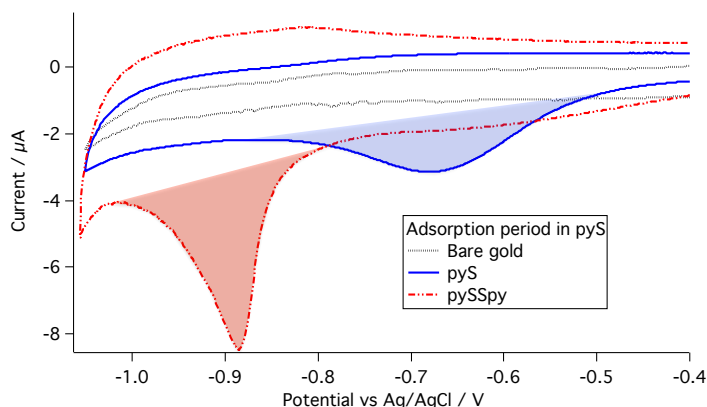


Figure 3.4: Reductive desorption of pyS from an encased polycrystalline gold electrode in 0.1 M NaOH from pyS and pySSpy adsorption, scan rate 50 mV/s.

can be used:



This is a one electron process [96], and the charge under the reduction peak can be used to determine the pyS coverage. Once the effective area of the gold electrode is known from the charge under the gold reduction peak, integration of the peak at -0.7 V vs SCE in Figure 3.4 yields a charge of around $17 \mu\text{C}/\text{cm}^2$ after 20 min adsorption in a $40 \mu\text{M}$ solution. A full monolayer on polycrystalline gold would correspond to a charge of $193 \mu\text{C}/\text{cm}^2$, therefore the coverage in Figure 3.4 is ≈ 0.1 ML. This is only half of the published values [88, 95, 97]. The low coverage from 4-mercaptopyridine adsorption is caused by sulfur contamination (see appendix). Use of aldrithiol (pySSpy) increases the measured charge to $52.6 \mu\text{C}/\text{cm}^2$ and therefore the coverage to 0.27 ML, which is close to the literature values. The different desorption peak position is due to the different gold surface structure (see appendix).

3.4 Surface-enhanced Raman spectroscopy of mercaptopyr-ridine on gold

A typical surface-enhanced Raman spectrum of pyS adsorbed on a rough gold surface is shown in Figure 3.5. The Raman peaks of adsorbed pyS have been assigned several times, on both silver [87, 98–102] and gold substrates [103–109]. The most prominent SERS peaks are labelled in Figure 3.5. The lowest frequency mode in the spectrum is the Au-S stretch at 258 cm^{-1} . This

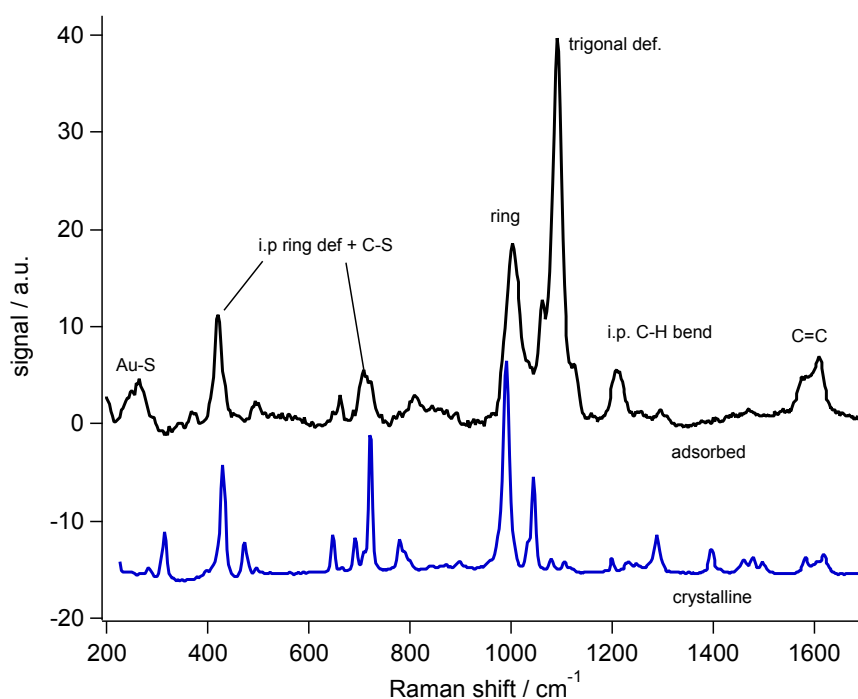


Figure 3.5: Raman spectra of crystalline and adsorbed pyS on Au with the main modes assigned.

indicates that adsorption has taken place, although the peak can be relatively weak and can partly overlap with the Au-Cl stretching peak at 265 cm^{-1} [70]. The clearest indication of adsorption is given by frequency and intensity changes in the so-called X-sensitive bands. These are vibrations of the aromatic ring which are altered strongly when one substituent is replaced by another. For mercaptopyridine, these are vibrations found at 431 cm^{-1} , 721 cm^{-1} and 1105 cm^{-1} in crystalline form. They are all in-plane deformations of the ring which couple to the C-S stretch. They shift

to 421 cm^{-1} , 710 cm^{-1} and 1094 cm^{-1} for pyS adsorbed on gold. Frequency downshifts of similar size have been found for several different metals [104,110] and are characteristic for PyS adsorbing via sulfur [111]. The highest frequency mode of these three modes, the so-called trigonal ring deformation, also gains considerable intensity in the process. Its intensity in the adsorbed state is a measure of the double-bond character of the C-S bond, which changes with pH [100,112]. Another important mode to indicate the change in local environment of the molecule is the ring breathing vibration at 1002 cm^{-1} . Its intensity and frequency are characteristic for the aromatic ring and change when the electron density on the ring is affected by coordination to the nitrogen lone pair. Such coordination also has a strong effect on the C=C ring stretching mode, which appears as a double peak at 1580 cm^{-1} and 1610 cm^{-1} . The higher frequency peak is the C=C stretch of protonated pyS, the lower frequency peak the C=C stretch of deprotonated pyS and their peak ratio has been used frequently to determine the local pH. The final peak, which is always clearly visible, is found at 1210 cm^{-1} and can be assigned to a symmetric in-plane CH bending mode. It also shifts slightly on protonation. In order to simplify the vibration mode discussion, the important vibrational modes for pyS are defined by their names and typical frequencies in table 3.1.

Table 3.1: The dominant vibrational modes of adsorbed mercaptopyridine and their typical frequencies

wavenumber / cm^{-1}	name
421	C-S with in-plane ring deformation
710	C-S with in-plane ring deformation
1002	ring breathing
1094	trigonal ring deformation
1210	in-plane C-H bend
1580	deprotonated C=C ring stretch
1600	protonated C=C ring stretch

All the spectral changes observed upon adsorption are a clear indication that mercap-

topyridine adsorbs as thiolate, rather than via the nitrogen lone pair or the aromatic π -electrons in the pyridine ring. However, small variations in the spectra could indicate differences in the orientation or packing and will be discussed later.

All the vibrational modes just assigned are totally symmetric modes of the pyS anion, which has C_{2v} symmetry. Several other, typically much smaller peaks can also be seen, which might not all be totally symmetric. Since the symmetry of the modes in a SER spectrum can give an indication of the orientation of the adsorbate [60] and since the orientation should determine the ease of coordination to the nitrogen lone pair, we decided to redo the assignment of the vibrational modes, based on our own DFT calculation. This task was considerably simplified by the recent paper by Birke and Lombardi [87] on pyS adsorbed on silver, which draws on a new classification of the vibrational modes of singly substituted benzene by Gardner and Wright [113]. Earlier publications have all used the Wilson notation for benzene vibrational modes. While this notation is well known, the reduced symmetry of pyS can make the assignment highly ambiguous and difficult to match the motion seen in the simulation with the patterns shown by Wilson [114]. The DFT calculation was carried out with Spartan 16 software, using density functional theory at B3LYP level with a 6-31G** basis set. This level of DFT reproduces the frequencies calculated by Birke and Lombardi for pyS on silver (see appendix), even though we only included a single gold atom in the simulation rather than a cluster. Raman intensities are generally more difficult to simulate and require a higher level of theory [87], but our simulation does correctly reproduce the strong intensity increase of the trigonal ring deformation.

Our calculated spectra for both deprotonated and protonated pyS bound to a single gold atom are shown in Figure 3.6. The simulation overall reproduces the peak positions well with a single scaling factor of 0.98 for all frequencies. The only mode frequency which is far off the experimental value is the Au-S stretch. The simulation places it at 337 cm^{-1} , whereas it is found at 258 cm^{-1} in the experimental spectrum. The discrepancy probably arises, because only a single gold atom is included rather than a cluster or a bulk surface. If we consider pyS-Au as a diatomic, then its reduced mass is 43 amu. The reduced mass of pyS-Au₁₃ (the cluster size used by Birke and Lombardi for silver) is 86 amu. Since the vibrational frequency of a diatomic is inversely proportional to the square root of the reduced mass, this increase in reduced mass should

shift the peak from 337 cm^{-1} down to 237 cm^{-1} , much closer to the measured value. In principle, Spartan 16 is able to calculate Raman spectra for larger gold clusters, but the calculation on a typical desktop computer would take several days for a gold cluster, while pyS-Au takes about half an hour to complete.

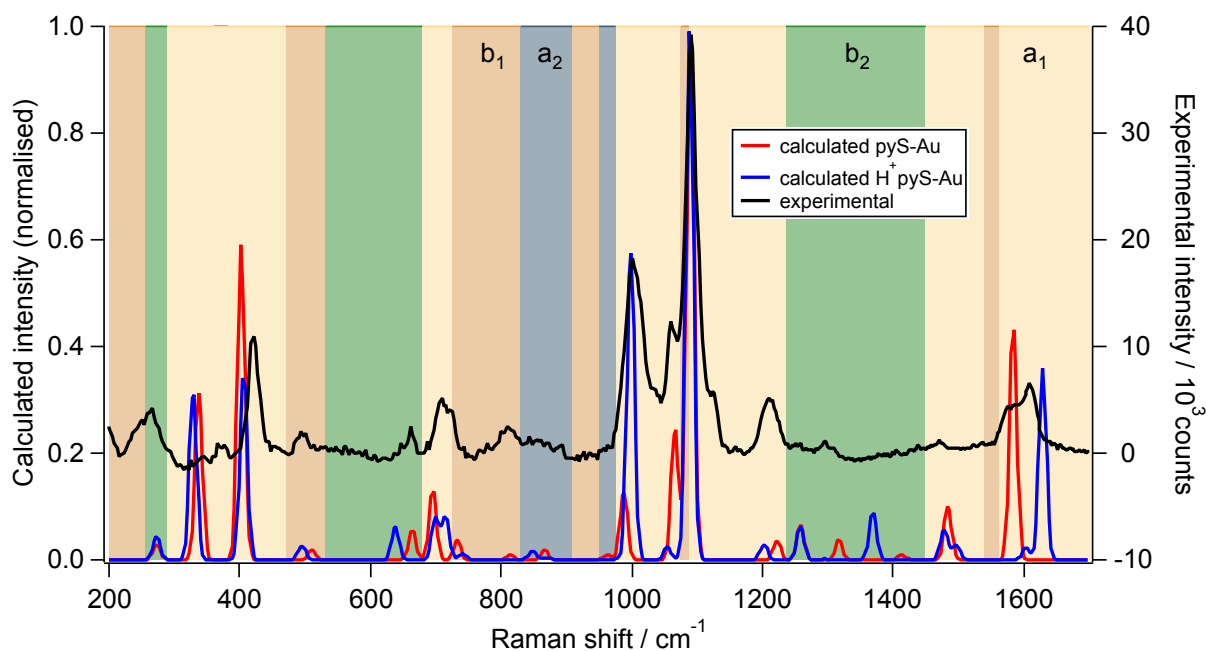


Figure 3.6: Comparison between a typical adsorbed spectrum and a DFT calculation of pyS (red) and pyS-H⁺ (blue) bound to a Au atom. The background is coloured according to the symmetry of the vibrational modes.

In order to simplify the assignment, the background of the graph is shaded in yellow, orange, green, and blue for a_1 , b_1 , b_2 , and a_2 vibration modes, respectively. In this comparison, all dominant vibrational modes can be seen to be a_1 modes, which are the strongest modes in SERS as discussed earlier. The smaller peaks and their symmetries are as follows:

- 494 cm^{-1} (b_1 symmetry): out-of-plane deformation of the ring
- 662 cm^{-1} (b_2 symmetry): in-plane asymmetric ring deformation of the ring
- 810 cm^{-1} (b_1 symmetry): out-of-plane CH + ring deformation

- 1471 cm⁻¹ (a₁ symmetry): symmetric in-plane CH bend

In the literature, the mode at 1580 cm⁻¹ has sometimes been assigned as an asymmetric b₂-type mode (\mathcal{M}_{23} or 8b₂, eg [100,107]), but the mode in question is so weak in the simulation that it cannot be noticed in the calculated spectra shown. The simulation clearly shows that protonation explains the double peak around 1600 cm⁻¹.

What does the pyS-Au spectrum tell us about the orientation of the molecule? In electromagnetic field-enhanced Raman scattering, the selection rule states that totally symmetric vibrational modes are most strongly enhanced, since their intensity is related to the α_{zz} polarisability tensor element [60]. However, which vibrational modes are totally symmetric depends on the orientation of the molecule on the surface. In the literature, the symmetry of mercaptopyridine is generally discussed as if it belonged to the C_{2v} symmetry group, even though only the pyS anion has this symmetry. On the surface, C_{2v} symmetry is only given if the 2-fold rotation axis of the pyridine ring points along the surface normal, as sketched in Figure 3.2D. This implies a surface-S-C angle of 180°, which can be achieved if the sulfur orbitals are sp hybridised. However, sp³ hybridisation is about 2 kJ/mol more stable for thiolates on gold [115] and yields a lower surface-S-C angle of around 104°. Recent calculations on Au(111) indicate that the most stable configuration for an isolated pyS adsorbate is with the ring plane tilted by 50° towards the surface [89], such that the Au-S-C plane is perpendicular to the ring plane (Figure 3.2E), which preserves the mirror plane perpendicular to the ring plane. This reduces the symmetry to C_s, which possesses only two types of vibrational modes, namely totally symmetric a' and asymmetric a'' modes. The correlation between C_{2v} and C_s modes for this case is shown in Table 3.2.

Therefore, any mode which was a₁ or b₂ for an upright pyS, would become totally symmetric for a tilted pyS. This would explain the presence of the modes at 494 cm⁻¹ and 810 cm⁻¹ in Figure 3.6.

In the simulation of other ordered structures on Au(111), pyS also appeared with the ring plane mostly perpendicular to the surface, but the C₂ axis rotated, see Figure 3.2F [89]. If the ring plane is perpendicular to the surface, then this mode would also possess C_s symmetry, but the correlation between upright and rotated pyS vibrational modes is different, as shown in

Table 3.2: Symmetry changes of vibrational modes between C_{2v} and C_s molecular symmetry

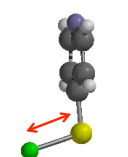
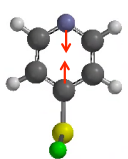
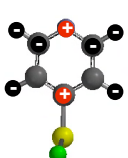
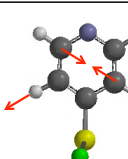
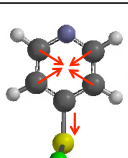
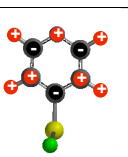
C_{2v}	C_s (mirror C-N)	C_s (mirror ring plane))
a_1	a'	a'
a_2	a''	a''
b_1	a'	a''
b_2	a''	a'

Table 3.2 (mirror ring plane). In this case, former b_2 modes would become totally symmetric, which could explain the appearance of the b_2 mode at 662 cm^{-1} . It seems unlikely however that many of these rotated pyS molecules exist on the surface, as there are several b_2 modes in the region from 1250 cm^{-1} to 1450 cm^{-1} which are not seen in the experimental spectra. A similar argument can be made for the existence of pyS molecules with a twisted ring plane such that all symmetry elements disappear.

Almost all of the features seen can therefore be justified by a tilted orientation of pyS on the gold surface and there is no need to include chemical enhancement in the discussion to explain the appearance of C_{2v} asymmetric modes [87, 104].

The results of the full calculation are summarised in Table 3.3 below. They include our experimental and calculated frequencies, a typical frequency range to cover literature values and both Gardner and Wilson notation systems. In addition, small cartoons of the vibrational modes are included.

Table 3.3: Summary of all experimental and calculated pyS-Au Raman peaks, their Gardner and Wilson mode numbers [103–106] and vibration pattern

$\nu_{Cal}/$ cm^{-1}	$\nu_{Exp}/$ cm^{-1}	Notation (symmetry)	ν_{Exp} range/ cm^{-1}	Mode description	Vibrational illustration
337	280	a_1	230-250	Au-S stretch	
402	417	$7a_1, 6a_1,$ (\mathcal{M}_{11})	428-430	$\delta(C-S)/\gamma(CCC)$	
510	497	$11b_1,$ (\mathcal{M}_{19})	608	op CH def	
664	665	$6b_2 (\mathcal{M}_{29})$	643-682	$\beta(CCC)$	
696	709	$6a_1 (\mathcal{M}_{10})$	700	op C-H def	
733	724	$4, 11b_1$ (\mathcal{M}_{18})	711-721	$\beta(CC)/\nu(C=S)$ ip ring def with C=S	

$\nu_{Cal}/$ cm^{-1}	$\nu_{Exp}/$ cm^{-1}	Notation (symmetry)	ν_{Exp} range/ cm^{-1}	Mode description	Vibrational illustration
813	809	$10b_1$ (\mathcal{M}_{17})	815	$\gamma(CH)$ op CH def	
866	851	$10a_2$ (\mathcal{M}_{13})	850	op CH def	
962	N.D.	$5b_1$ (\mathcal{M}_{15})	990	op CH def	
988	1002	$1a_1$ (\mathcal{M}_9)	988-1013	ring breathing	
1066	1064	$18a_1$ (\mathcal{M}_8)	1030-1058	$\beta(CH)/\nu(C=S)$ ip CH def with C=S	
1084	N.D.	$18b_2$ (\mathcal{M}_{28})	1085	$\beta(CH)$ ip CH def	
1090	1093	$7a_1$ (\mathcal{M}_6)	1095-1099	trigonal ring def with C=S, X-sensitive	

$\nu_{Cal}/$ cm^{-1}	$\nu_{Exp}/$ cm^{-1}	Notation (symmetry)	ν_{Exp} range/ cm^{-1}	Mode description	Vibrational illustration
1222	1214	$9a_1 (\mathcal{M}_7)$	1210-1220	$\beta(CH)$ ip CH def	
1258	1271	$3b_2 (\mathcal{M}_{25})$	1277	$\beta(CH)$ CCC distortion with CH def, ip N-H	
1317	1309	(\mathcal{M}_{26})	N.D.	$\beta(CH)$ ip CH def	
1414	1404	$10b_2 (\mathcal{M}_{24})$	1391-1440	$\nu(C=C)$ ring stretch	
1484	1476	$19a_1 (\mathcal{M}_5)$	1470-1484	$\nu(CC/C=N)$ ring stretch	
1562	1574	$8b_2 (\mathcal{M}_{23})$	1551-1581	$\nu(C=C/C=N)$ ring stretch	
1584	1608	$8a_1 (\mathcal{M}_4)$	1580-1620	$\nu(CC)$ ring stretch	

I will now illustrate other factors which influence pyS spectra.

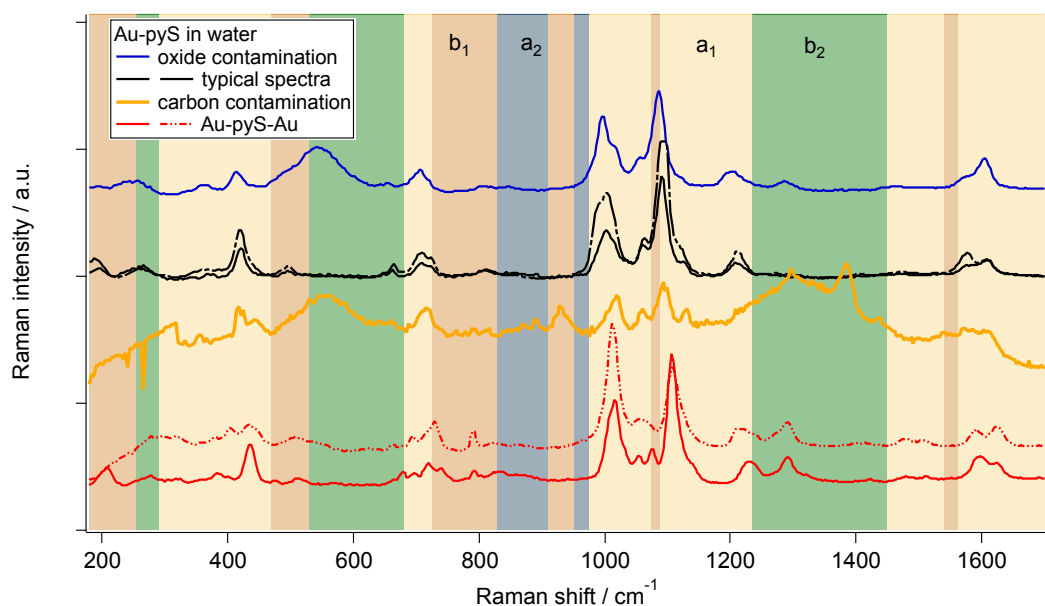


Figure 3.7: Raman spectra of typical Au-pyS and exceptional conditions, (eg. double-ended link and surface contamination).

Figure 3.7 shows a typical pyS spectrum and two other types of spectra which are encountered regularly. The blue spectrum shows a broad peak around 550 cm^{-1} , which can be identified as a Au-O stretch indicating oxide formation on the surface [116,117]. It can be generated from surfaces represented by the typical pyS spectrum in black, by keeping the potential at values of 1 V or above for several minutes. Even in purged milliQ water, sufficient oxygen is found in the solvent to gradually oxidise the gold surface. Equally, the intensity of the peak can be reduced by reduction of the gold surface. Sulfur contamination is expected, particularly for commercial pyS, which has not been recrystallised [80], or for pySSpy dissolved in ethanol [77]. These studies show that this can normally be counteracted by keeping the adsorption time to less than 20 min.

The two red spectra shown in Figure 3.7 contain a few unusual peaks at 800 cm^{-1} , 1040 cm^{-1} and 1280 cm^{-1} . The additional peak in the ring breathing region is typically seen when a metal ion successfully coordinates to the nitrogen lone pair (see chapter 4). Such double bonding could arise when pyS is found in a very rough environment as illustrated in Figure 3.8.

Alternatively, since thiol adsorption is often accompanied by a reconstruction of the gold surface, some of the gold atoms released could potentially bind to the nitrogen lone pair. Alternatively, on CuO, a chelate structure, where pyS binds via both sulfur and nitrogen, has been suggested [104]. The additional peaks all have b_2 symmetry, indicating a different average orientation to typical adsorbed pyS. The peak at 1280 cm^{-1} can be assigned to an asymmetric stretching motion of the ring, which involves a relatively large amplitude on the nitrogen. In addition, extra weak peaks appear in the regions between 800 cm^{-1} and 900 cm^{-1} and between 1400 cm^{-1} and 1500 cm^{-1} . Alternatively, the strong peak at 1280 cm^{-1} could arise from a pypyS species, created through a reaction between adsorbed pyS and pyS in solution, where the py-sulfur bond breaks in solution and the pyridine ring coordinates to the lone pair of adsorbed pyS [118]. A Spartan simulation of this species shows indeed a very strong peak at 1257 cm^{-1} and several peaks in the ring breathing region, as each of the pyridine rings can carry out individual or coupled oscillations. Whether the reason is a chelation, binding to another gold atom or a pypyS species can not be clearly decided from these data, as this type of spectrum was not seen very often. The next chapter contains a more in-depth discussion of the influence of metal coordination on the pyS SER spectra. The best indication that the microscopic arrangement of pyS molecules does not



Figure 3.8: A rough gold surface might lead to pyS binding to gold with both the thiol and the nitrogen lone pair.

strongly influence the SER spectrum is shown in Figure 3.9, which combines SER spectra of pyS on different gold surfaces - roughened foil, gold nanoparticles and inside pinholes on silica-shell encased gold nanoparticles (SHINs). The local coverage and microstructure can be expected to be different on all three surfaces, yet with the exception of differences in the ratios of some pH-sensitive peaks and the width and frequency of the ring breathing mode, there are no clearly discernible differences between spectra.

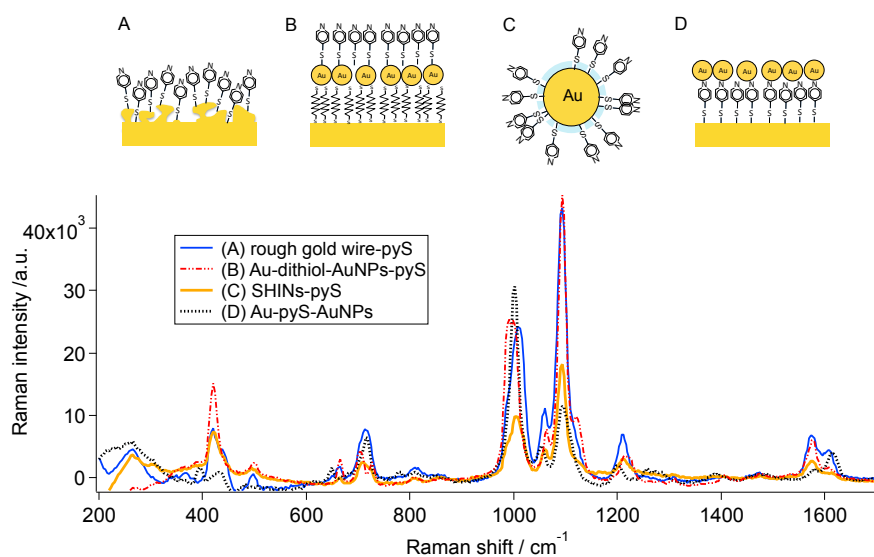


Figure 3.9: SERS spectra of pyS adsorbed at a variety of gold surfaces - (A) rough, (B) gold nanoparticles linked to flat gold with a dithiol, (C) in pinholes of SHIN particles or (D) adsorbed on flat gold with a layer of bare gold nanoparticles above.

3.5 The influence of hydrogen bonding

The metallisation of a pyS layer occurs by complexation of a metal ion to the nitrogen lone pair. A related process already happens on the SAM in pure water - protons can coordinate to the nitrogen and form pyridinium cations. The accompanying spectral changes make pyS a good pH sensor and a number of papers have looked into the pH dependence of pyS Raman spectra [32, 86, 104–107, 112, 119] and intensity changes in the pH-sensitive peaks have been used to deduce bonding to gold nanoparticles deposited on top of a pyS SAM [120, 121]. A typical set of pH-dependent data is shown in Figure 3.10. Protonation affects several Raman peaks. The largest frequency shift occurs for the C=C stretch, which, as discussed above, occurs at 1580 cm^{-1} for pyS and at 1610 cm^{-1} for pyS-H⁺ [86, 104–107, 119]. The intensity ratio of these two peaks is therefore often used to determine the local pH. Protonation also strongly affects the intensities of the ring breathing and ring stretching vibrations. The intensity of the ring breathing vibration is related to the stability of the aromatic ring system. Protonation stabilises

the aromatic ring and strengthens this peak. The trigonal ring deformation involves stretching of the C-S bond, which has more double-bond character in the deprotonated form, increasing its intensity. Therefore the intensity ratio of ring breathing to trigonal ring deformation is low at low pH and then increases with increasing pH. The peak around 720 cm^{-1} is also a combination of a ring deformation with C-S stretch. It does not change intensity, but the lower frequency shoulder at about 710 cm^{-1} belongs to the protonated species, whereas the deprotonated species has a peak at 720 cm^{-1} [112]. The in-plane C-H bending mode around 1200 cm^{-1} is also pH-dependent. Again, the lower frequency peak at 1206 cm^{-1} corresponds to the protonated form and the peak at 1214 cm^{-1} belongs to the deprotonated form. The protonated adsorbate layer also always shows a small peak at 1250 cm^{-1} .

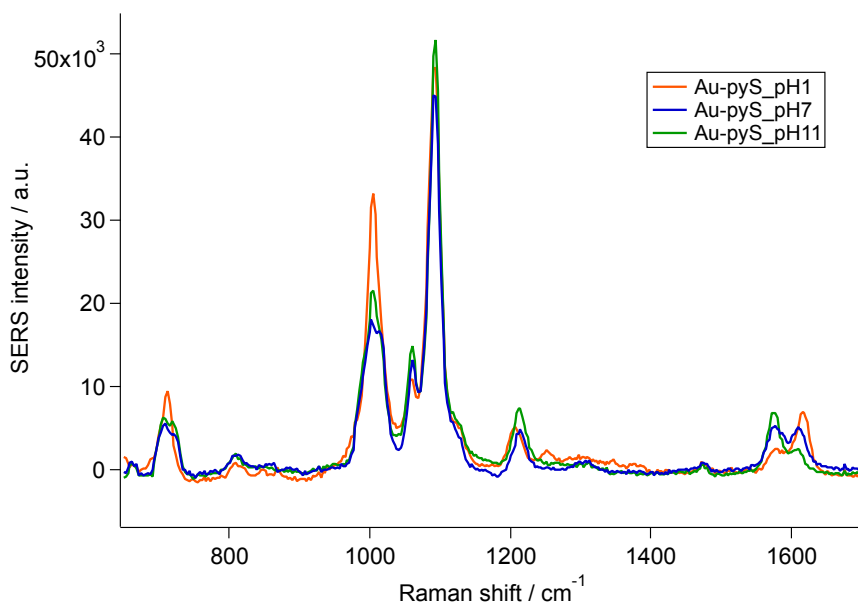


Figure 3.10: SERS spectra of Au-pyS in aqueous solution, pH adjusted with H_2SO_4 or NaOH.

In acidic solution, an available proton can bind to the nitrogen lone pair and form pyS-H^+ . In basic solution, the deprotonated form dominates. The pK_a of pyS adsorbed on gold has been determined as 4.6 ± 0.5 from electrochemical capacitance data [122] or as 5.3 ± 0.3 from a SERS titration curve [106]. This is very different from the bulk value of 1.43 ± 0.07 [123]. The low bulk value is due to solvent effects on the tautomeric equilibrium between thiol and thione, shown in Figure 3.11 [124]. In a polar solvent, the thione form is much more stable than

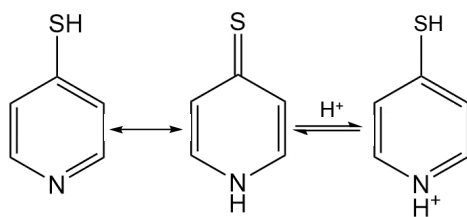


Figure 3.11: Thiol-thione tautomerism of pyS and protonation at low pH.

the thiol due to its higher polarity (dipole moment 8.2 D versus 2.1 D), which lowers the pK_a . The adsorption of mercaptopyridine removes the tautomerism, but it also makes protonation of neighbouring adsorbed pyS unfavourable due electrostatic repulsion. Both effects increase the pK_a .

There is one more remarkable change visible in Figure 3.10, which is not discussed in the SERS literature at all. The ring breathing mode does not just change in intensity, it also exhibits frequency and width changes. Generally, it looks narrower in highly acidic solution and appears to develop shoulders on its low and high frequency sides in neutral or basic solution. This mode also shows significant changes during adsorption in pure water, which will be discussed in the following. PySSpy dissolved in ultrapure water was chosen as the starting material to reduce the chance of sulfur contamination and a concentration of 1 mM was chosen as representative for other experiments. Adsorption was followed over the course of 30 min, with spectra integrated over 30 s acquired every 2 min. The raw data are shown in Figure 3.12. Two things should be noted. The 0 min trace (corresponding to 30 s of adsorption) has an unusually low SER background signal and the most likely explanation is a small motion of the sample at the start of the experiment caused by injection of pyS solution into the cuvette. SER peak heights scale with the height of the background (which will be shown in the next chapter, [69]), therefore we have scaled the 0 min spectrum by a factor 5 for later detailed analysis of peak shapes. The second noticeable feature is a gradual decrease in the background with adsorption time. This was also noticed in another in-situ adsorption experiment at lower concentration, which suffered from some carbon contamination. The decrease of the background as a function of time (including the 0 min spectrum) is also shown in the same figure. There is an initial slow decrease, followed by

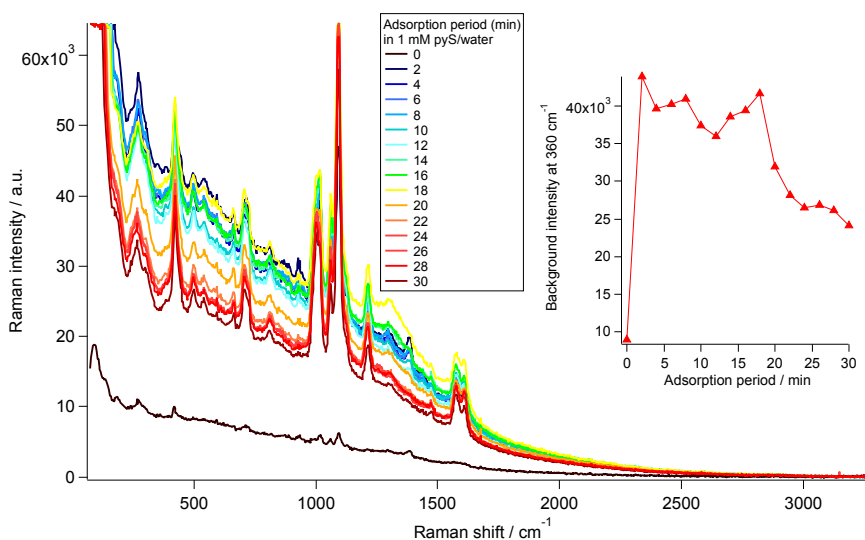


Figure 3.12: SERS spectra acquired in-situ during adsorption of 1mM pyS.

a sharper decrease around 20 min. A possible explanation is a microscopic rearrangement of the gold surface by the pyS adsorption, which could lower the electromagnetic field enhancement of the surface.

The background-subtracted spectra are shown in Figure 3.13. In general, all peaks increase over time, with the exception of the peak at 1380 cm⁻¹ which decreases. Since this is a b₂-type peak which is not normally seen, this could indicate that the orientation of pyS changes during the first few minutes of adsorption. There is also a relatively small broad peak around 1300 cm⁻¹, which is probably a carbon contamination.

The most striking feature of the spectra though is the changing appearance of the ring-breathing mode, which is shown in detail in an inset to the Figure 3.13. The peak consists of three narrower peaks in changing proportions over time. Initially, the largest peak is at about 1020 cm⁻¹ with a small shoulder at 985 cm⁻¹. With increasing time, a third peak at 1017 cm⁻¹ becomes stronger. We suggest that the three peaks correspond to three different species of adsorbed mercaptopyridine, namely pyS, pyS-H⁺ and pyS hydrogen-bonded to water. Hydrogen bonding is known to affect the frequency of the pyridine ring breathing mode [125]: free pyridine has a ring breathing mode at 990 cm⁻¹, hydrogen-bonded pyridine vibrates at 994 cm⁻¹ and

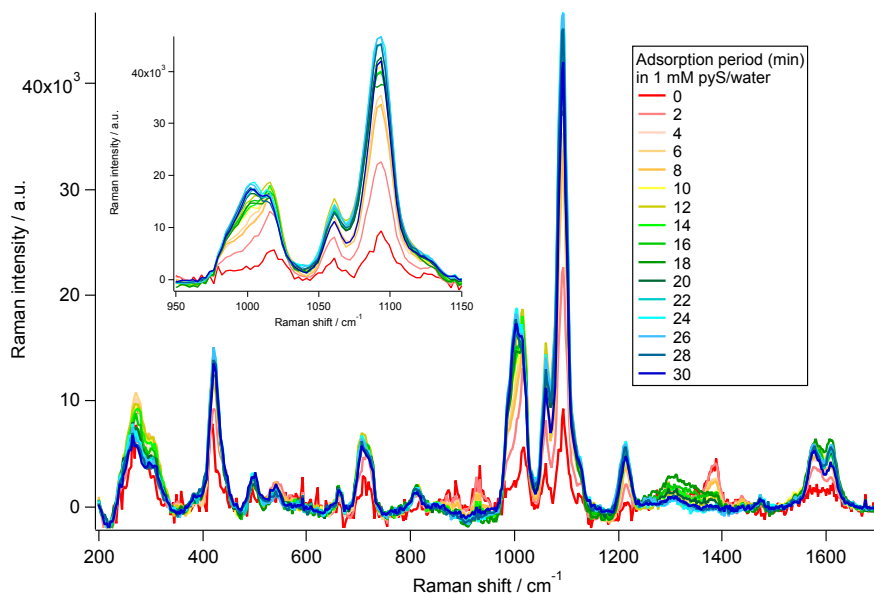


Figure 3.13: SERS spectral change with adsorption period.

pyridinium has a ring breathing frequency of 1003 cm^{-1} . The blue shift of the frequency indicates stronger bonds and thereby a more stable aromatic ring. This can be explained in an intuitive way: the stability increases because H-bonding pulls the electron density of the lone pair away from the aromatic ring system. Therefore, the delocalised π -electrons in the pyridine ring are less disturbed by the nitrogen lone pair electron. The shorter the hydrogen bond, the more stable the aromatic ring; a trend which is continued for pyridinium, which is still aromatic, since the proton binds to the lone pair and not the ring.

In order to understand the effect of hydrogen bonding on adsorbed pyS, we simulated hydrogen-bonding between a variety of species and pyS bound to a single gold atom. Formamide is known to form a comparatively weak H bond, a single or two water molecules form slightly stronger bonds, while acidic molecules such as hydrochloric acid, sulfuric acid, acetic acid form much stronger hydrogen bonds. The H-bond distances range from 1.016 \AA for protonated pyS up to 1.997 \AA for formamide. The shortest bonds are of course formed in the protonated pyS- H^+ , but the bond can be slightly lengthened by including a chloride counter ion or a water molecule. The results are summarised in Figure 3.14, which shows the frequencies of the ring breathing,

ring stretching and trigonal ring deformation modes as a function of the nitrogen-hydrogen bond length. Free pyS was placed at 3 Å in the graph in order to incorporate the relevant data points.

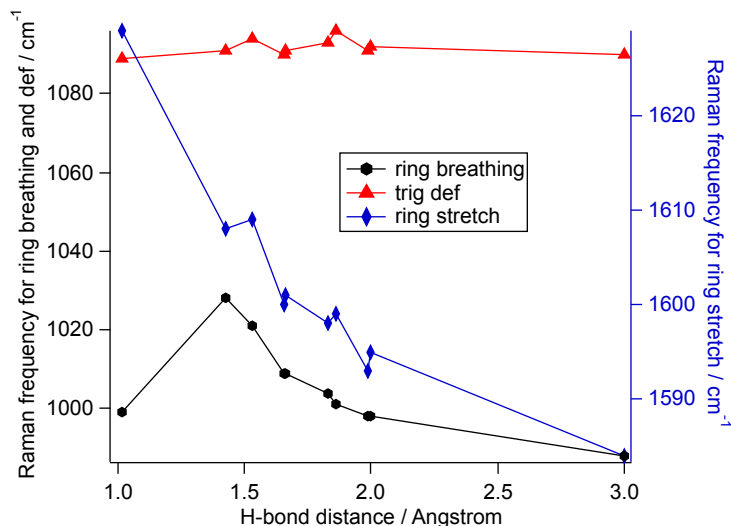


Figure 3.14: Dependence of ring breathing and stretching frequencies on H-bond distance from simulated species.

The calculation mostly confirms for pyS-Au what is known from pyridine: the trigonal ring deformation frequency is independent of any hydrogen bonding to the nitrogen lone pair, while both the ring breathing and ring stretching frequencies generally increase with decreasing N-H distance. The only exception is when the molecule becomes protonated. The intensity of the ring breathing mode increases, because the aromatic ring is more stable in the protonated than in the deprotonated state, which is also experimentally observed, but the frequency red shifts to a value that is close to pyS hydrogen bonded to water. This is not a feature of the calculation, which correctly reproduces the frequency blue shift from pyridine to pyridinium (experimental shift 13 cm⁻¹, calculated shift 11 cm⁻¹), but must be related to the substitution on the ring. We found that gas-phase mercaptopyridine with its electron-donating -SH group has calculated frequencies of $\nu(\text{pySH}) < \nu(\text{pySH-H}^+) < \nu(\text{pySH-water})$, while an electron-withdrawing group like -CN leads to $\nu(\text{pyCN}) < \nu(\text{pyCN-H}^+) < \nu(\text{pyCN-water})$. Both coordination to the nitrogen and substitution will affect the ring stability, but since we are not aiming for a detailed understanding of the exact balance of these effects here, we will instead use the relative calculated frequencies in

combination with experimental observation to assign contributions to the ring breathing mode. In

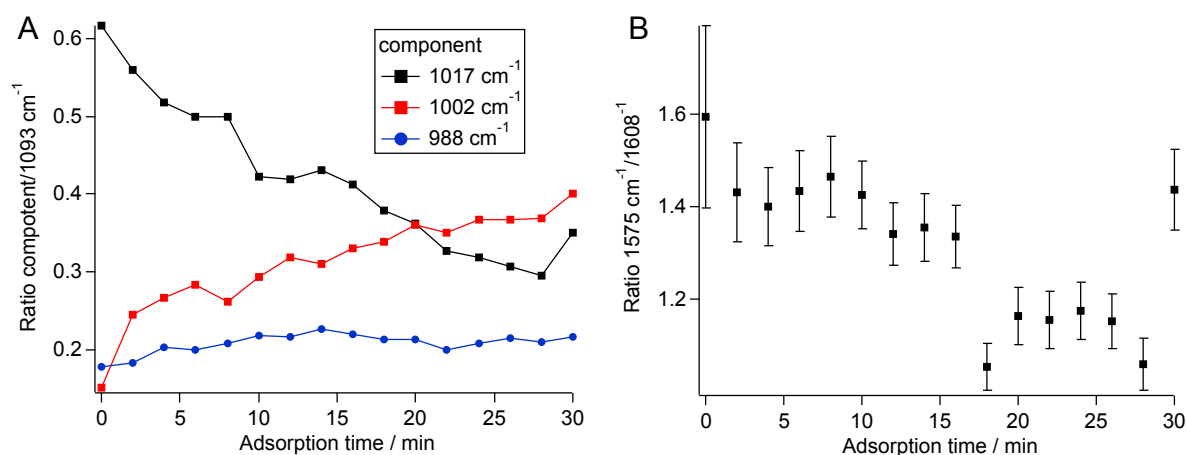


Figure 3.15: SERS intensity ratio of (A) 988 cm⁻¹, 1002 cm⁻¹, and 1017 cm⁻¹ to 1093 cm⁻¹ (trigonal ring deformation and (B) 1575 cm⁻¹ to 1609 cm⁻¹.

the experimental spectrum we fitted three components to the ring breathing peak with constant frequencies set at 988.4 cm⁻¹, 1002.5 cm⁻¹ and 1017.0 cm⁻¹. Figure 3.15 (A) shows the ratio of each component against the trigonal ring deformation mode. It can be seen that the lowest frequency peak contributes a relatively constant fraction, while the center peak increases and the high frequency shoulder decreases with adsorption time. We also fitted the ring stretching region with two modes at 1576.7 cm⁻¹ and 1609.9 cm⁻¹ and plot their ratio in Figure 3.15 (B). The ring stretching peaks reveal what can be discerned from the spectra by eye, namely that the intensity of the protonated peak increases with adsorption time. The relative increase as well as the relatively large contribution from the protonated species is unexpected. The solvent is milliQ water and adsorption occurs at neutral pH, so with a surface pK_a of 4.6 one would expect more than 99% of adsorbed pyS to be deprotonated. This is not the case and in fact samples prepared in essentially the same way (roughening procedure, starting material, concentration, adsorption time) show a wide range of ring stretching and ring breathing ratios. Paulo *et al.* recently determined a very different surface pK_a for pyS by determining the peak current of the ferri/ferrocyanide redox couple as a function of pH [126]. They obtain a value of 7.5 and attribute this to oxidative cleavage of the C-S bond aided by ferricyanide. Such a high value would explain why we frequently observe significant intensities of the protonated C=C stretching peak in pure water or air. Perhaps the

value of the pK_a depends quite sensitively on the adsorption site of pyS, which is very difficult to control when roughened surfaces are used and could perhaps explain the wide range of ratios observed by us. In this particular case, it is possible that the small carbon contamination seen around 1300 cm^{-1} causes a shift in the pK_a .

In either case, the spectra indicate that the fraction of protonated molecules slightly increases with adsorption time. Protonated pyS has a higher ring breathing intensity as the calculations and experiments have shown, eg Figure 3.10. This means that, of the three ring breathing components, the centre one has to correspond to protonated pyS, while the low frequency shoulder represents pyS without any hydrogen bonding and the high frequency shoulder corresponds to the gradually decreasing fraction of hydrogen-bonded pyridine. This assignment can be confirmed by several other data sets, where each set was recorded on the same pyS layer but with changing solvent. The data in Figure 3.16 were acquired in milliQ water, 0.1 and 0.5 M H_2SO_4 and so-called superacid, a mixture of trifluoromethane sulfonic acid, carbon tetrachloride and acetonitrile, which should protonate a larger fraction of adsorbed molecules [127]. If we first consider just the changes occurring in switching from water to H_2SO_4 , it can be seen that with increasing concentration of the acid the high frequency shoulder disappears. This agrees with our assignment of this shoulder as pyS hydrogen-bound to water. The switch from sulfuric to superacid leads to a frequency blue shift. The calculated H-bond distance is reduced from 1.530 \AA to 1.424 \AA , while the calculated frequency of the ring breathing vibration increases by 7 cm^{-1} compared to a measured increase of 5 cm^{-1} . The stronger acid clearly leads to a more stable aromatic ring.

Wang *et al.* found for a pyridine-terminated araliphatic layer on gold (4-(pyridin-4-yl)biphenyl-4-yl)-methanethiol) that the C=C stretching frequency of the pyridine and benzene rings shifted with adsorption time, which was attributed to $\pi-\pi$ interactions between adsorbates, which change with coverage and structure of the layer. We have found a similar frequency shift while changing solvent. Figure 3.17 shows the frequencies of both ring stretching and all ring breathing modes as the solvent is switched from water (blue symbols) to sulfuric acid (red symbols) to sodium hydroxide (green symbols). It can be seen that during the switch to sulfuric acid, the frequencies of both ring stretching modes increase (3.17 B), while the ring

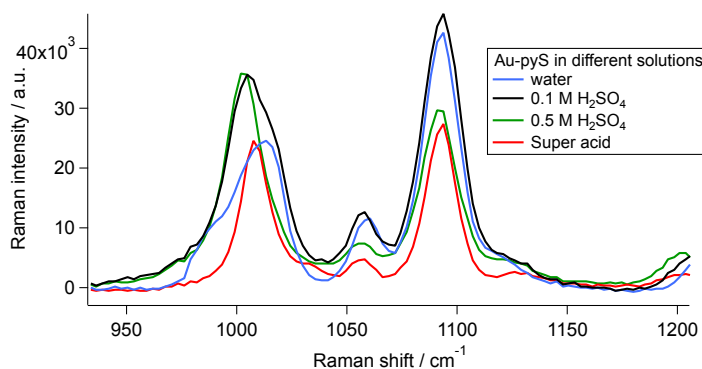


Figure 3.16: SERS spectra of Au-pyS in superacid solution at ring breathing region.

breathing frequencies are virtually constant (3.17 A). This is perhaps related to the special role of sulfuric acid observed in electrochemistry discussed earlier. If a bisulfate ion can bridge two pyS and encourage interaction between rings, this could explain the observed frequency shift. The microscopic rearrangement is probably aided by the weaker Au-pyS bond for protonated adsorbates, which removes the clear preference for a bridging adsorption site and could indicate that pyS can rearrange in the acidic state more easily [89]. Hydrogen bonding to water itself however changes the adsorption energy by very little.

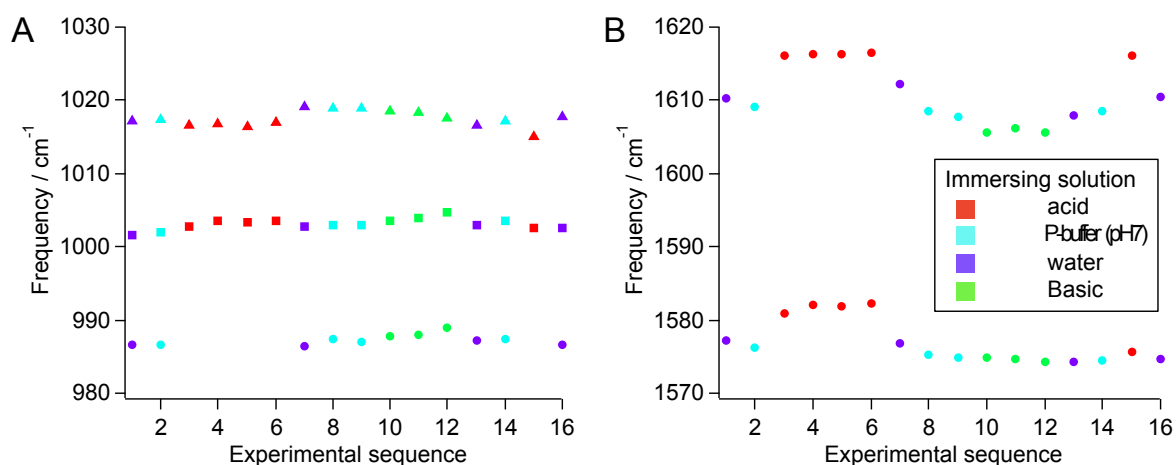


Figure 3.17: Frequency shifts in the ring breathing region (A) and ring stretching region (B) observed during sequential pH changed in 0.1 M H_2SO_4 , phosphate buffer, milli-Q water, and 0.1 M NaOH. The spectra were taken after immersion in each solution for 3 min.

In conclusion, the peaks visible in the pyS SER spectrum are compatible with a pyridine ring plane tilted away from the surface normal, which is the most stable arrangement according to DFT calculations on a Au(111) surface. The detailed microscopic arrangement of the pyS SAM on a roughened gold electrode does not result in any large spectral changes, rather it is manifested by different contributions to the pyridine ring breathing vibration, which we assigned to free, protonated and hydrogen bound species. Their proportions change with both coverage and solvent and we were able to correlate frequency changes with the stability of the aromatic ring. The surface pK_a of pyS must vary by 2 or 3 pH units (similar to literature values [86,106]) depending on the microstructure of the surface, as the shape of the ring breathing peak and the ring stretching ratio vary over a wide range for the same surface preparations. This highlights one of the great challenges of SERS - while it is easy to roughen a surface to produce large signals, it is very difficult to use it for detailed surface science analysis. We shall see in the next section that pinholes in silica coated nanoparticles might be a way forward to create more surface uniformity while still enabling studies at a macroscopic level.

Chapter 4

Metallisation

4.1 Metallisation of self-assembled monolayers

In this chapter, I will investigate the deposition of a metal layer on top of a pyS SAM on gold using SERS and cyclic voltammetry.

Since the emergence of molecular electronics, metal-molecule junctions have been developed to fulfil specific tasks based on the properties of the molecule. For example, rotaxanes can act as a molecular switch in a junction because the molecule itself can change between conductive and non-conductive states. Porphyrins, self-assembled on metal and semiconductor surfaces, can be used for information storage through their multiple oxidation states [128].

Thiols bound to a metal form the basis for many of these devices, because the thiol group reacts specifically with many metals such as gold. To turn this self-assembled layer into a metal-molecule-metal junction, the molecule needs to have a second active functional group, ideally pointing away from the substrate. Several approaches have been used to deposit the top metal layer in order to form large-scale junctions. Many early efforts used metal vapour deposition [129–132], however, in most cases permeation of metal through the SAM could not be prevented. Electrochemical deposition offered more control of the process and is generally

more successful, although metal creeping underneath the SAM is an often-encountered problem [133–142]. A highly successful variation of the electrochemical approach was developed by the Kolb group [42, 43, 47]. The technique is a two-step deposition, where metal ions coordinate to the SAM in metal salt solution before transferring the sample to a dilute metal-free electrolyte for electrochemical reduction. The metal ions serve as nucleation centres for growth of metal clusters, which prevents metal diffusion into the SAM [143] and leads to smaller metal clusters compared to the one-step method [85]. The formation of relatively stable solvent complexes, e.g. $\text{Pd}(\text{H}_2\text{O})_2$, also serves to stop vertical diffusion through the layer and facilitates horizontal diffusion [144]. Alternative successful variants of the technique involve electrochemical reduction in low metal salt concentration [145] or the use of molecular hydrogen for a gentler reduction [146].

The Kolb method used 4-mercaptopyridine (pyS) as a linker molecule, and was shown to work for a variety of metals, namely Pd [47, 147], Pt [42], and Rh [43]. The concept was extended to more complicated structures such as a Au-pyS-Pd-pyS-Pt doubledecker [83] and different linkers such as thiazole [33] or pyridine-terminated araliphatic thiols [84, 145].

The successful formation of a metal layer on top of a pyS SAM has been deduced by a number of techniques. STM detects small clusters on top of the SAM [47] and the $I(V)$ curves are characteristic for a Coulomb blockade by the SAM [148]. X-ray photoelectron spectroscopy (XPS) shows that the deposited metal changes from an ionic to a metallic state by a corresponding shift in binding energy, while variation of the photoelectron detection angle confirms that the deposited metal sits on top of the SAM [42]. Palladium turns out to have unusual properties when deposited on top of pyS. The Pd islands have a binding energy which is different from bulk Pd or Pd deposited directly on gold [147]. Valence band spectroscopy revealed that the Pd layer has a reduced density of states at the Fermi level [33, 78, 149], which could not be explained from the calculated electronic structure of a pure Au-pyS-Pd layer [150]. Interaction of water with Pd could only partly explain the effect. The formation of a N-Pd-O complex significantly reduces the density of states [151], but other Pd atoms in the cluster are not affected by this. It was shown by later DFT calculations that a more likely explanation was the adsorption of atomic hydrogen on palladium [48], which is a well-known hydrogen storage material [152]. Deposition of Pd weakens the Au-S bond, although the effect is negated by co-adsorption with hydrogen [48].

The complexation of metal ions to the nitrogen lone pairs is a critical factor in the process. Since complexation occurs from acidic metal salt solutions, the pyridine nitrogens will be mostly protonated. Poppenberg *et al.* regard protonation and complexation as competitive processes [46], while Muglali *et al.* simply consider the like charge on the SAM and metal cations as a reason for why complexation is considerably slower than self-assembly [84]. Complexation periods of several hours in metal salt solution however allow for metal ion creep underneath the SAM, which is noticeable during reduction because Pd ions in direct contact with gold are reduced at 0.4 V vs SCE, while those on top of the SAM are reduced at -0.2 V vs SCE [47]. Complexation can however be accelerated by applying a potential to the substrate to shift the surface below the point of zero charge [84].

The reduction charge shows that one metal atom is reduced per nitrogen lone pair, corresponding to 0.33 ML for mercaptopyrindine [47,145] and 0.67 ML for thiazole [33]. However, metal atoms are quite mobile on top of the SAM [150], so appear to form small clusters after reduction, freeing some nitrogen lone pairs. Subsequent complexation and reduction cycles were shown to form denser clusters and completely cover all pyS molecules [42,43].

Vibrational spectroscopy of metal-molecule-metal junctions is desirable simply because it shows whether the molecule remains intact and whether any new vibrational modes in the spectrum indicate actual bond formation between a functional group and a metal layer. Moreover, in the context of molecular electronics, it permits detecting the effect of an applied electric field on the molecular structure or any coupling between electronic transport in the junction and vibrational modes. A number of different experimental approaches are used. In inelastic tunneling spectroscopy (IETS) electrons tunneling between a substrate and a tip can lose energy by exciting a molecular vibration, thus tunneling into a different empty electronic state. This inelastic tunneling channel increases the conductance and becomes visible as a peak in the d^2I/dV^2 curve as a function of bias potential. IET spectra were found to agree well with Raman spectra [153], and it could be shown that only longitudinal vibrational modes couple to the tunneling electrons [154]. If one of the contacting electrodes is a semiconductor transparent to infrared light, such as silicon, then total internal reflection IR spectroscopy can be used [155–157], for example to understand the molecular origin of rectification in nitroazobenzene junctions [158].

Sum frequency spectroscopy has been applied to similar systems and has the advantage compared to FTIR that it can reveal the change in molecular order as the metal overlayer is deposited. For example, Asanuma *et al.* found that gold vapour deposition on an alkane SAM introduces a large number of gauche defects, explained by metal creep in these layers [159]. A more common approach to study metal-molecule-metal junctions is gap-mode Raman spectroscopy, which uses the strong electric-field enhancement in a metallic nanogap to detect Raman spectra of few or even single molecules [160–164]. Nanogaps can be created by nanofabrication, deposition of gold nanoparticles or a metallic tip (tip-enhanced Raman spectroscopy, TERS). Molecules have even been deposited at the internal junction of a core-shell nanoparticle [165]. The field of gap-mode Raman spectroscopy was recently reviewed by Marqués-González *et al.* [166]. Many of these studies have focussed on understanding the relationship between junction bias and vibrational spectrum, but surprisingly few have focussed on the fundamental issue of detecting a vibrational signature for the contact formed between the molecule and the top electrode. Huang *et al.* looked at bipyridine SAMs between a gold surface and gold nanoparticles [167] and Zheng *et al.* investigated mercaptopyrindine in the same configuration [120]. Both investigations focussed on changes in the ring stretching region. Huang *et al.* deduced junction formation from a frequency upshift of the C=C stretch, which was attributed to changes in reduced mass as well as changes in the bipyridine orbitals caused by a second gold contact. Zheng *et al.* diagnosed changes in the ratio of deprotonated/protonated C=C stretching intensities as caused by junction formation, with the lower frequency peak representing double-end-bonded molecules and the higher peak representing single-end-bonded molecules. This interpretation was later questioned by the observation that plasmon-induced protonation of mercaptopyrindine is possible in gaps between silver nanoparticles [119].

As far as we are aware, there is only one publication which shows a new vibrational mode when mercaptopyrindine binds to a metal ion. Baldwin *et al.* used evanescent wave enhanced SERS to record the spectral changes which occur when pyS on gold is exposed to different pH or to a metal salt solution containing Cu²⁺ ions [168]. They reported a decrease of the protonated C=C stretch intensity at 1617 cm⁻¹ and an increase of the deprotonated C=C stretch at 1585 cm⁻¹ as the concentration of Cu²⁺ increased, in qualitative agreement with Zheng *et al.* [120].

In addition, Baldwin *et al.* found a new ring breathing mode at 1034 cm^{-1} which grows at the expense of the original pyS mode at 1015 cm^{-1} [168]. This was assigned to a Cu-pyS-Au species by comparison to similar frequency blue shifts observed in Cu/pyridine complexes.

Here we also use SERS to reveal detailed spectral changes in adsorbed pyS caused by electrochemical metal deposition. Starting from confined metal-molecule-metal junctions formed in the pinholes of silica-coated gold nanoparticles, we identify bond formation from frequency shifts in both ring breathing and ring stretching regions, and confirm the assignment by comparison to DFT calculations. We then look at metallisation of pyS self-assembled on a rough gold electrode and by recording spectra from multiple small areas on the same sample we show that successful metallisation is closely linked to successful complexation. We finally combine the results from a large number of both successful and unsuccessful metal deposition experiments to show that success is not clearly correlated to the degree of protonation of the pyS SAM, but instead reduction seems to work better in metal salt solution.

4.2 Metal-molecule-metal junctions in confined spaces

Silica-coated gold nanoparticles (SHINs) have been used in SERS to enhance signals by a confined region of high electric field enhancement [74, 75, 169, 170]. They have become popular in spectro-electrochemistry at single crystal surfaces as the silica layer makes them electrochemically inert. Despite a published protocol [76] it is relatively difficult to grow silica shells which are thin enough to create a high enhancement, but thick enough at the same time to avoid pinholes. Pinholes can be diagnosed electrochemically (see appendix) as the sharp gold reduction peak is easy to detect or by adsorption of molecules such as pyridine or mercaptopyridine which do not bind to silica. While pinholes are a nuisance in electrochemical experiments, they have been used recently to detect trace amounts of cyanide [171] using SERS. Here we use pinholes in SHINs to create more homogeneous and highly metallised pyS layers. SHINs were prepared according to the standard Nature protocol [76], washed, deposited on a piranha-cleaned silicon wafer and dried. The wafer was immersed in 1 mM aqueous pyS solution for 5 min and then washed with milliQ water and

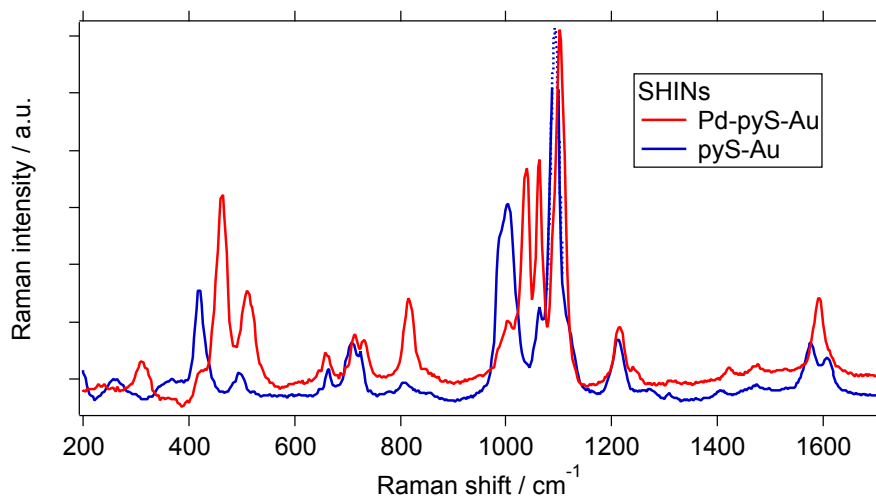


Figure 4.1: Metal-molecule-metal formation in SHIN pinholes. The blue trace shows a SER spectrum of mercaptopyridine adsorbed on a layer of SHINs dried on a silicon wafer. The red trace shows the same layer after complexation in PdSO_4 solution and washing. Spectra are scaled relative to the trigonal ring deformation.

dried. After recording a Raman spectrum, the wafer was immersed in 0.1 M PdSO_4 solution for 15 min, washed and dried. Raman spectra were acquired with the Mini Ram II (B&W Tek) with 785 nm laser. Figure 4.1 shows the numerous spectral changes which occur upon complexation. The ring breathing mode at 994 cm^{-1} drops strongly in intensity and a new mode appears at 1038.5 cm^{-1} , which is similar to Baldwin's observation [168]. The trigonal ring deformation shifts up by 9 cm^{-1} , which indicates a weakening of the Au-S bond. The ring deformation + C-S vibration at 417 cm^{-1} shows a very strong blue shift of 47 cm^{-1} , confirming that the Pd ions are strongly affecting the pyS-Au bond. The Au-S stretch at 262 cm^{-1} disappears and a new vibration appears at 311 cm^{-1} , which could possibly be the Pd-N stretch. The changes in the C=C stretching region are also striking. The familiar peaks for deprotonated and protonated pyS at 1575 cm^{-1} and 1609 cm^{-1} merge into a single peak at 1591 cm^{-1} . The CH in-plane bending mode at 1064 cm^{-1} does not shift, while the in-plane bend at 1211 cm^{-1} and the out-of-plane bend at 810 cm^{-1} shift up by 6 cm^{-1} . The latter mode has b_2 symmetry, so could conceivably indicate a change in orientation of adsorbed pyS upon metallisation. In order to understand the spectral changes better, we calculated the Raman spectrum of Au-pyS-Au^+ and compared it to

the experimental spectra. A double gold junction was chosen, because the insertion of a Pd ion caused technical problems in Spartan 16, which we have not been able to solve yet. Figure 4.2

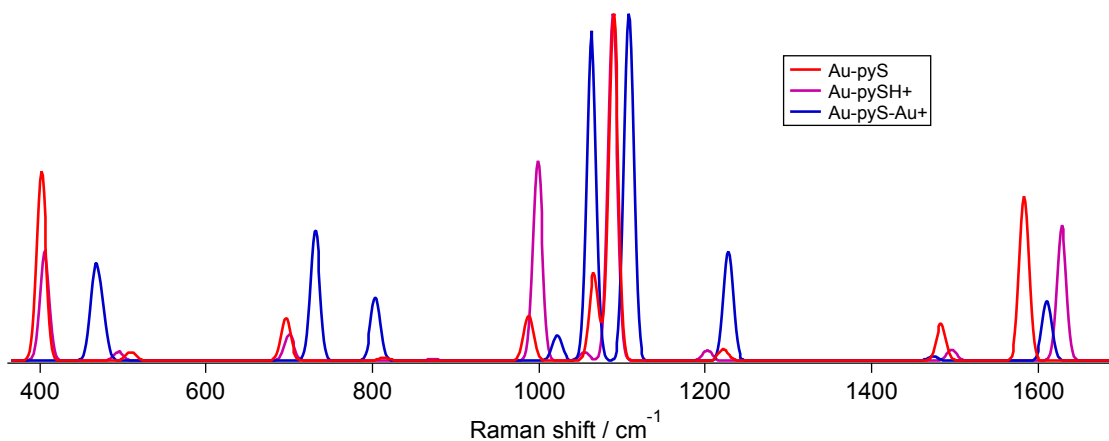


Figure 4.2: Calculated Raman spectra of deprotonated and protonated pyS adsorbed on Au-pyS and a Au-pyS-Au cation.

shows the calculated spectra of pyS-Au, H⁺-pyS-Au, and Au⁺-pyS-Au. Virtually all the frequency shifts seen in the experimental spectra are reproduced by the calculation. The new ring breathing mode is found at 1022.5 cm⁻¹, up by 36 respectively 24 cm⁻¹ from the deprotonated and protonated peaks. The calculation reproduces the intensity increase which accompanies the frequency blue shift of the ring breathing mode, which is commonly attributed to a higher stability of the aromatic ring. The even higher frequency of the sandwich ring breathing mode also indicates increased stability, but the calculation predicts a rather weak Raman mode. The trigonal ring deformation as well as the low frequency deformation + C-S stretching mode are also correctly predicted to blueshift, even though the calculated shifts of 18 and 60 cm⁻¹ are significantly larger than the experimental shifts of 9 and 47 cm⁻¹. Also, the third X-sensitive mode at 700 cm⁻¹ is predicted to shift to 730 cm⁻¹, whereas experimentally hardly a shift is seen. The discrepancy might arise from the fact that we model binding to the gold substrate as binding to a single atom. Since metallisation affects the Au-S bond, which in turn affects all X-sensitive modes, a correct description of the shift can only be expected for a cluster calculation.

The calculation also clarifies the outstanding characteristic peak change in the C=C

ring stretch. Binding to the lone pair generally blueshifts this peak, but unlike in the previous chapter which only looked at hydrogen bonding, we now have a much heavier ion complexed to the nitrogen, which will reduce the frequency simply by its increased mass. This explains the previously discussed work by Baldwin *et al.* [168] and Zheng *et al.* [120]. The former do not show the relevant C=C stretching spectra, while the latter show them at fairly low resolution. The new peak of the metallised pyS shows a relatively strong overlap with the deprotonated peak. If protonated pyS were to preferentially react with the metal ions, then the complexation would show a reduction in the protonated peak and an apparent increase in the deprotonated peak because spectra are recorded at low resolution. Table 4.1 summarises the frequencies of the important peaks in SER spectra of Au-pyS, Au-pySH⁺, and Au/pyS/Au junctions.

Table 4.1: Frequency comparison of key peaks of Au-pyS, Au-pySH⁺, and Au/pyS/Au junctions

Mode	Au-pyS	Au-pySH ⁺	Au/pyS/Au ⁺
Ring deformation + C-S stretch	402	406	466
C-C bend	696	700	732
Ring breathing	988	999	1023
Trigonal deformation + C-S stretch	1009	1089	1108
C-H bend	1221	1202	1228
C-C stretch	1584	1629	1612

4.3 Large-scale junctions

The metal-molecule-metal junction was fabricated on electrochemically cleaned and roughened gold foil (chapter 2.3.3) using the two-step Kolb method. Briefly, mercaptopyrindine was adsorbed from 40 μ M aqueous solution for 15 min, rinsed and then immersed for 30 min in metal salt solutions (0.1 M PdSO₄/0.1 M H₂SO₄, 0.1 M K₂PtCl₄/0.1 M H₂SO₄, 0.1 M RhCl₃/0.1 M HCl). These were rinsed and then transferred to an electrochemical cell at +700 mV and reduced by scanning to -200 mV vs SCE in 0.1 M H₂SO₄. Raman spectra were acquired with the Mini Ram II (B&W Tek), except for 4.7 and 4.8 which were acquired with the inVia microscope

(Renishaw), 50x objective and 785 nm laser. The cell used is shown in 2.16. The complete reduction of metal ion on Au-pyS layer was confirmed by cyclic voltammetry. An example of a Pd reduction cyclic voltammogram is shown in Figure 4.3. The reduction occurred in 0.1 M H_2SO_4 and the potential was initially set at a positive value to prevent spontaneous reduction of Pd [47, 172, 173]. Then the potential was continually reduced at a rate of 5 mV/s until -200 mV vs SCE. The characteristic peak of Pd^{2+} converting to Pd^0 appears at around -100 mV vs SCE, which is similar to Kolb's value of -200 mV vs SCE [47]. Figure 4.3 compares the Pd reduction peak from two samples with different complexation periods in Pd salt solution. Both

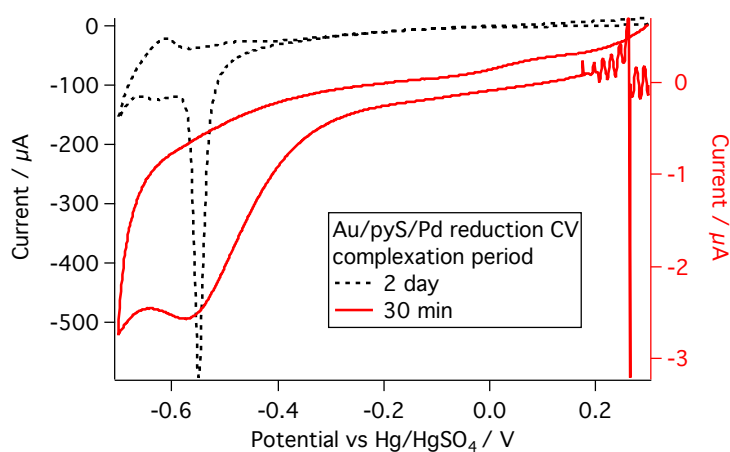


Figure 4.3: Cyclic voltammogram of Pd reduction in 0.1 M H_2SO_4 for two different complexation periods of Au foil-pyS in Pd salt solution.

of them show reduction at the same potential; however, the 2-day complexation gives a sharper and narrower reduction peak than that of 30-min complexation. The narrower peak indicates a more homogeneous layer which reacts within a narrower potential range. However, we need to bear in mind that the longer complexation time leads to the risk of Pd penetrating through the pyS layer and depositing directly on the Au surface. Pd reduction on Au can also give the sharp and narrow reduction peak but this occurs at a higher voltage. Formation of Pd multilayers will also sharpen the reduction peak [174]. The peak after 30-min complexation is broader than the one found by Kolb's group which could indicate a more inhomogeneous gold substrate with a less well-ordered pyS layer. The estimated areas under the 2-day and 30-min peaks are 2505 μC

cm^{-2} and $125.2 \mu\text{C cm}^{-2}$, respectively. Using a monolayer charge of $386 \mu\text{C cm}^{-2}$, it can be estimated that 2-day complexation gives a Pd coverage of around 6.49 ML and 30-min (normal condition) gives a value of only 0.32 ML which corresponds with the pySSpy coverage (0.3 ML). Silien *et al.* recorded a slightly lower reduction charge of $81 \mu\text{C cm}^{-2}$ after 20 min complexation time on pyS [145]. The higher value could be due to overestimating the Pd reduction peak which can be subtracted by the reduction in second cycle.

Apart from electrochemical characterisation, the surface profile of the rough Au electrode before and after metal deposition was observed with an atomic force microscope (AFM). Figure 4.4 reveals the surface topography of Au-pyS (A) and Au/pyS/Rh (B). They clearly illustrate the increased roughness of the Au-pyS layer after Rh deposition. In addition, the phase measurement in Figure 4.4 C and D also shows differences caused by metallisation, which relate to surface properties such as elasticity, adhesion, and friction.

Figure 4.5 compares the SER spectra of pyS-Au layers metallised with Pd, Rh, and Pt. Even though different metals are used, the spectra all share the same characteristic changes seen in the SER spectra of pinhole junctions. A new ring breathing mode appears in the region of $1032 - 1045 \text{ cm}^{-1}$, the low frequency ring deformation + C-S stretch shifts up strongly and a new C=C peak appears between the deprotonated and protonated peaks. For this particular data set, the changes were most apparent for Pd, followed by Pt and Rh, which show similar frequency shifts but not as strong intensity changes. This indicates that more pyS adsorbates were metallised by Pd than Pt or Rh in this case. The frequency of the new ring breathing mode is probably metal-dependent. We have observed an order of $\text{Rh} \approx \text{Pd} < \text{Pt}$, which could indicate that Pt forms the strongest bond and thus stabilises the aromatic ring the most. There has been no systematic investigation of the interaction of mercaptopyrindine with metals, but the interaction between pyridine and transition metals has been thoroughly investigated by the Tian group. They find that the N-M bond length decreases in the order of Pd, Rh, Pt, but do not detect strong dependence of the ring breathing mode on the deposited metal [175]. Instead, they show that the $6a_1$ mode has a frequency which strongly changes with the metal. The equivalent mode in pyS is the \mathcal{M}_{11} mode near 400 cm^{-1} , which shows a strong frequency increase upon metallisation. With Pd, the mode is at 461.5 cm^{-1} , with Rh at 463.0 cm^{-1} and with Pt at 468.2 cm^{-1} (see inset

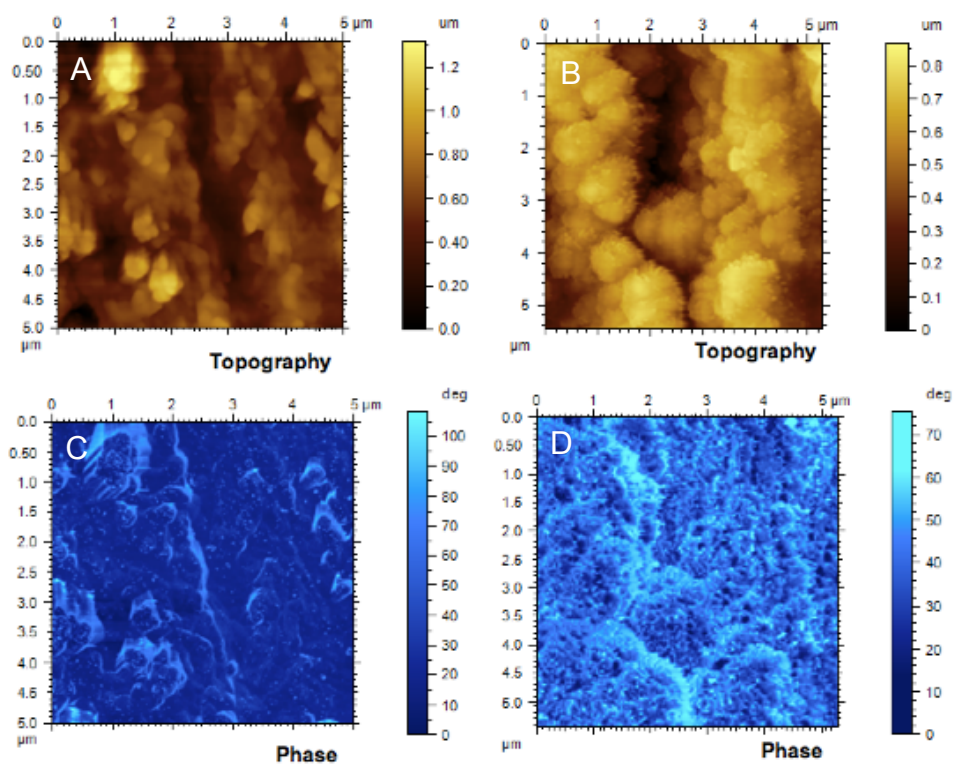


Figure 4.4: AFM image of surface topography and phase of Au-pyS (A,C) and Au/pyS/Rh (B,D). Measurement conducted in KFM mode, tip PPP NCH-Pt, f_q 160 kHz. Image size $5\mu\text{m} \times 5\mu\text{m}$

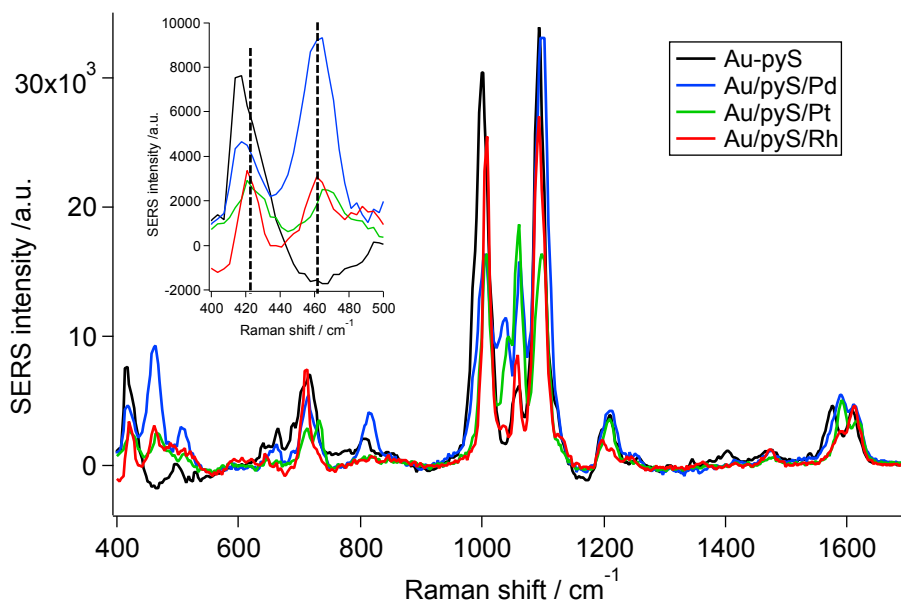


Figure 4.5: Comparison of the SER spectra of successful Au-pyS-metal junctions formed for three different metals.

to Figure 4.5). The DFT calculation by Wu *et al.* [175] finds the equivalent pyridine frequencies in the same sequence and shows that they are proportional to the force constant of the bond.

By detailed inspection of spectra from about 20 metalisation experiments, we finally found characteristic changes to distinguish between successful and unsuccessful junction creation. Figure 4.6(A) shows an example of successful Pd-pyS-Au junction formation, while Figure 4.6(B) shows an unsuccessful metallisation. The successful junction was formed by reduction in a low concentration Pd salt solution (1 mM), which has been shown to work better than the two-step method for pyridine-terminated araliphatic SAMs [145]. The unsuccessful junction was formed in H_2SO_4 , which can lead to the dissolution of Pd ions back into H_2SO_4 solution [174]. This was also confirmed by the cyclic voltammograms in Figure 4.6(C). The reduction in Pd ion containing solution gives a clearer reduction peak than the one in H_2SO_4 . It can be seen that complexation leads to the expected spectral changes, but that the spectrum reverts back to the spectrum of a bare pyS-Au layer upon reduction. This is a general observation we have made: metal ion complexation generally shows the characteristic spectral changes, but the subsequent reduction

is sometimes unsuccessful.

Since the characteristic changes are not metal-dependent, we focus on Rh deposition in the following. We record data with the help of a Raman microscope, with a laser spot diameter of 5 μm , mapping a small area of a roughened sample in 5 μm steps and following the changes in each area after metal ion complexation and reduction. The irregular appearance of the roughened surface under the microscope makes it possible to ensure that the laser spot moves very little from one map to the next so that we can follow spectral changes individual to each 5 μm diameter area. In this way we gained 132 spectra, which we can now analyse with a statistical approach. Figure 4.7 shows spectra for the pyS SAM, after complexation to Rh ions and after electrochemical reduction. These spectra represent the average over all 132 spectra, normalised by the background height at 1150 cm^{-1} and 1545 cm^{-1} respectively. The typical peak shifts caused by metallisation can be seen clearly. These spectra however reveal more detail, partly due to the higher wavelength resolution of the microscope (nominally 1 cm^{-1} compared to 10 cm^{-1} in the portable instrument). The ring breathing peak of pyS free from metal ions increases in frequency after complexation and reduction. Its intensity (compared to either background or trigonal ring deformation) only drops after reduction. The trigonal ring deformation consists of two components and metallisation causes the high frequency shoulder to grow. The C=C stretching peak of protonated pyS increases slightly upon complexation (which occurs in acidic solution), but returns to its initial height after reduction. The C=C peak of deprotonated pyS disappears and a new peak appears at higher frequency during complexation, which slightly shifts up during reduction. We will now analyse the individual spectra to see whether there are any correlations between the degree of metallisation and the initial state of the surface. This analysis touches on one of the key challenges of Raman spectroscopy in general and SERS in particular, namely the relationship between the signal size from a given sample and quantity of material. While doubling the quantity should generally double the signal (as long as molecules are non-interacting), the signal also depends on the laser intensity, the photon collection and detector efficiency and the local field enhancement. While some small efforts have been made to use dye molecules with a known Raman cross section to calibrate the intensity in SERS (eg [176]), approaches to quantitative SERS generally rely on interpreting peak ratios. The problem and its

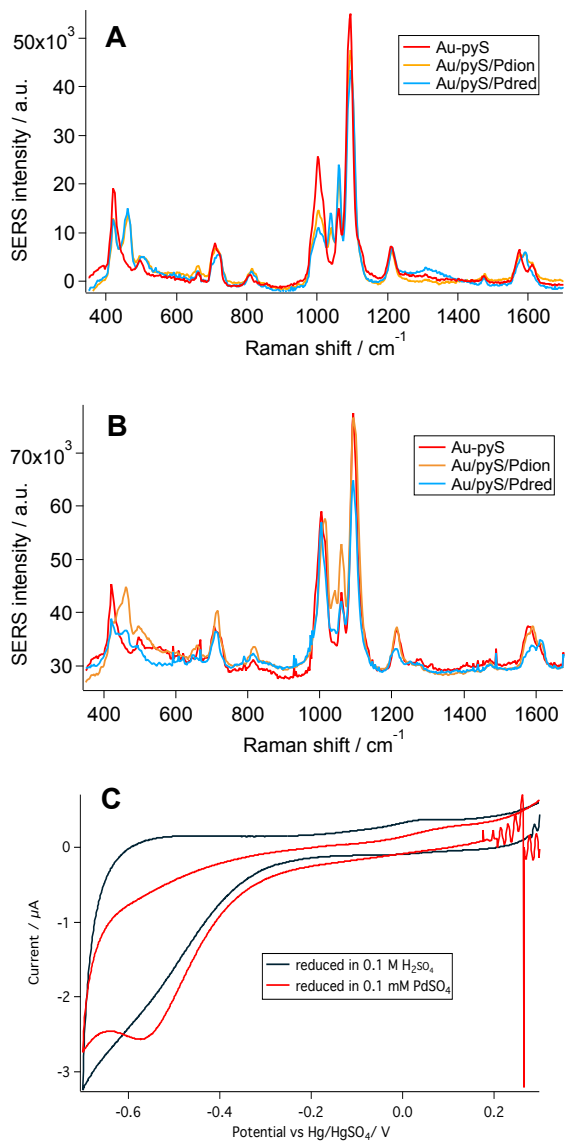


Figure 4.6: Identification of successful (A), unsuccessful (B) metallisation of a pyS-Au layer by Pd. (A) shows SER spectra with final reduction in 1 mM PdSO₄, (B) shows SER spectra with final reduction in 0.1 M H₂SO₄. (C) corresponding cyclic voltammograms of Pd reduction in Pd-containing solution and H₂SO₄.

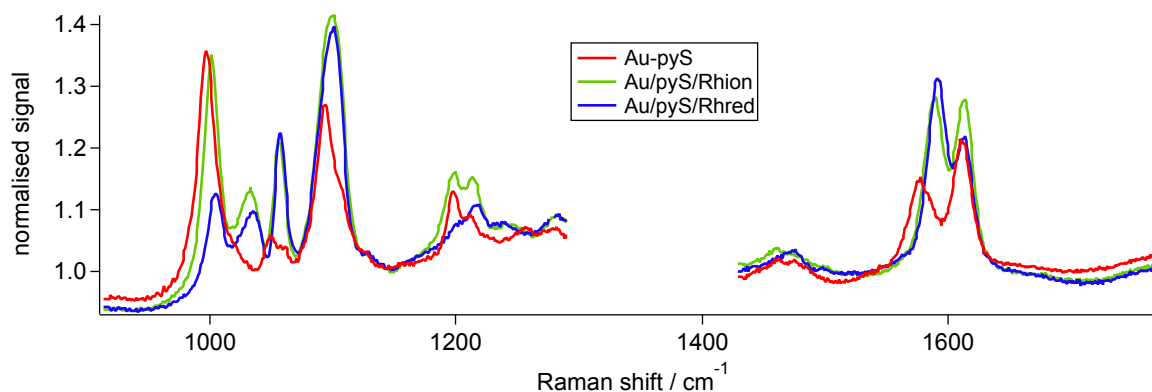


Figure 4.7: Averaged normalised spectra of Au-pyS SAM, after complexation to Rh ions and after electrochemical reduction.

solution can be illustrated for the mercaptopyrindine layer by displaying the data in map format. Figure 4.8(A) shows the large scatter in signal heights for the trigonal ring deformation and the intensity of the SER background at 1150 cm^{-1} and the relatively small scatter if the ratio of two peak heights is calculated, in this case the intensity of the ring breathing mode normalised against the trigonal ring deformation. The scatter in signal heights is purely related to the field enhancement at particular spots as Figure 4.8(B) shows, as there is a clear linear relationship between the peak height and the background signal. This graph shows just how inhomogeneous the SERS activity of the surface is even on a relatively rough scale of a few micrometers. Once the ratio between two peaks is calculated though, it can be seen that it is independent on the local field enhancement as represented by the background intensity (Figure 4.8(C)). This is one of the reasons why peak ratios can be used to follow pH changes in this and other systems, as they are independent of the field enhancement experienced by the sensing molecule. In Figure 4.9 we look at the correlation between two peak ratios commonly used to define the local pH, namely the ratio between the trigonal ring deformation at 1095.5 cm^{-1} and the ring breathing mode at 997.3 cm^{-1} and the two ring stretches at 1577.7 cm^{-1} and 1611.2 cm^{-1} . It can be seen that they are anticorrelated as expected (the ring breathing mode becomes weaker when the local pH increases, the C=C stretch at 1577 cm^{-1} becomes stronger). The linear correlation between them however is not strong, only -0.5 (Pearson's correlation coefficient), which indicates that these ratios do not measure the same physical property. Indeed, the ratio of stretching peaks

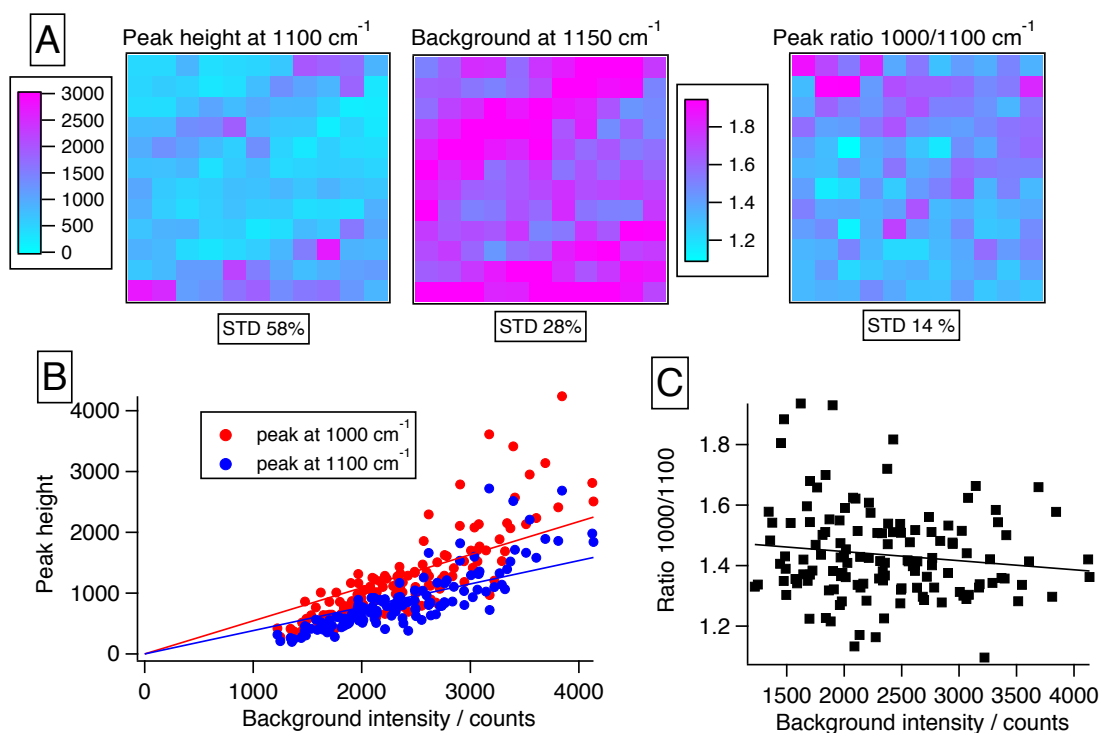


Figure 4.8: (A) Maps of the intensity of the trigonal ring deformation and background Raman scattering and of the peak ratio between ring breathing and trigonal ring deformation. Each pixel represents a $5 \times 5 \mu\text{m}$ area. (B) Plot of peak intensity versus background intensity for each pixel, showing the wide range of field enhancement factors across the surface. (C) Plot of the peak ratio versus background intensity.

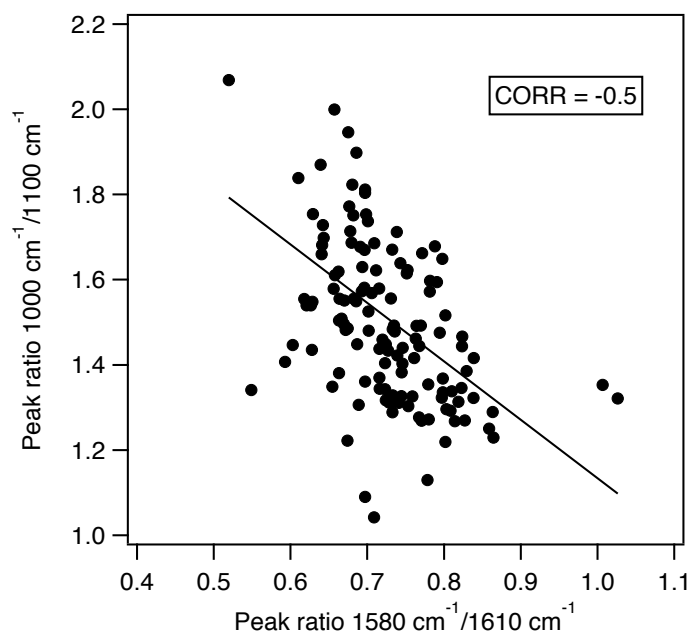


Figure 4.9: Correlation between two peak ratios in ring breathing and trigonal ring deformation regions which commonly used for local pH determination in literatures.

compares the peak heights of two species with distinct peaks. Assuming that positively charged adsorbates have the same Raman cross section as neutral adsorbates then this ratio is a direct measure of the fraction of adsorbates that are protonated. The ratio of ring breathing versus trigonal ring deformation however changes based on a very different effect: protonation changes both the stability of the aromatic ring and the double-bond character of the C-S bond which affect the intensity of both peaks differently.

We can use a similar correlation plot to demonstrate that our peak assignment for complexation and metalisation processes are correct. Figure 4.10 shows the ring breathing modes at 1020 cm^{-1} and 997 cm^{-1} represent the same species as the modes at 1590 cm^{-1} and 1610 cm^{-1} for the complexed and metallised layers. These two ratios have correlation coefficients of 0.8 respectively 0.7 for the complexed and metallised layers, which justifies our assignment of these modes as belonging to the same species in which both 1020 cm^{-1} and 1590 cm^{-1} peaks represents the complexation state of pyS with metal ion.

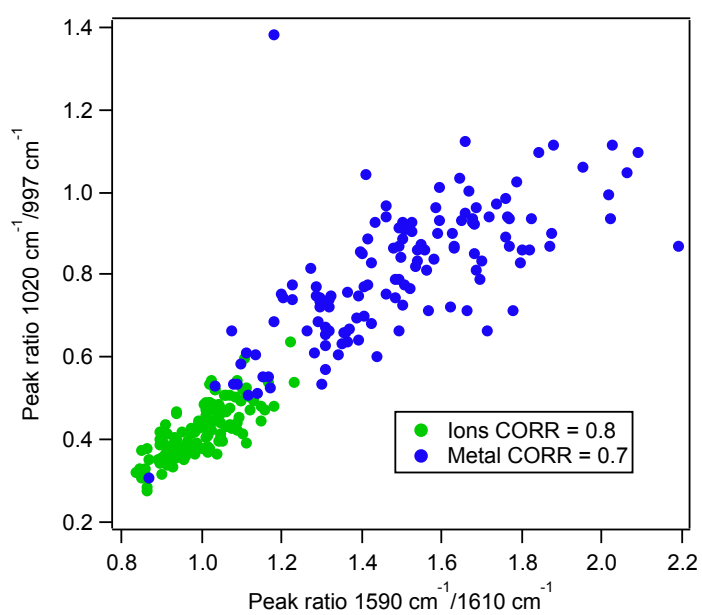


Figure 4.10: Correlation between two new peak ratios in ring breathing and trigonal ring deformation regions which justified by our assignment for complexation and metallisation of metal on pyS layer

We finally test whether the peak ratios in the C=C stretching region before and after complexation and metallisation are correlated as shown in Figure 4.11. The ratio for the metallised layer is weakly correlated to the ratio for the pyS SAM with a coefficient of 0.3. Since the correlation is positive, the implication is that the fewer pyS were protonated in the layer, the more pyS are metallised. This makes intuitive sense as there is electrostatic repulsion between protonated pyS and metal ions in solution, leading to slow kinetics as discussed by Muglali *et al.* [84]. If we can rely on the scaled average spectra in Figure 4.7, then only the deprotonated pyS forms a complex with Rh, since this peak completely disappears while the protonated peak heights before complexation and after reduction are very similar. There is a stronger correlation of 0.65 between the ratios of metal and ion. This confirms that complexation is positively correlated to metallisation, but the value is still far away from 1 and could therefore indicate that other processes play a role.

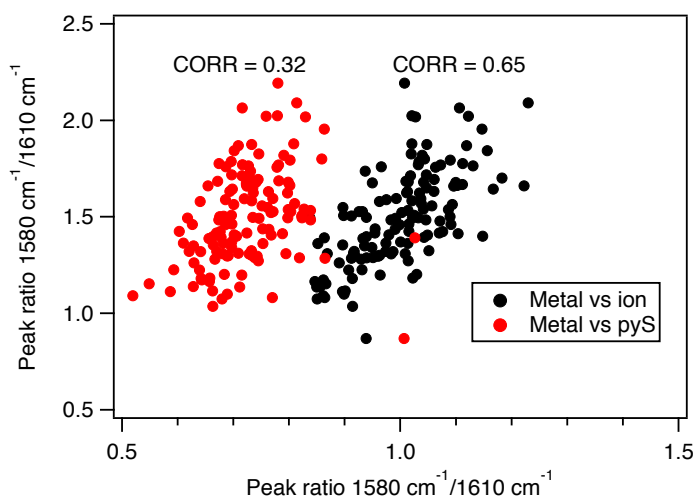


Figure 4.11: Correlation between peak ratios in the trigonal ring deformation. The black dots show the relation between ratio after metallisation (y-axis) and ratio after complexation (x-axis), and the red dots show the relation between ratio after metallisation (y-axis) and ratio of pyS SAM (x-axis)

We finally tried to collate all the different experiments to see whether we could discover which experimental parameters lead to a successful metallisation. Figure 4.12 shows the change in C=C stretch peak ratio ($1580\text{ cm}^{-1}/1620\text{ cm}^{-1}$) going from a pyS SAM to an ion complex

and finally reduced metal. Black markers correspond to reduction in metal ion salt solution, while red markers correspond to reduction in metal ion free (H_2SO_4) solutions. The graph only contains data sets which after reduction show a distinct new ring breathing mode. The reduction in metal containing solution generally increases the ratio, while the one in metal ion-free solution shows a general decrease. In the metal salt containing solutions, the lower the starting ratio (ie the more protonated pyS are present), the larger the final ratio, which now corresponds to a large number of metallised pyS. The range of starting ratios however is very large, which means the degree of protonation does not have a very pronounced effect on the eventual success. In general, the chance of making a successful junction is higher for metallisation in metal ion-containing solution than the metal free solution, which agrees with an observation by Silien *et al.* for low concentrations of metal salt solutions [145]. At higher concentrations, mushroom-type growth occurs, but Raman is not able to detect the presence of Pd islands in direct contact with gold.

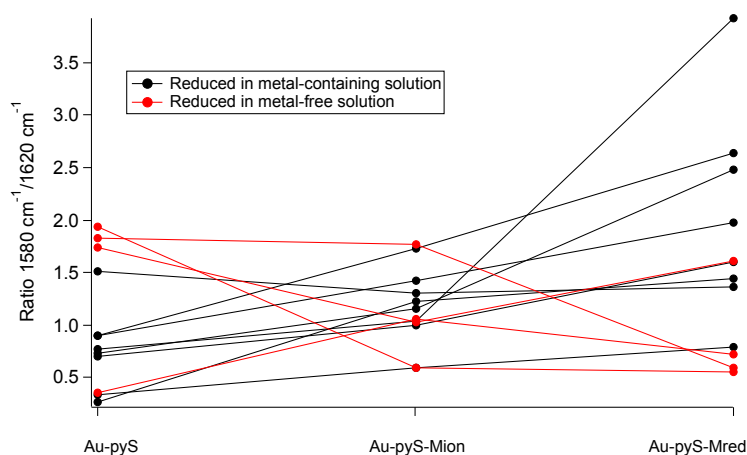


Figure 4.12: Ratio $1580\text{ cm}^{-1}/1620\text{ cm}^{-1}$ of Au-pyS, Au/pyS/Pd ion, and Au/pyS/Pd metal which was electrodeposited in Pd ion containing solution (black) and metal ion free solution (red).

In summary, we have uncovered a distinct spectral signature for pyS bonding to both a gold substrate and a metal overlayer. While the spectral changes (emergence of new ring breathing and stretching mode, shift of X-sensitive low frequency mode) are common for all metals deposited (Pt,Pd,Rh), the frequency shift of the \mathcal{M}_{11} mode shows the same periodic trend as found for pyridine adsorbing on transition metals. Detailed analysis shows that mainly deprotonated pyS is

metallised, but successful junctions can be formed from layers with a wide range of protonation states. The most common parameter in the preparation of successful junctions was reduction in a metal salt containing solution, as previously suggested in the literature.

Chapter 5

Electronic resonances in SERS

5.1 Probing electronic states by SERS

When a molecule forms a chemical bond with an interface, the position of the resulting hybrid frontier orbitals, the HOMO and the LUMO, determines the outcome of a wide range of physical phenomena. In surface catalysis, they reflect the reactivity of an adsorbate [177]. In surface photochemistry, they determine whether electrons or holes are transferred and thereby which bond is broken [178]. In surface-enhanced Raman scattering, they determine whether chemical enhancement via charge transfer takes place, thereby changing which vibrational modes are observed [179]. In single-molecule electronics, they determine how charge flows through the molecule [180]. All these interface phenomena occur in environments spanning ambient to high pressure to liquids, which have a strong influence on the chemistry ranging from changes in catalyst reactivity with pressure [181], to changes in molecular conductance in the presence of solvent molecules [23]. However, little is known about the fate of HOMO and LUMO in environments other than vacuum, as our experimental knowledge is mostly derived from photoemission spectroscopies [182, 183], which measure the density of either occupied or unoccupied electronic states. In contrast, purely optical techniques can access a much wider range of interfaces, but the relationship between the signal and the electronic structure is more complex. Surface-enhanced Raman scattering (SERS)

has been used regularly to determine the LUMO position and direction of charge transfer for a small number of aromatic molecules like pyridine or piperidine by monitoring the enhancement of certain vibrational modes as the Raman photon energy or the surface potential is changed [61].

The principle of the measurement is explained in Figure 5.1. The Raman laser can either cause a charge transfer from the molecular HOMO to an empty state above the Fermi level (molecule-to-metal charge transfer) or from occupied states below the Fermi level to the molecular LUMO (metal-to-molecule charge transfer). The Fermi level can be shifted by an externally applied potential. If a Raman spectrum is recorded with two different photon energies, then a different potential will be needed for each photon energy to cause a resonance and thereby enhance the signal. If the laser causes charge transfer from metal to molecule, then the potential needs to shift to more negative values to bring a lower energy photon into resonance. If charge transfer is in the opposite direction, then the potential has to shift to more positive values to achieve the same effect. For example on silver, piperidine and quinuclidine are enhanced by molecule-to-metal transfer, while pyridine, p-aminothiophenol, and 4-methyl pyridine are enhanced by metal-to-molecule charge transfer [61]. This approach has been used by Shegai *et al.* to study charge transfer in 4-mercaptopyridine adsorbed on silver colloids, whose Raman spectra were found to be enhanced by metal-to-molecule charge transfer [176].

While this approach is regularly being used to find charge transfer states by SERS, interpretation can be difficult because several other parameters can change with potential. Firstly, coverage can change with potential, as we saw earlier during the phase transition of pyS in H₂SO₄ solution. This should be relatively easy to establish, because the Raman signal is proportional to coverage in the low coverage regime and all peaks should increase by the same amount. Only for densely packed layers does the Raman signal saturate or even decrease due to mutual depolarisation of molecules [184–187]. Secondly, the orientation of the molecule might change, for example infrared reflection spectroscopy showed that mercaptopyrindine is further tilted away from the surface normal as the potential is changed from -0.2 to 0.3 V vs SCE [188]. Thirdly, the rough surface could be remodelled at certain applied potential ranges, not only changing the enhancement factor, but also changing local coverage and orientation. As we saw in the detailed discussion in chapter mercaptopyrindine adsorption, it is not easy to discern changes in orientation

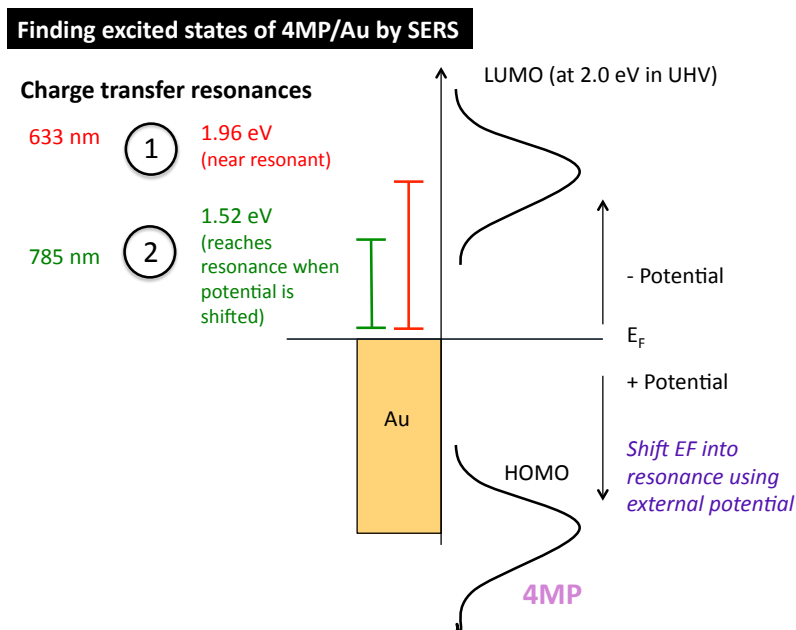


Figure 5.1: Experimental scheme of SERS measurement of Au-pyS molecular electronic state.

of pyS. Previously reported studies define the electronic energy level of adsorbate molecules by looking the characteristic change of Raman spectra [162, 189].

5.2 Experimental

We used an InVia Raman microscope with 50x objective and both 633 and 785 nm lasers. The power used was about 0.4 mW for both lasers, and the spot size of the 633 nm beam appeared to be slightly smaller than the 5 μm of the 785 nm beam. Each spectrum took just under 3 min to acquire. A gold surface was roughened as described in the experimental chapter and a pyS SAM was formed in 1 mM aqueous aldrithiol solution. After washing the sample with ultrapure water, it was placed inside a quartz cuvette with polished bottom face. 0.1 M H_2SO_4 was used, the potential was measured with a Biologic potentiostat using a Ag/AgCl reference electrode. The setup of electrochemical cell is shown in Figure 5.2.

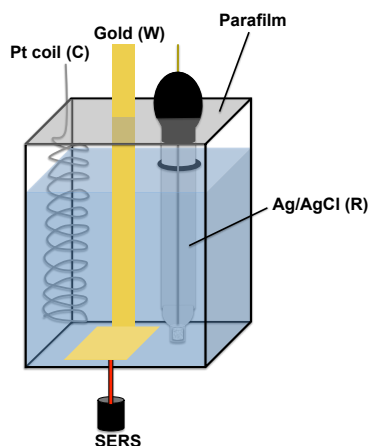


Figure 5.2: Electrochemical cell and SERS setup for LUMO determination experiment

5.3 Results

Figure 5.3 shows spectra of pyS adsorbed on a roughened gold electrode in 0.1 M H_2SO_4 recorded with both 785 and 633 nm Raman lasers as the potential is stepped from + 0.6 V to -0.6 V vs Ag/AgCl. Spectra were acquired with different laser wavelengths at each potential before switching to the next potential. The SERS background changed by up to 50 % during the scan in the negative direction (with an overall tendency to increase), so in order to account for the changing enhancement factor, we subtracted the sloping background from each spectrum first (by fitting a polynomial), and then divided the spectrum by the background intensity at 800 cm^{-1} (the lower end of the spectral range) shown as a function of potential in Figure 5.4. We attribute the changing background to electrochemical remodelling and the results from the previous chapter showed that we can remove this effect by normalising spectra by the background height. There are some common features in the spectra and some differences. The trigonal ring deformation initially increases as the potential is lowered but then decreases to values that are lower than at the start of the scan, while the ring breathing mode shows a continuous increase. The CH bending mode at 1062.3 cm^{-1} decreases with decreasing potential, and a shoulder grows at 1047.6 cm^{-1} , which is probably a different type of vibration (see below). A changeover occurs for the CH bending mode at 1210 cm^{-1} which decreases in height while the one at 1199 cm^{-1} increases.

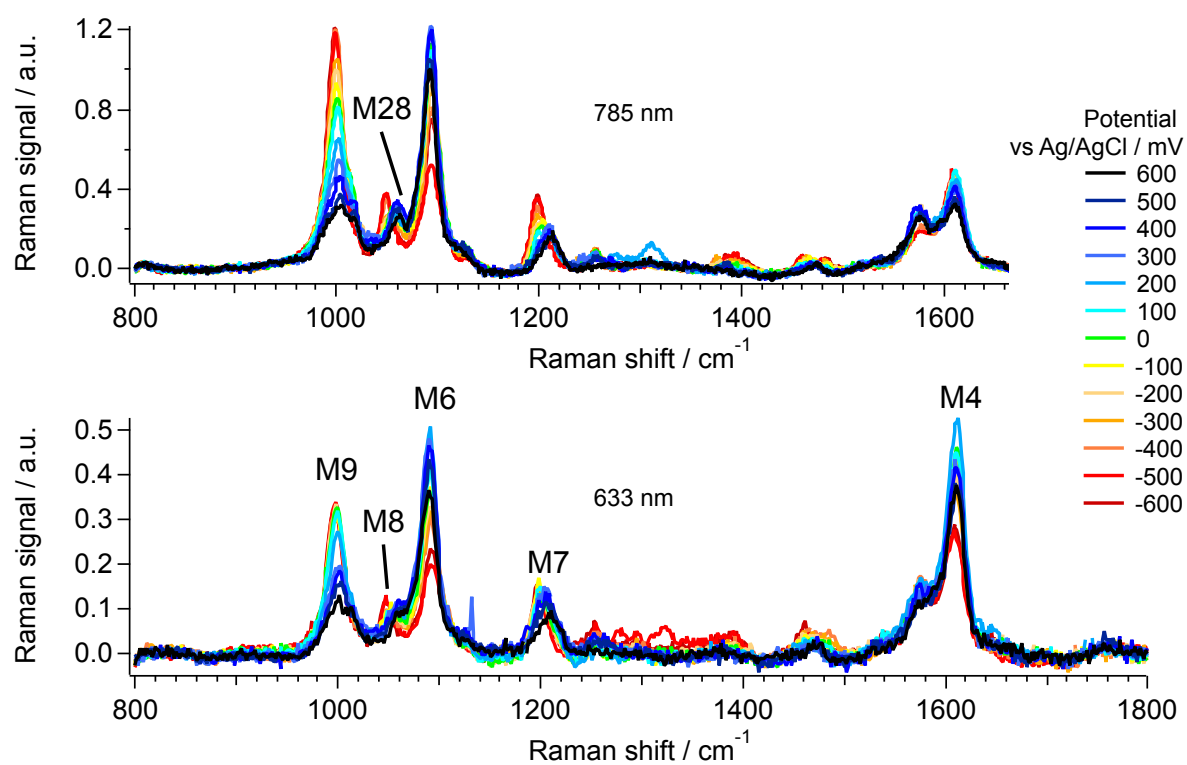


Figure 5.3: SERS spectra of Au-pyS as a function of applied potential. Background has been subtracted and peaks normalised by the background value at 800 cm⁻¹. Peaks are labelled with the Gardner notation introduced in Chapter 3

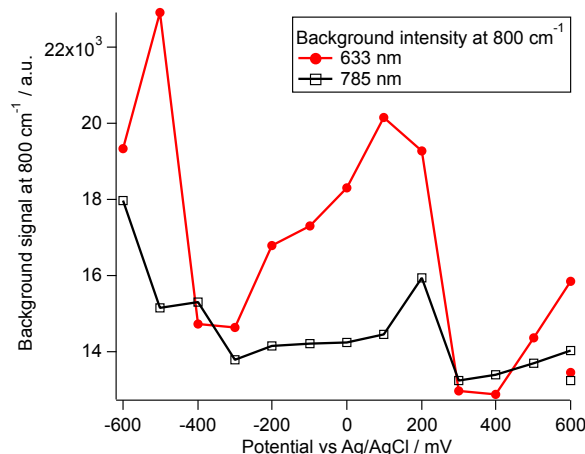


Figure 5.4: Change in the SERS background at 800 cm^{-1} for excitation at 785 nm and 633 nm during the potential scan (lines and markers) and after the potential is returned to + 600 mV (markers).

The intensities of the ring breathing, ring deformation and the latter CH bending mode behave in general during the negative potential scan as if the pH of the surrounding solution decreased. The trigonal ring frequency shows a Stark shift of about $-3\text{ cm}^{-1}/\text{V}$, while the ring breathing frequency shifts by $5\text{ cm}^{-1}/\text{V}$. At the end of the scan, the potential was increased back to 600 mV and the spectra recorded again, shown in Figure 5.5. The background-normalised spectra show an overall higher intensity (by a factor 1.7 for 785 nm and by a factor 1.5 for 633 nm, recorded in this order, ca 5 min between spectra), but they also show that there are fewer protonated pyS than before the scan, as observed for pyS on silver [190]. The increase in intensity could be related to the observed denser packing of the pyS adlayer in H_2SO_4 when the potential is decreased and the different intensity ratios observed at the two wavelengths could be related to a slow restructuring back to a lower density adlayer at the higher potential.

If we plot the fitted heights of all these peaks as a function of potential for both excitation wavelengths, we see that the peaks fall into two categories - those where both data sets show the same dependence on potential and those where the potential dependence also depends on the excitation wavelength. These results are summarised in Figure 5.6. This figure shows that the spectra exhibit a mixture of effects which are either caused by potential alone or by

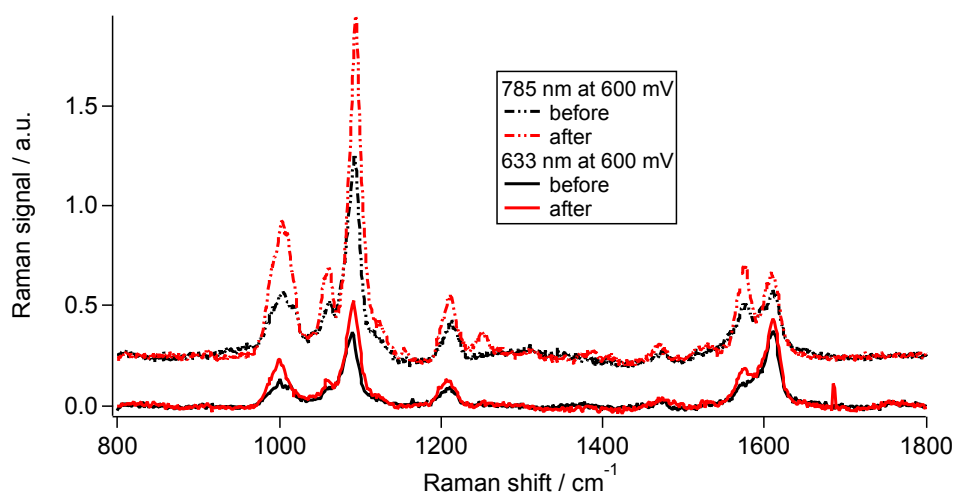


Figure 5.5: Spectra recorded before and after the potential scan at 600 mV vs Ag/AgCl.

a combination of potential and excitation wavelength. The only peaks which show a dependence on both potential and wavelength are those of protonated pyridine (left column in Figure 5.6). The other peaks which only exhibit a dependence on potential show a variety of dependencies. The ring deformation, the in-plane bend at 1211 cm^{-1} and the in plane CH bend + C=S all show a general downwards trend with lowering potential (with perhaps an initial increase). The C=C stretch of pyS is largely independent of potential and the new peak which appears as a shoulder to the in-plane bend + C=S decreases as a function of potential. We actually do not know the identity of this peak. The pH changes shift the \mathcal{M}_8 peak slightly, but not enough to assign this to an \mathcal{M}_8 mode of pyS-H⁺. Coordination of a metal atom does not shift the ring breathing mode up enough to reach the right frequency range. We tentatively assign this to an asymmetric ring mode \mathcal{M}_{28} , as several other modes appear in the spectra, which indicate an orientation change. This makes it clear that the spectra show all possible changes: remodelling, change in protonation, change in coverage, change in orientation and a possible chemical enhancement. The latter two effects are very closely related of course, as chemical enhancement by resonance also enhances modes which are not totally symmetric, and, as we saw earlier, symmetry/orientation changes can have a similar effect. The ring breathing and CH in plane bending mode \mathcal{M}_7 are both excitation wavelength-dependent - at 633 nm, their heights reach a level value at about + 200 mV vs Ag/AgCl, while the height measured with 785 nm shows an almost linear increase with

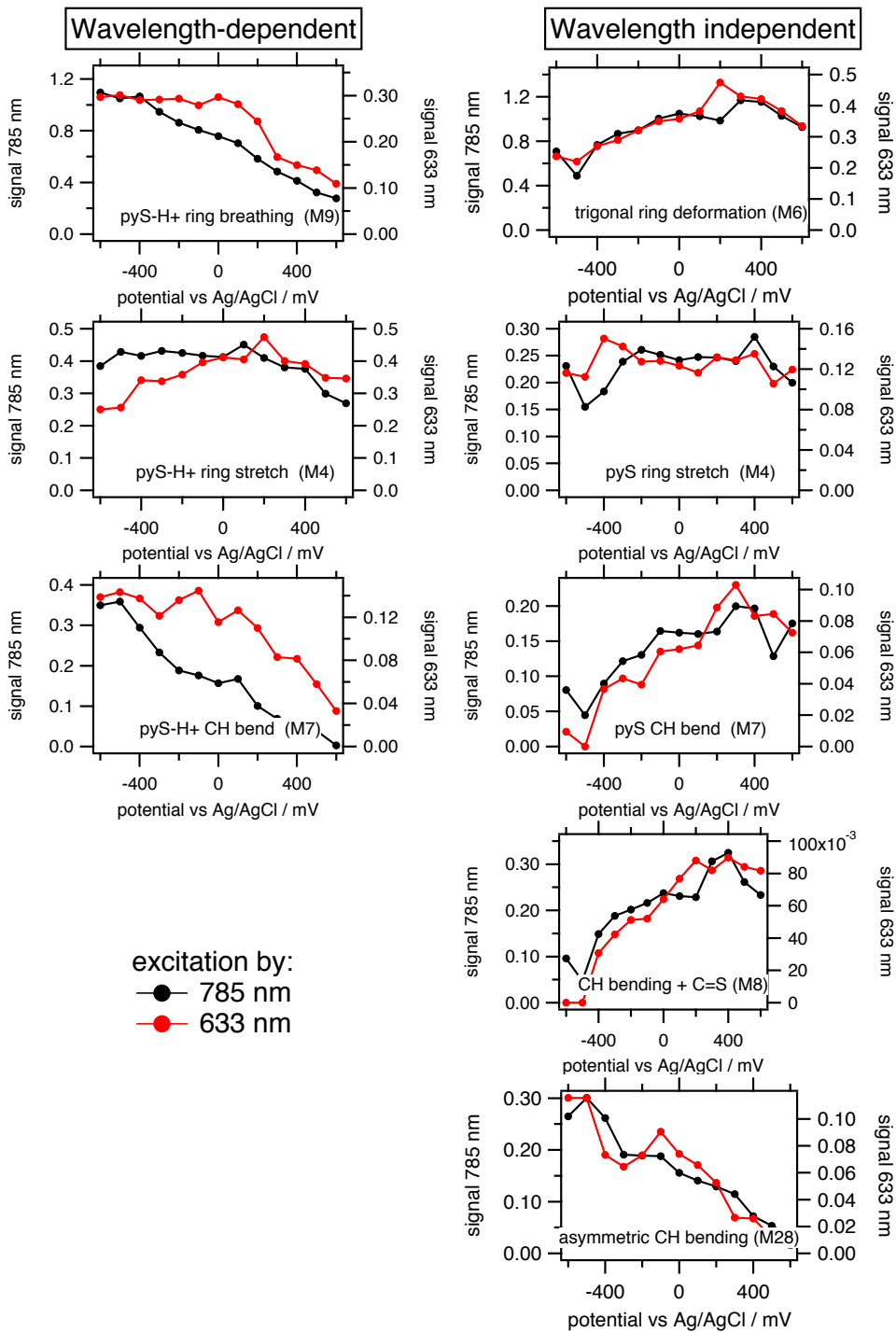


Figure 5.6: Intensity changes of SERS peaks grouped by excitation-dependent and independent types. The Gardner labels refer back to 5.3

decreasing potential. The fact that the lower wavelength reaches saturation at higher potentials than the higher wavelength means we are dealing with metal-to-molecule charge transfer, as suggested also by Shegai *et al.* for pyS on silver [176]. The photon energy difference between these is 0.44 eV, so theoretically if the potential is shifted negative by the same amount, then 785 nm should behave similar to 633 nm. In Figure 5.7 we show the same data set for the ring breathing mode again, only this time, the 633 nm trace is shifted. It can be seen that the traces now show the same trend as a function of potential, which we propose is a resonance with the LUMO of pyS-H⁺. The similarity of the curves when they are shifted merely by the photon energy difference means that the molecule must experience nearly the full potential drop. This is reasonable since the Debye length of 0.1 M H₂SO₄ is about 1 nm, while the height of Au-pyS is about 0.5 nm, so the potential drop does occur on the same length scale as the molecule.

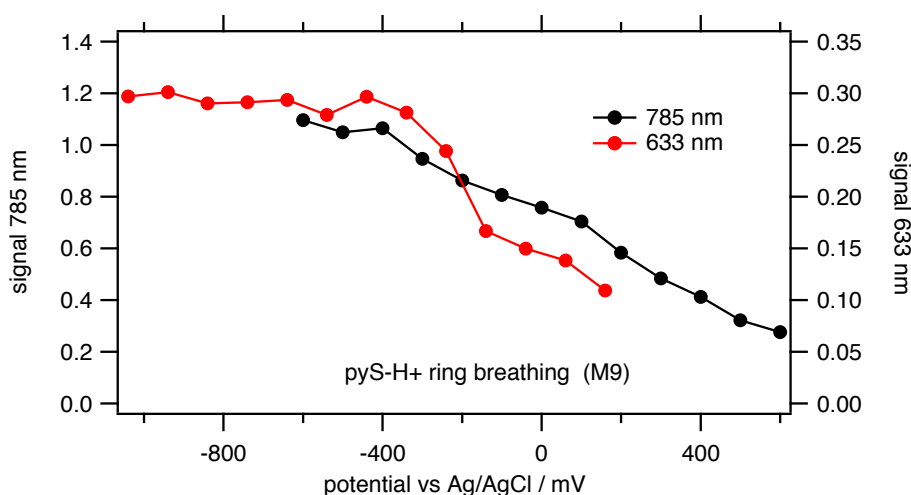


Figure 5.7: Potential dependent intensity of the ring breathing mode measured with 785 nm and 633 nm. The latter trace was shifted down by the difference in photon energies between the two Raman lasers.

The half-way point for 633 nm is about + 200 mV, so the LUMO would be found at 1.92 eV - 0.2 eV = 1.72 eV [191]. This is slightly lower than the LUMO position measured in UHV but for deprotonated pyridine, and at fairly high coverage. While the effect of an electrolyte on the LUMO position is difficult to predict, one would expect a charged species to have a resonance closer to the Fermi level, due to the interaction with its own image charge. Given

that the intensity of the deprotonated C=C peak does not increase at the lowest potentials when probed with a 633 nm laser, the pyS LUMO has to be significantly higher than 2.5 eV. Shegai *et al.* do not analyse their data to deduce the position of the CT state, but from the half way points of their intensity profiles, this can be estimated to be around 2.5 eV. Similar measurements were also carried out for pyS on cobalt and the CT state was found around 3.3 eV [189]. The pyS-Co bond is likely stronger, so it is unsurprising that the LUMO is higher than on silver or gold.

One of the most remarkable difference between the 785 nm and 633 nm data sets is the different appearance of the C=C stretching region. When the same layer is probed with a higher photon energy, the apparent degree of protonation of the surface increases by a factor 2. This already shows in itself that some resonant effects are in play, because the wavelength dependence of Raman scattering alone cannot explain this phenomenon.

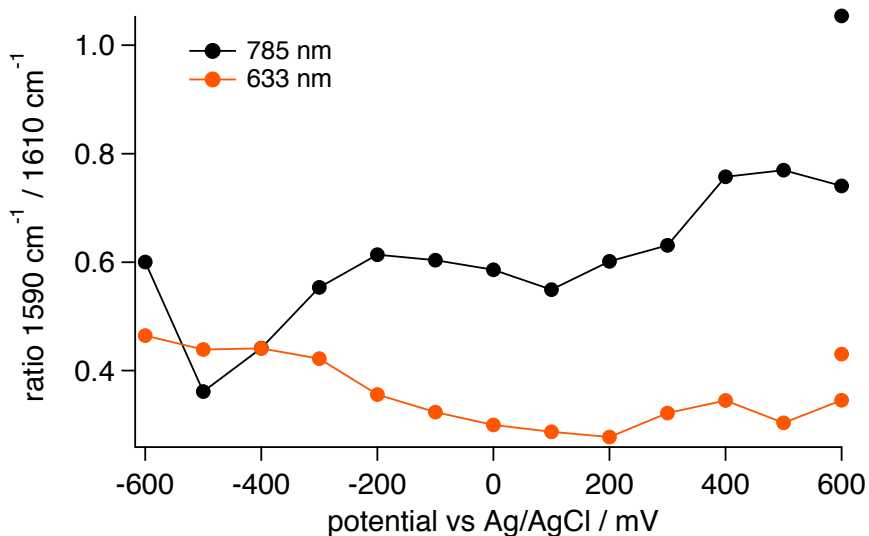


Figure 5.8: The ratio between deprotonated and protonated C=C stretching peak intensities measured with both 785 nm and 633 nm excitation.

How the detected SERS signal varies with wavelength depends on a large number of factors, such as optical properties of the surface used, detector efficiency, optical properties of the objective, mirror coatings etc, which we have little information on. However, as a general rule of thumb, it is known that shorter wavelengths used will overestimate the intensity of bands

at high wavenumbers while longer excitation wavelengths will overestimate the bands at lower wavenumbers [192]. This can be clearly seen in the spectra, but cannot explain the different ratios of the two C=C stretching peaks as their wavelengths are within about 2 nm of each other and we would not expect any of the external factors to change that drastically over such a small wavelength range.

The potential-dependent ratios of deprotonated versus protonated C=C stretching intensity for both excitation wavelengths are plotted in Figure 5.8. The two ratios change in opposite directions and thus become more similar at the lower potentials. The values after returning to + 600 mV are also added to the plot. The very different starting ratios and the subsequent changes are compatible with the protonated species being almost in resonance at the start of the potential scan when a 633 nm laser is used, and gradually shifting into resonance for the 785 nm laser. As these results show, multiple effects contribute to the changes seen with both wavelength and potential. We will discuss their physical origins in the following.

5.4 Discussion

Two basic enhancement mechanisms contribute to SERS, the electromagnetic field enhancement mechanism (EM) and the chemical enhancement mechanism. The former is the most straightforward to understand and will be discussed first.

Since the SER signal depends on the fourth power of the local electric field, even small changes in field enhancement, for example through changes in local surface structure can have a massive effect. It has been shown that a ppm of molecules present at a SERS-active surface can contribute as much as 24% of the signal [193], therefore surface remodelling does not have to occur on a large scale to have a noticeable effect. We showed in chapter 4.3 that it is possible to use the size of the SERS background signal as a measure for the electromagnetic field enhancement. It should be pointed out though that the origin of this so-called nonresonant background in SERS is not fully established. Baumberg's group proposed a model where the SERS background is caused by the creation of electron-hole pairs as the surface plasmon decays [69].

Electron-withdrawing and -donating adsorbates can thus affect the background, because they change the electron density at the surface. This implies that changes in adsorbate coverage can also affect the SERS background. Ikeda *et al.* proposed that chemical enhancement also contributes to the SERS background, because they saw similar potential-dependent changes in background as well as in molecular resonances [194]. For both reasons, our approach of normalising peaks by the background height needs to be justified. Our SER intensities suggest an increase in coverage by 50 to 70% during the scan to -600 mV vs Ag/AgCl (Figure 5.5), while the background intensities for the respective spectra decrease by 18 respectively 6%, i.e. coverage probably does not affect our normalisation procedure. While we observe a general increase at lower potentials with decreasing potential similar to Ikeda *et al.* [162], the overall scatter in the data shows that structural changes on the electrode surface are likely the strongest contribution. It is possible to independently determine the local field enhancement factor by using a dye molecule with a known Raman cross section, for example as applied for pyS on silver by Shegai *et al.* [176]. This is a more thorough approach, but our method is simpler to apply and is certainly applicable to this particular case.

The chemical enhancement mechanism is conceptually relatively simple, both as a Resonant Raman process with transitions occurring between metallic and molecular states and as an enhancement of the molecular polarisability through adsorption. Its existence is much harder to prove though. Generally, the appearance of non-totally symmetric modes is used as an indicator for its existence, but the symmetry of a vibrational mode depends on its orientation, as we saw in chapter 3. The clearest indication of a charge transfer resonance is a difference in the potential energy dependence of mode intensities when the excitation wavelength is changed. This resonance however has two contributions, the so-called Albrecht A term, which is the direct metal-to-molecule charge transfer, and the Herzberg-Teller C term, which is an enhancement of this CT resonance by coupling to an other electronic transition, namely the surface plasmon resonance in this case [195]. Shegai *et al.* suggested that the A term was the dominant contribution for pyS on silver, but since the ratios between different peak intensities also changed with potential they proposed that the C term must be taken into account [176]. In their experiments they did not account for the fact that pyS can exist in both deprotonated and protonated forms

at the surface and that both species can possess different CT resonance energies. They also did not account for the fact that changing the potential affects the strength of the pyS bond to the substrate. Lowering the applied potential on a pyS SAM has the overall effect of weakening the

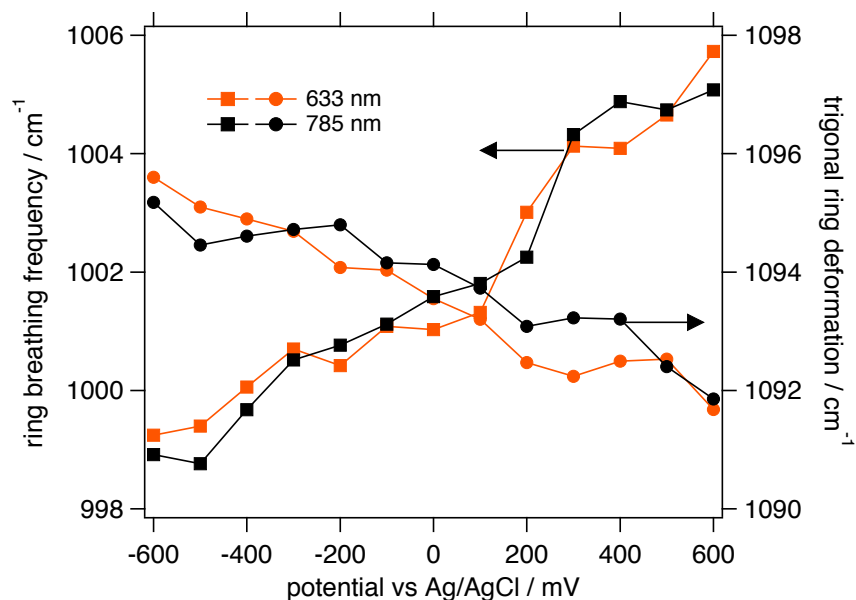


Figure 5.9: Stark frequency shifts of ring breathing and trigonal ring deformation modes measured with both 785 nm and 633 nm excitation. 633 nm data have been shifted by + 2.5 cm⁻¹ to account for a difference in wavelength calibration.

bond between the gold surface and the adsorbate. PyS desorbs at - 0.7 V vs Ag/AgCl and while our scan ends at potentials slightly positive of the reductive desorption, it can be seen from the Stark shifts of ring breathing and trigonal ring deformation modes in Figure 5.9 that the bond is affected. Both ring breathing and trigonal ring deformation modes shift towards values that are closer to crystalline pyS, namely towards 991 cm⁻¹ and 1104 cm⁻¹. The weakening bond at lower potentials also becomes visible in the increasing ratio between ring breathing and trigonal ring deformation modes, which was first observed by Taniguchi *et al.* [196], who reported that the spectra could be obtained reversibly with respect to the potential. Similar relative intensity changes were also recently reported by Bron *et al.* [107], who changed the potential from negative to positive values. Such bond weakening would help in a rearrangement of the pyS layer caused by bisulfate ions. This could not be observed by Taniguchi *et al.* or Bron *et al.* who used HClO₄

and KF, respectively, as electrolytes.

As far as orientation changes are concerned, the appearance of several b_2 modes in the 1300-1500 cm^{-1} region makes it likely that the pyS ring plane twists to either yield a completely asymmetric orientation with respect to the gold surface, or C_s symmetry where the ring plane is perpendicular to the gold surface (see Figure 3.2). Some early infrared experiments indicated that pyS should be more upright at lower potentials, although the quality of the absorbance spectra was relatively low [188].

Chao *et al.* carried out similar potential-dependent scans for pyS adsorbed on roughened silver. They observed irreversible changes after a scan to negative potentials, which they attributed to a conversion of upright to flat-lying pyS [190], characterised by the appearance of an additional peak in between ring breathing and ring deformation modes (similar to the mode we assigned as \mathcal{M}_{28} above) and a frequency downshift of the protonated C=C stretching mode from 1621 to 1604 cm^{-1} . Similar experiments were later carried out by Shegai *et al.* [176], who concluded that the permanent change seen by Chao *et al.* [190] was likely due to a remodelling of the electrode surface rather than a reorientation of the molecule.

In order to disentangle the various effects, the following experiments could be performed. The use of a Au(111) substrate and field-enhancement via SHINs could remove the effect of surface remodelling on the spectra. Potential-dependent spectra in electrolytes of very different pH value could help isolate changes in protonated and deprotonated pyS. The use of an ionic liquid as electrolyte could expand the potential window and allow to detect electronic resonance effects more clearly. The comparison between SERS and reflection-adsorption IR spectra could disentangle orientation changes from electronic effects.

Chapter 6

SFG of 4-mercaptopyridine on gold

6.1 Introduction

Sum frequency generation (SFG) is a useful technique to study interfaces since it is non-destructive, provides high sensitivity and high time resolution. Most importantly, it is intrinsically sensitive to surface properties. Moreover, coupling this spectroscopy with a pump-probe technique can give information about real time phenomena on picoseconds or faster [28]. Therefore, the original idea for this project was to not only to create molecular sandwich layers, but to also probe electron transfer across the layer with the help of femtosecond pump-sum frequency probe spectroscopy. No prior studies of mercaptopyridine adsorbed on gold exist, although thiol SAMs have been a frequently studied adsorbates, because the order of the layer and the existence of gauche defects can be easily seen by SFG [197, 198].

6.2 Molecular vibrations and relation to electron transfer

In order to make an efficient molecular electronic bridge for specific usage, we have to understand comprehensively how electrons transfer across molecules in the junction. There are two basic possibilities either by direct tunnelling, in which case, the main effect of the molecule is to keep

the two junctions a certain distance apart, or by hopping, in which case, the electron is transferred using an unoccupied molecular level as an intermediate state. Interactions of travelling electrons with environmental fluctuations cause energy dissipation. This dissipation is affected by many factors including temperature, size and complexity of the molecular bridge [15, 16]. As described in [15, 16], the interaction of electrons with molecular vibrations is known to be an important source of inelastic contribution to the electron transport.

The basic idea is that when an electron transfers to a certain (for example, unoccupied) state of the molecule, this transfer will couple to a vibration if the vibrational mode effects this electronic state. For example, looking at the normal mercaptopyridine LUMO in Figure 6.1, the electron wavefunction stretches across the C=C bond, which lengthens and shortens for the \mathcal{M}_4 vibrational mode, so we would expect this vibration to be affected by and in turn affect electron transport via the LUMO. In contrast, if charge transport occurred in the form of a hole, then we need to look at the HOMO. The HOMO wavefunction has a node on the C=C bond, so hole transport is probably unaffected by the C=C vibration.

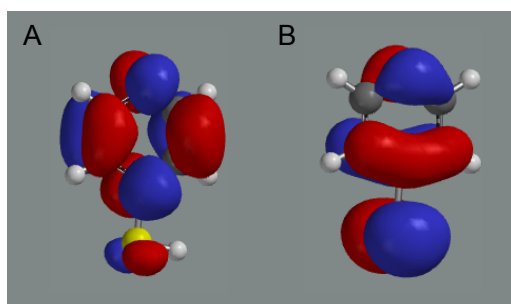


Figure 6.1: 4-mercaptopyridine LUMO (A) and HOMO (B) orbitals. The LUMO orbital lies across C=C, therefore if charge transfer occurs via the LUMO, it should couple to the C=C stretching vibration. On the other hand, the HOMO orbital has a node on the C=C bond, so transfer via the HOMO should not couple to the C=C vibration.

Electrochemical measurements are normally too slow to follow such coupling, as the fastest measured timescale is of the order of nanoseconds, but it might be possible to watch coupling between electrons on the molecular bridge and molecular vibrations via pump-probe spectroscopy.

In order to follow electron transfer in real time, the SAM layer would be excited with photons from a femtosecond laser pulse and the effect on vibrations would be probed with a time-delayed SFG probed. As shown in Figure 2.12, after the metal surface is exposed to a short laser pulse, so-called nascent electrons are created up to the photon energy. Within 100 fs, they form an equilibrated hot electron bath. The electron bath then equilibrates with surface phonons within ≈ 1 ps. If the vibrational spectrum changes on a similar timescale of around 1 ps, it is clear that these hot electrons are causing the changes, while any changes occurring on much longer timescales will be due to phonons, that is just a hot surface [28]. Because of a large variety of technical problems with the femtosecond laser, very little time was available to do these experiments in this thesis, so the following results represent a sketch of what is possible.

6.3 SFG of 4MP on gold

In order to do SFG measurements, a Au(111) surface (ArrandeeTM, Germany) was immersed in 40 μ M pyS/water solution for 15 minutes. For the complexation, pyS-Au was soaked in 1 mM PdSO₄ solution for 30 min followed by reduction in 0.1 M H₂SO₄ as described in the experimental chapter.

In the pyS-Au spectrum, only two peaks are really clearly visible, and a fit results in two vibrational resonances at 3003 cm⁻¹ and 3058 cm⁻¹ shown in Figure 6.2. The broad peak around 3150 cm⁻¹ represent of the nonresonant background of the gold surface, where surface electrons near the Fermi level produce the sum frequency. The width of this peak reflects the spectral width of the IR probe pulse. The Spartan calculation predicts two symmetric CH stretching vibrations at 3104 cm⁻¹ and 3155 cm⁻¹, ie the frequency separation fits well, only the absolute frequencies do not. Frequency calibration of this SFG spectrum was done by passing the IR through the plastic window of an envelope (polystyrene) which was calibrated on a transmission FTIR instrument. Since both the polystyrene calibration and the Spartan calculation might be off in absolute terms, the agreement is satisfactory. Both peaks appear to have a shoulder, but this is not easy to fit. When a comparable sample is metallised, then several changes become clear: the nonresonant

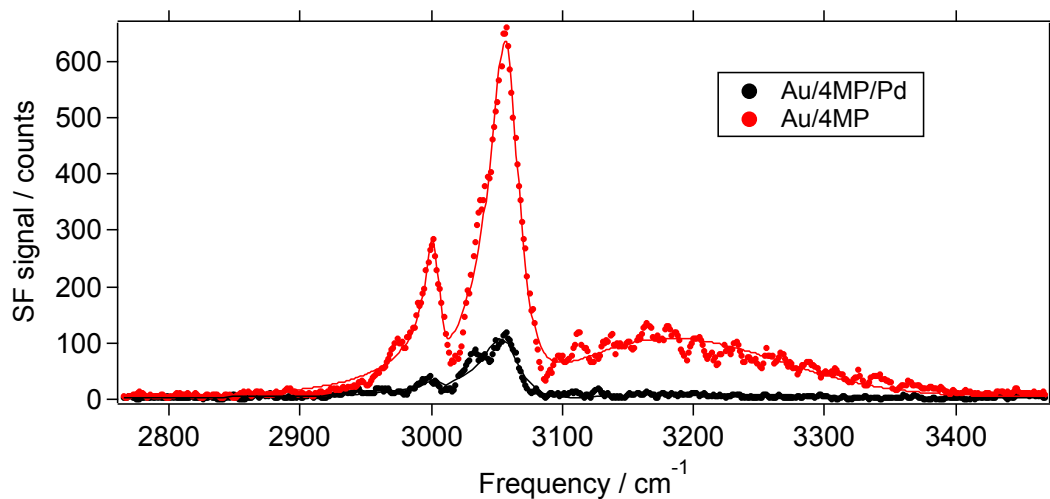


Figure 6.2: Sum frequency spectra of the C-H stretching region for a pyS SAM without and with Pd overlayer.

background is much reduced with respect to the previous spectrum, and the vibrational peaks are much smaller. The first observation could be related to a reduced density of states. We cannot tell from the CH stretching region whether this sample was successfully metallised or not. If it was, then the Pd islands on top of pyS-Au could have a lower density of states than Au, even though Pd has a high density of states due to the Fermi level within the d-band. In the literature, this effect was explained by the propensity of hydrogen to bind to Pd [48]. It is also possible that any Pd clusters created were simply oxidised, either in air on their own, or assisted by the intense laser irradiation. Oxidation of a metal would also lower the density of states and thereby the nonresonant signal. The reduction of the height of the vibrational peaks indicates either that this sample was less ordered than the other one to start with or that the order of the SAM was reduced on metallisation. While clearly much more would need to be done to prove these ideas, these two spectra show the potential information which can be gathered from SFG.

SFG is also able to detect the C=C stretching vibration as shown in Figure 6.3. In this spectrum, the nonresonant background was removed by delaying the upconversion pulse by 1 ps to only detect the oscillating polarisation of the molecule, not the surface electrons [199]. Both SFG and SERS show two peaks, although the exact positions and linewidths do not fully

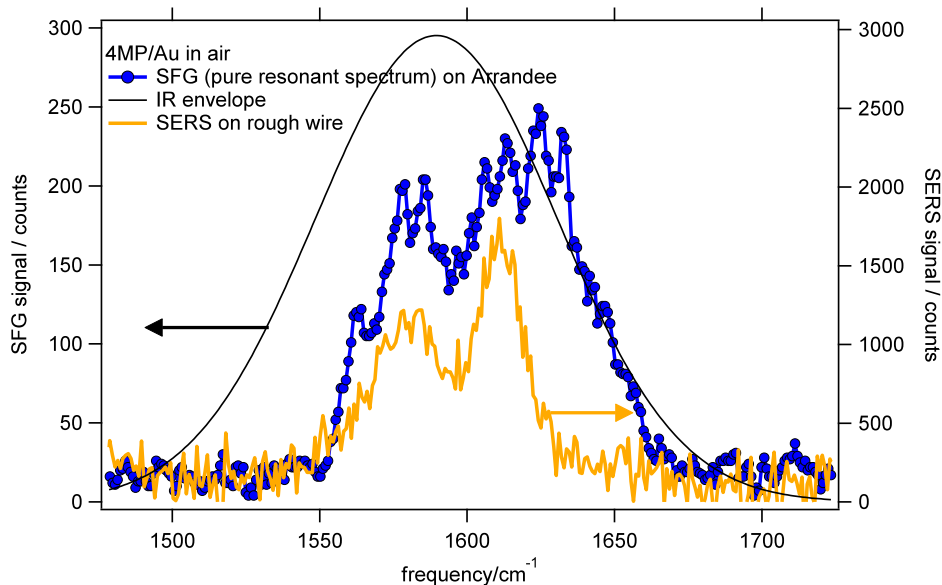


Figure 6.3: Comparison between SFG and SERS spectra of the C=C stretching region of pyS-Au. The thin line shows the intensity envelope of the IR probe pulse.

agree. The SFG wavelength was calibrated by comparison of a bare gold spectrum to an air IR spectrum - both show dips due to water vapour absorption. The spectrograph was calibrated with the help of a neon lamp, but the SFG wavelength is around 709 nm for this spectrum and only two neon lines were available for calibration, ie the change in wavenumbers between pixels on the detector might be slightly wrong. The SFG spectrum was obtained on an almost atomically smooth surface, while the SERS spectrum was acquired on a roughened gold foil. To record this SFG spectrum, the nonresonant signal was reduced by delaying the visible pulse. In the ideal case, this gradually reduces the amplitude of the nonresonant background without shifting it. But when we record an SFG spectrum with slightly different IR excitation wavelengths, as shown in Figure 6.4, we can see that while the lower peak stays roughly in place at 1580 cm^{-1} and only changes height, the higher one grows broader if we excite at higher wavenumbers. This could be due to a reduced nonresonant background even at this long time delay, which shifts to the high frequency side due to some misalignment in the femtosecond laser. These experiments were done in air, and while water absorption is a general problem in this region, the C=C stretch happens to fall inside a small region where little light is absorbed by water.

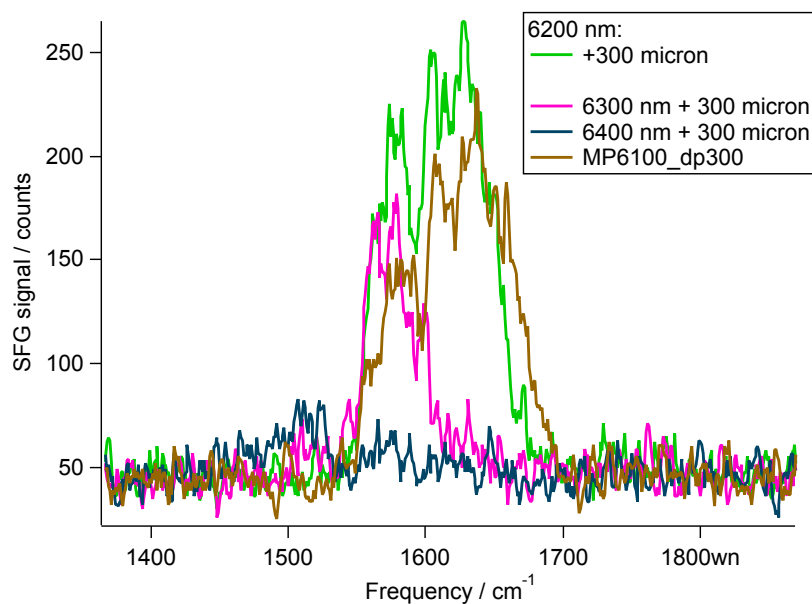


Figure 6.4: SFG spectrum of pyS-Au recorded at different infrared center wavelengths.

6.4 Pump-probe

Generating a good enough alignment of the laser for a good C=C spectrum is difficult, but while setting up for pump-probe experiments, we noticed a phenomenon which can be detected more easily. When mercaptopyridine is adsorbed on a gold sample, the effect of an 800 nm pump beam is to reduce the nonresonant Au background. If the surface is cleaned, no comparable signal reduction is seen. The NR background is reduced on a similar timescale as the hot electron distribution is expected to cool down (a few picoseconds), so the cause of this transient could be that the presence of the molecule makes the surface nonlinear susceptibility temperature-dependent [200, 201]. Alternatively, the transient could be caused by an electronic excitation of the molecule by a pump pulse. In order to test for this, we recorded pump-probe spectra at a constant delay time of 0 ps (the maximum effect above) and varied the energy of the SFG probe by selecting different IR wavelengths. Figure 6.5 shows the size of the signal reduction as a function of SFG photon energy.

For example, for 6 μm IR wavelength, the SFG photon energy is 1.75 eV, scanning

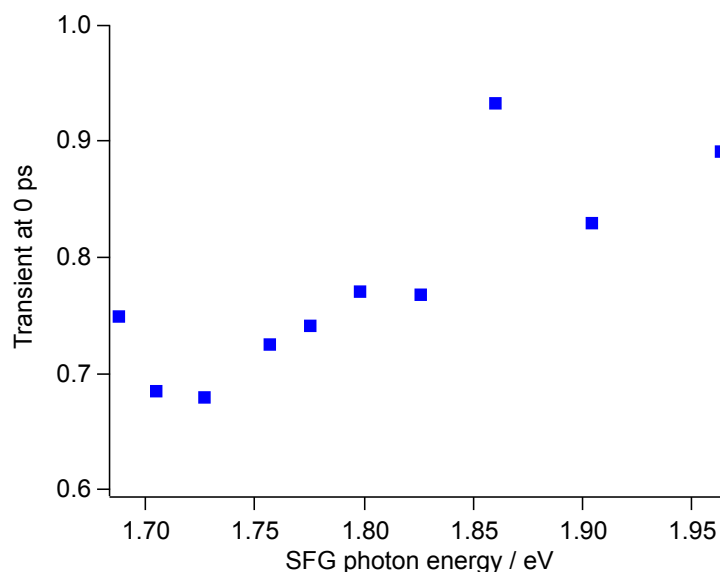


Figure 6.5: Transient reduction at 0 ps as a function of the SFG photon energy.

to shorter IR wavelengths ($3 \mu\text{m}$) increases the energy to 1.95 eV. At these higher energies, the effect of the pump disappears. This means that the cause of the transient in Figure 6.6 is not thermal, but has to be electronic. It is possible that the SFG photon is resonant with an electronic transition, for example the Fermi to LUMO transition, which was found at 1.7 eV in the previous chapter. A possible explanation for the transient would be that excitation into the pyS-Au LUMO strongly affects the nonlinear response of the surface. In order to confirm this, one would need to repeat these measurements under electrochemical control by shifting the Fermi level and seeing whether this response curve shifts in energy as well. Or one could adsorb mercaptobenzene or another thiol, which would have a LUMO at a different energy and see whether this effect disappears. In summary, these results show that the original idea for this thesis of observing coupling between excited electrons and molecular vibrations is feasible. The challenges to overcome are firstly a more reliable laser system, purging of the beam path with dry air to obtain higher IR pulse energies, a more thorough study of the vibrational spectrum and finally detecting a vibrational signal during the pump-probe.

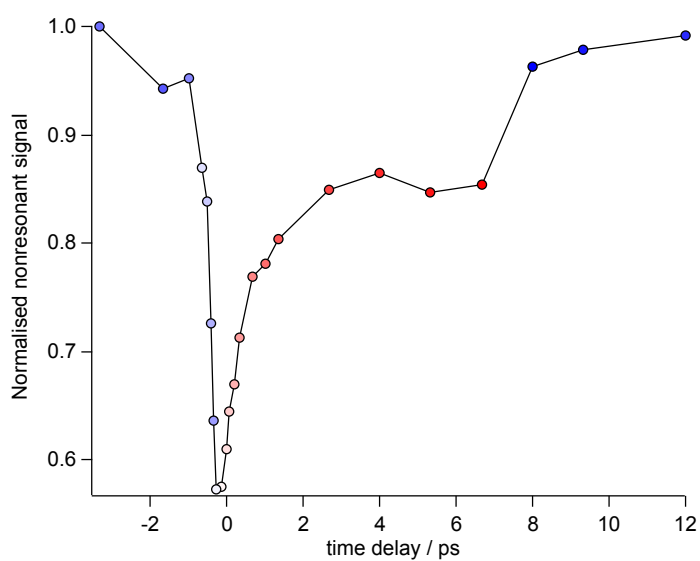


Figure 6.6: Change in the nonresonant background of a pyS-Au sample as a function of time delay between an 800 nm pump pulse and an SFG probe. Data points were acquired in sequence from red to blue, the step at 8 ps time delay is probably caused by a change in alignment during the scan.

Chapter 7

Conclusions and future work

This thesis achieved a detailed insight into the vibrational modes of 4-mercaptopyridine on gold, in particular the effects of coordinating a proton or metal ion to the nitrogen lone pair. Metal-molecule-metal junctions were fabricated electrochemically and a spectral signature for successful coordination was found. Raman spectroscopy coupled to electrochemistry was used to determine the location of the LUMO of protonated mercaptopyridine, and several factors were identified from the spectra which are not caused by charge transfer. In order to identify higher-lying charge transfer states of deprotonated mercaptopyridine or metallised mercaptopyridine layers, either a higher energy laser should be used or experiments could be carried out in a different electrolyte which allows to shift the potential over a wider range. A full understanding of all vibrational modes and the electronic structure of each species is fundamental knowledge for using mercaptopyridine as part of a molecular electronic junction.

After showing the general feasibility of carrying out SFG experiments on this molecule in form of pump-probe spectroscopy, future work can determine the actual timescale of coupling between excited electrons and the molecular vibrations in an electrochemical cell. The next step would then be to investigate junctions with different functions such as redox-gated molecular junctions or molecular switch junctions. For the redox-gated molecular junction, the molecular bridge can be changed in its redox state by an applied potential. It would then become possible to

investigate the influence of the redox state on the electron-vibration coupling time. Alternatively, a molecular switch which has at least two stable structures which can be changed by pH, light, temperature, or electric current, could be investigated. In this way we can begin to understand fundamental relationships between molecular structure and electron transfer from the point of view of vibrational spectroscopy.

Chapter 8

Appendices

8.1 Spartan calculations

In order to test our Spartan calculations, we calculated a range of molecules for which detailed theoretical Raman spectra have been published, namely those by Birke and Lombardi and Gardner *et al.* [87,113,202]. Figure 8.1 shows the success of these calculation. Each figure contains a plot of our calculated frequencies versus the published frequencies for fluorobenzene, chlorobenzene, pyS-Ag, and the pyS anion. Especially the latter shows that binding to a single metal atom is good enough to obtain frequencies close to those calculated for a whole cluster.

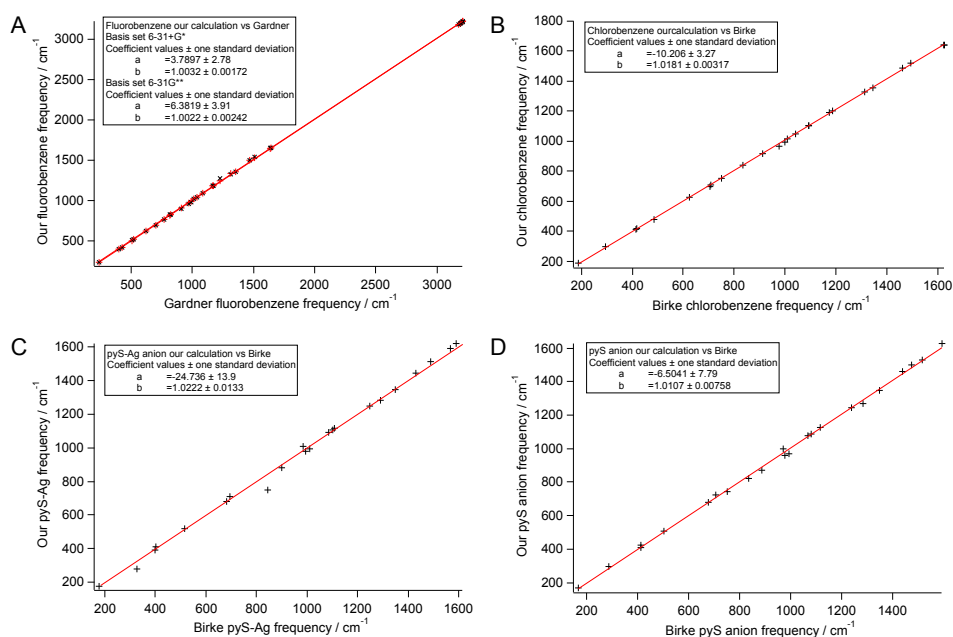


Figure 8.1: Correlation plots compare our experiment to published papers [87, 113, 202] of (A) fluorobenzene, (B) chlorobenzene, (C) pyS-Ag, and (D) pyS anion.

8.2 Electrochemistry of gold

The cyclic voltammogram of Au(111) and polycrystalline gold in H_2SO_4 is shown in Figure 8.2. In this potential region the butterfly peaks from the phase transition of adsorbed H_2SO_4 should be seen as very sharp peaks, e.g. [203].

Instead of the expected sharp peaks only broad ones are seen, also the polycrystalline sample shows a similar CV to nominally single crystalline gold, which is probably due to problems with the microscopic structure of the gold bead crystal [81]. When no potential is applied, Au(111) consists of a reconstructed surface. The peak around 0.4 V vs Ag/AgCl refers to the lifting of the (1×23) reconstruction of the (111) surface to the unreconstructed (1×1) phase [204]. This arrangement has an interatomic spacing of 0.29 nm [50]. The so-called butterfly peaks arise from a superstructure in the anion adsorbate layer which in this case can be sulfate or bisulfate on Au(111) surface when the potential is more positive [205–207]. However, the relatively weak

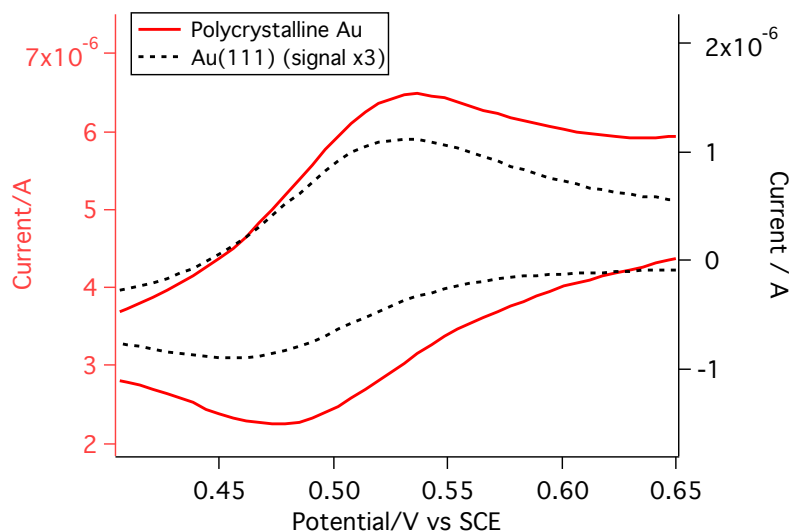


Figure 8.2: Cyclic voltammogram of a Au(111) bead crystal and polycrystalline gold foil in the region of the sulfuric acid phase transition.

current means there are defects in the Au(111) structure.

Figure 8.3 shows the reduction-oxidation CVs of annealed and non-annealed polycrystalline gold. According to the CV, the gold reduction of the annealed polycrystalline gold is shifted to a positive potential from 0.82 V to 0.85 V vs SCE as well as a narrowing of the reduction peak. On the oxidation scan between 1.0 to 1.4 V vs SCE, the non-annealed sample shows a broad peak which peaks at 1.2 V vs SCE. Inversely, the annealed polycrystalline gold shows distinct peaks around 1.03 V and 1.25 V vs SCE. These two peaks are characteristic of Au(111) oxidation and show that annealing can create ordered facets [50]. The oxidation region has a shape that is characteristic of the microstructure of the gold surface [208].

Figure 8.4 compares the active area of smooth and rough gold foils by comparing the CV. Apart from a small bump around 1.1 V vs SCE, the CVs of smooth and rough gold foils have very similar features. The area of the gold reduction peak at 0.85 V vs SCE was measured to be 1293 and 650 μC , respectively. It is quite unexpected that after roughening, the active area of gold decreased. However, this result could be explained as the roughening procedure is the process of electrochemically dissolving Au(0) into the electrolyte solution by applying a negative

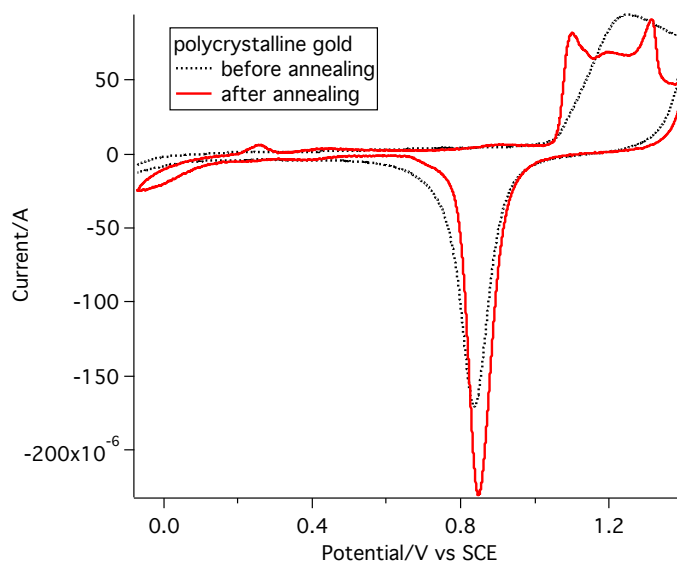


Figure 8.3: Cyclic voltammogram of the reduction-oxidation region of gold foil before and after annealing.

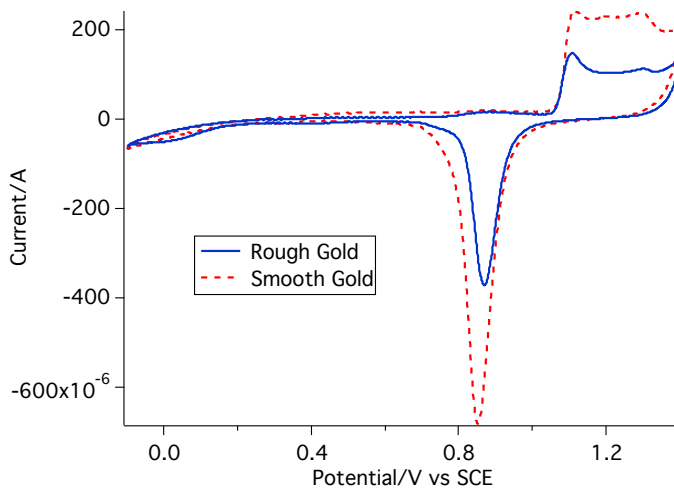


Figure 8.4: Cyclic voltammogram of gold oxidation-reduction comparing between smooth gold foil and rough gold foil.

potential and then redepositing gold oxide when the positive potential is applied [68]. The gold oxide redeposition might decrease the active area of the gold surface. However, this preparation procedure worked perfectly for generating high Raman signals. Figure 8.5 shows the surface morphology of Au(111) surface (A) and roughened polycrystalline gold (B) taken by atomic force microscopy (AFM).

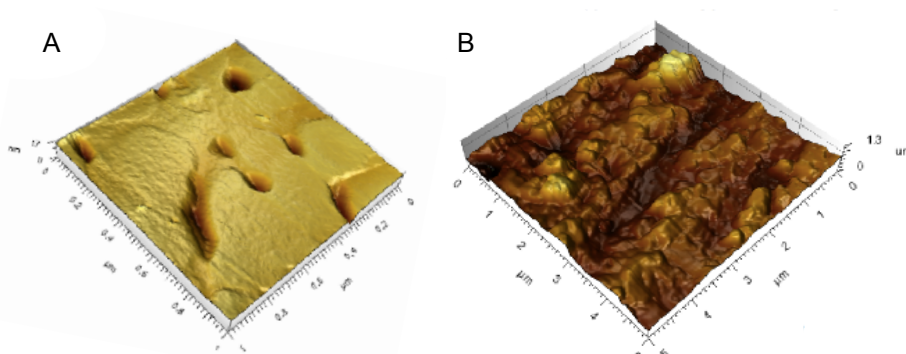


Figure 8.5: AFM of (A) Au(111) (1 micron x 1 micron) and (B) roughening gold polycrystalline (5 microns x 5 microns).

In this study, electrochemical desorption by reduction in alkali solution was used to determine pyS surface coverage on gold. Figure 8.6 shows reductive desorption from smooth and rough gold surfaces. The desorption of pyS from smooth gold surface gives a huge peak at -0.6 V vs SCE in stark contrast to that from the rough surface. The much lower coverage of pyS can also be seen by the earlier onset of hydrogen evolution on the rough compared to smooth surface. This result could be explained by a difference in gold active surface area, which could be due to contamination from the 4-mercaptopyridine substance used.

8.3 Sulfur contamination upon pyS adsorption

A serious problem of pyS adsorption on gold is the contamination by sulfur which forms an Au-S bond and blocks adsorption sites for thiols. There are two sources for the contamination.

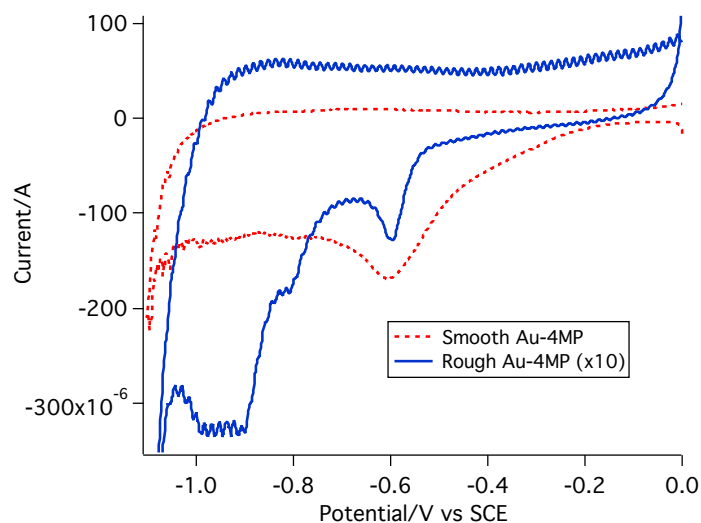


Figure 8.6: Cyclic voltammogram of pyS desorption from smooth gold encase electrode and rough gold foil.

As mentioned by Ramirez *et al.*, a long adsorption time of pyS in ethanol can lead to pyS dissociation, leaving only S atom on gold surface [77]. In addition, many publications mention sulfur contamination in commercial pyS [77, 80]. Among these, Taniguchi *et al.* adsorbed pyS on Au(111) and characterised via cyclic voltammetry [80]. They state that when pyS is adsorbed for more than 5 min, the desorption peak of Au-S, which indicates sulfur contamination, appears. Moreover, they also published ways to diminish this sulfur contamination by adsorbing in KOH solution, using a very low pyS concentration (eg. 5 μM), and adsorbing at positive potentials (+0.3 V vs Ag/AgCl). Figure 8.7 shows the normal pyS desorption from an encased polycrystalline gold electrode in our experiment. The reference condition for sulfur contamination is produced by immersing in Na_2S solution. Na_2S dissolves in the water as Na^+ and S_2^- and forms Au-S bonds. According to literature, the pyS desorption peak is located at -0.574 V vs SCE and sulfur contamination is at -0.894 V vs SCE [80]. The CV of pyS desorption in Figure 8.7 shows two small bumps at both potentials of pyS adsorption and sulfur contamination, which confirms sulfur contamination in our experiment.

Therefore, three suggested procedures have been used to reduce sulfur contamination and observe the change in CV. All of them provided similar results, thus the adsorption in KOH

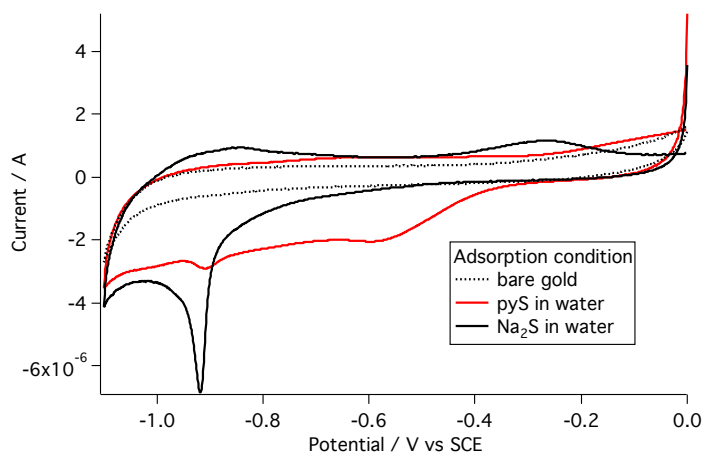


Figure 8.7: Cyclic voltammogram of encased gold electrode soaked in Na_2S .

was selected for further investigation because it is the most convenient method. The adsorption in EtOH has been studied due to its known effect of creating sulfur contamination on gold [77]. Figure 8.8 (A) shows the comparison CV when pyS is adsorbed in 0.1 KOH or EtOH solution (note that the concentration of pyS was very low to minimise sulfur contamination). At the beginning period of the adsorption, no sulfur contamination peak is seen after either 1 and 3 min in KOH solution; however, even 1 min of adsorption in EtOH already produced a contamination. This peak is more pronounced when the adsorption period was increased to 3 min. Therefore, the sulfur contamination is much larger when pyS is adsorbed in EtOH than in KOH solution. Even for the 10 min adsorption time in KOH, the contamination peak still has not developed. The adsorption has also been investigated in water with a longer period of 20 min, Figure 8.8 (B). For the longer adsorption time, the sulfur contamination peak could be found in the adsorption in water, which shows both sulfur contamination and pyS desorption peak. The result also confirmed that by using KOH as an adsorption solvent, the size of the contamination peak can be reduced. For the red-dashed line 5 μM of Na_2S was mixed with the pyS solution. It shows a distinct large peak of sulfur contamination compared to others. The interesting thing is that although the desorption of pyS in water or KOH appears only in the form of tiny peaks at about -0.5 V vs SCE, these show a shift of the background CV during a wide potential scan, compared to the bare gold CV.

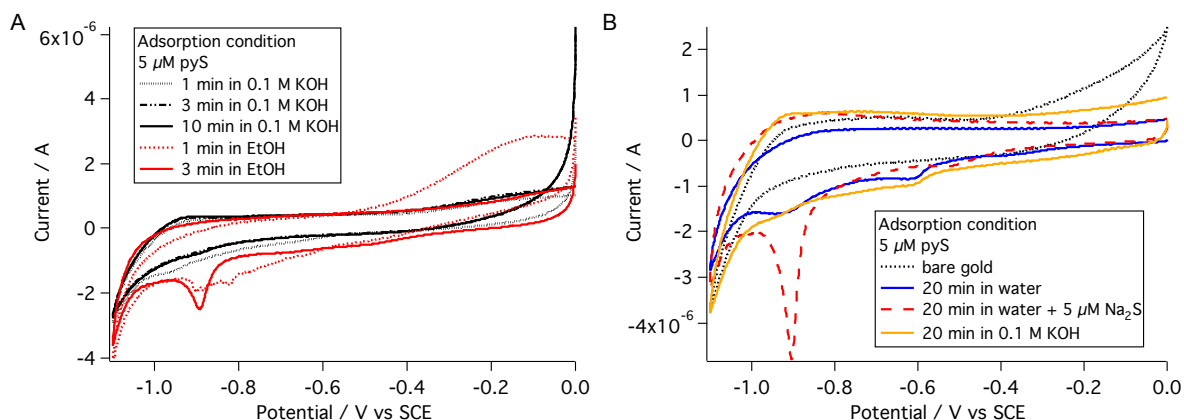


Figure 8.8: Cyclic voltammogram shows pyS desorption from encase gold electrode for various adsorption conditions.

This character can be explained by the effect of different gold facets. According to Yoshimoto *et al.*, the desorption peak from different gold facets appears at different potentials [209]. Moreover, the sulfur contamination peak is located very close to the pyS desorption peak on Au(110). However, in very low sulfur contaminated commercial pyS, the adsorption kinetics of pyS is faster than for a small amount of sulfur in the solution [209]. Another procedure to define the coverage of pyS is the oxidative technique shown earlier [210, 211]. They used oxidation-reduction CVs of gold to determine the coverage. They mentioned that after pyS adsorbed on gold and was oxidatively desorbed, the oxidative peak shifted to higher potential and the reduction peak of gold increased when pyS desorbed from the surface [210]. Another paper carried out CV of sulfur desorption on polycrystalline gold [211]. They found that the oxidation of Au-S appeared at lower potential than Au, on the other hand, the oxidation peak of pyS appeared at higher potential than that of bare gold. Figure 8.9 shows oxidation-reduction CV of gold when adsorbed with pyS in different solvents. All CVs of pyS adsorption on gold exhibit a similar CV pattern. Here, the sulfur contamination can be obvious distinguished since the oxidation peak is at a lower potential than the pyS oxidation peak.

With this method, the coverage of pyS was determined to be 29, 25, and 60 $\mu\text{C}/\text{cm}^2$ for water, H_2SO_4 , and KOH respectively.

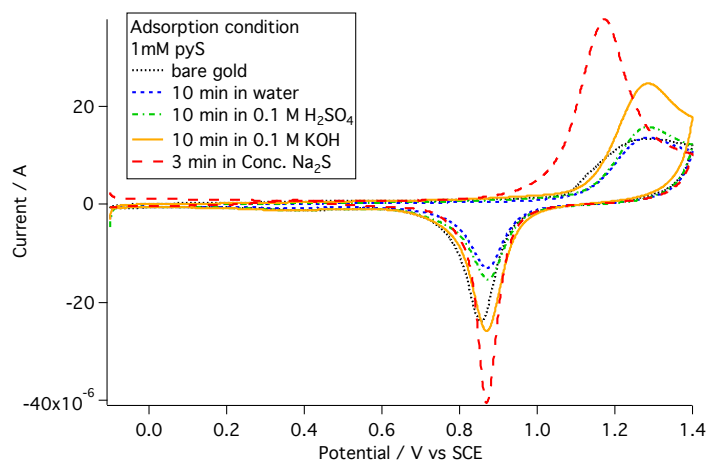


Figure 8.9: Cyclic voltammogram of gold oxidation-reduction of encased gold electrode with different adsorption conditions.

8.4 SHINs

Shell-isolated gold nanoparticles (SHINs) have been synthesized in order to help gain a SERS signal from flat electrodes. SHINs were introduced because they enhance the local electric field by plasmon resonance while remaining electrochemically inert through their silica shell [74, 75, 169, 170]. Figure 8.10 shows a sketch of the core-shell structure of SHINs and the corresponding absorbance spectrum.

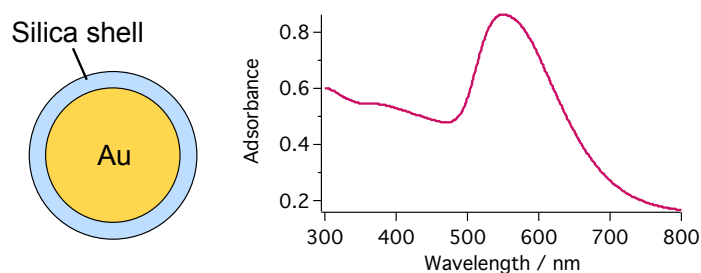


Figure 8.10: The core-shell structure of SHINs and their absorbance spectrum.

In order to enhance the surface plasmon resonance, the size of the gold nanoparticles play a crucial role to maximize the enhancement. According to literature [74, 75, 169, 170], the

most suitable size for 785 nm laser is a diameter of around 55 nm. The size of gold nanoparticle can be determined roughly by measuring the absorption wavelength of the particle with UV-vis spectrometry. 55 nm diameter particles absorb light at around 550 nm. Figure 8.10 shows the absorption spectrum of synthesized gold nanoparticles, which confirms that the majority of particles are 55 nm diameter in size.

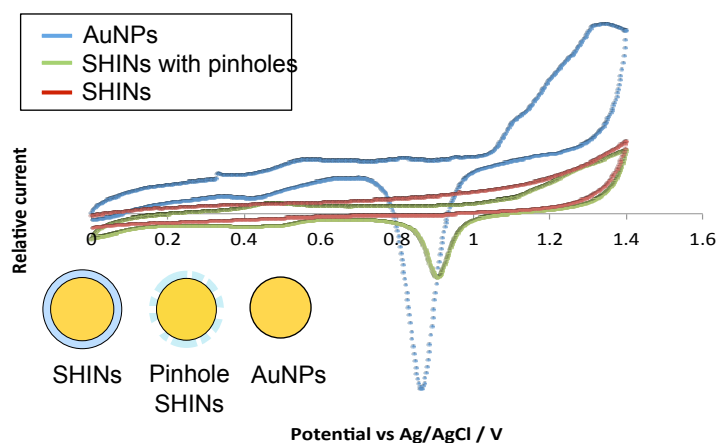


Figure 8.11: Cyclic voltammogram of AuNPs, pinhole-SHINs, and pinhole-free SHINs.

After suitable gold nanoparticles were successfully synthesized, the next step is to coat the gold nanoparticles with a silica shell. This shell should cover the particle homogeneously without any pinholes on the shell. The optimized thickness of shell should be around 4 nm [74]. If the shell is too thick, the enhancement is reduced, if it is too thin, pinholes are seen. In order to determine the appropriate shell thickness, electrochemistry and Raman spectroscopy were used. Figure 8.11 shows cyclic voltammograms of SHINs on a glassy carbon electrode. By running the potential scan of gold oxidation-reduction in H_2SO_4 solution, the pinholes can be revealed. Figure 8.11 shows typical CVs for bare gold nanoparticles and SHINs with and without pinholes. Raman spectroscopy can also be used to observe pinholes [76, 170]. In this technique, a silicon wafer was used as a substrate layer and SHINs were dried on top. A drop of pyS solution was added and a spectrum was recorded. If the SHINs have pinholes, the pyS signal appears as demonstrated by bare gold nanoparticles. pyS cannot adsorb on the wafer, whose surface oxide is chemically identical to the SHIN silica shell. Figure 8.12 (A) shows pinhole-free SHINs and gold nanoparticles adsorbed on silicon wafer. The pinhole-free spectrum does not show any pyS related peaks. Another test was carried out on a gold substrate to test whether the shell was thin enough to enhance the SERS signal. By making gold-pyS-SHINs layer, the pyS should be enhanced significantly. Bare gold nanoparticles were used as a reference to see the enhancement

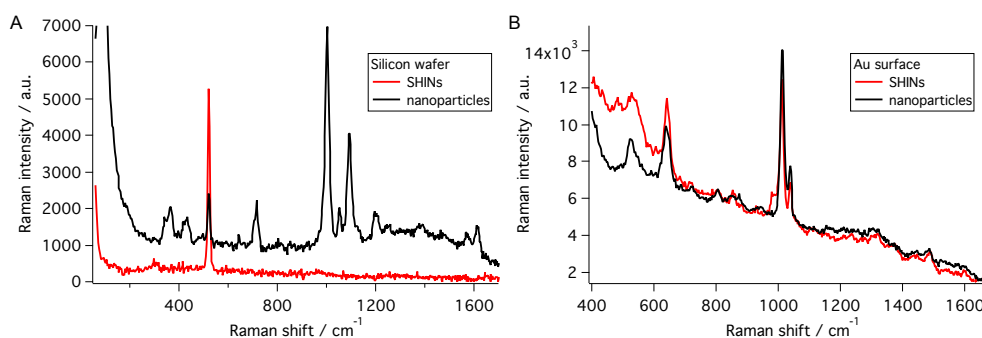


Figure 8.12: SER spectra determining pinholes on SHINs.

of signal. As shown in Figure 8.12 (B), both SHINs and gold nanoparticles enhance SERS signal at a comparable level, which indicates that the shell is thin enough for this purpose. Although SHINs

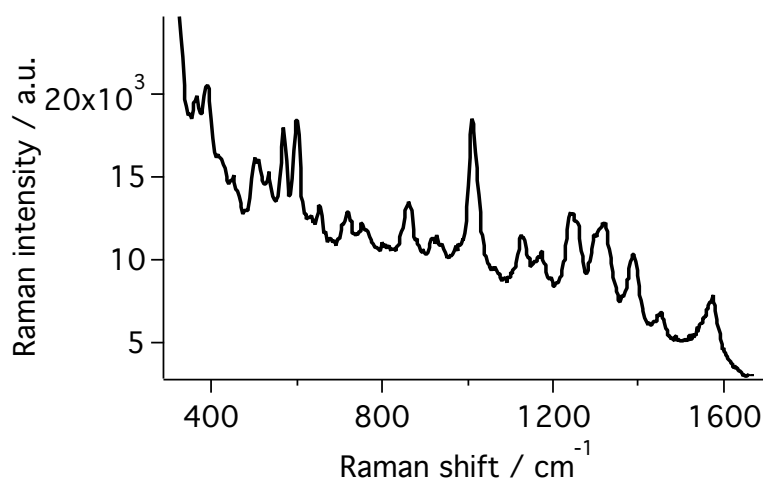


Figure 8.13: SER spectra of contaminated SHINs.

were successfully fabricated, there are many relevant problems. Firstly, pinhole-free particles are difficult to reproduce. The properties of SHINs varied greatly from batch to batch, since the shell thickness is hard to control since it depends on coating period, pH of the reaction, concentration of chemicals, etc. Secondly, the chemical synthesis process leads to contamination. Even if all glassware is carefully cleaned with piranha solution prior to use and the reaction was handled with great care, the contamination still occurred as shown in Figure 8.13. Not only are contaminations hard to avoid, but they are also hard to get rid of. The cleaning method for SHINs can destroy the coating layer or lead to aggregation of nanoparticles eg. piranha solution or electrochemical

cleaning. Lastly, using SHINs requires a mechanical polish of the substrate after use which can destroy the substrate over a long-term period. For all these reasons and the comparative ease of gold roughening, I did not use SHINs in further experiments.

Bibliography

- [1] Scheer, E. *Molecular Electronics: An Introduction to Theory and Experiment*, EBSCO ebook academic collection; World Scientific Publishing Company Pte Limited, 2010.
- [2] Aviram, A.; Ratner, M. A. *Chemical Physics Letters* **1974**, *29*(2), 277 – 283.
- [3] Reed, M. A.; Zhou, C.; Muller, C. J.; Burgin, T. P.; Tour, J. M. *Science* **1997**, *278*(5336), 252–254.
- [4] Tour, J. *Molecular Electronics: Commercial Insights, Chemistry, Devices, Architecture and Programming*, EBSCO ebook academic collection; World Scientific, 2003.
- [5] Quek, S. Y.; Kamenetska, M.; Steigerwald, M. L.; Choi, H. J.; Louie, S. G.; Hybertsen, M. S.; Neaton, J. B.; Venkataraman, L. *Nat Nanotechnol* **2009**, *4*(4), 230–234.
- [6] Petty, M. *Molecular Electronics: From Principles to Practice*, Wiley Series in Materials for Electronic & Optoelectronic Applications; Wiley, 2007.
- [7] Dasari, R.; Ibaez, F. J.; Zamborini, F. P. *Langmuir* **2011**, *27*(11), 7285–7293.
- [8] McCartney, S. *ENIAC: The Triumphs and Tragedies of the World's First Computer*, Science Matters; Berkley Books, 2001.
- [9] Lieber, C. M. *Sci. Am.* **2001**, *285*(3), 58–64.
- [10] Alivisatos, A. P. *Sci. Am.* **2001**, *285*(3), 66–73.
- [11] Gross, M. *Travels to the Nanoworld*; Basic Books, 2008.
- [12] Rietman, E. *Molecular Engineering of Nanosystems*, Biological and Medical Physics, Biomedical Engineering; Springer New York, 2013.
- [13] Khoo, K. H.; Chen, Y.; Li, S.; Quek, S. Y. *Phys. Chem. Chem. Phys.* **2015**, *17*, 77–96.
- [14] McConnell, H. M. *The Journal of Chemical Physics* **1961**, *35*(2), 508–515.
- [15] Zimbovskaya, N. A.; Kuklja, M. M. *The Journal of Chemical Physics* **2009**, *131*(11), 114703.
- [16] Zimbovskaya, N. A. *ArXiv e-prints*, **2013** <http://adsabs.harvard.edu/abs/2013arXiv1301.5569Z> .

- [17] Martín, S.; Grace, I.; Bryce, M. R.; Wang, C.; Jitchati, R.; Batsanov, A. S.; Higgins, S. J.; Lambert, C. J.; Nichols, R. J. *Journal of the American Chemical Society* **2010**, *132*(26), 9157–9164.
- [18] Milan, D. C.; Al-Owaedi, O. A.; Oerthel, M.-C.; Marques-Gonzalez, S.; Brooke, R. J.; Bryce, M. R.; Cea, P.; Ferrer, J.; Higgins, S. J.; Lambert, C. J.; Low, P. J.; Manrique, D. Z.; Martin, S.; Nichols, R. J.; Schwarzacher, W.; Garcia-Suarez, V. M. *The Journal of Physical Chemistry C* **2016**, *120*(29), 15666–15674.
- [19] Vezzoli, A.; Grace, I.; Brooke, C.; Wang, K.; Lambert, C. J.; Xu, B.; Nichols, R. J.; Higgins, S. J. *Nanoscale* **2015**, *7*, 18949–18955.
- [20] Sedghi, G.; Garcia-Suarez, V. M.; Esdaile, L. J.; Anderson, H. L.; Lambert, C. J.; Martin, S.; Bethell, D.; Higgins, S. J.; Elliott, M.; Bennett, N.; Macdonald, J. E.; Nichols, R. J. *Nat Nanotechnol* **2011**, *6*(8), 517–523.
- [21] Haiss, W.; Nichols, R. J.; van Zalinge, H.; Higgins, S. J.; Bethell, D.; Schiffrin, D. J. *Phys. Chem. Chem. Phys.* **2004**, *6*, 4330–4337.
- [22] Haiss, W.; Albrecht, T.; van Zalinge, H.; Higgins, S. J.; Bethell, D.; Höbenreich, H.; Schiffrin, D. J.; Nichols, R. J.; Kuznetsov, A. M.; Zhang, J.; Chi, Q.; Ulstrup, J. *The Journal of Physical Chemistry B* **2007**, *111*(24), 6703–6712.
- [23] Leary, E.; Höbenreich, H.; Higgins, S. J.; van Zalinge, H.; Haiss, W.; Nichols, R. J.; Finch, C. M.; Grace, I.; Lambert, C. J.; McGrath, R.; Smerdon, J. *Chem. Commun.* **2009**, *102*, 086801.
- [24] Stadler, J.; Schmid, T.; Opilik, L.; Kuhn, P.; Dittrich, P. S.; Zenobi, R. *Beilstein J Nanotechnol* **2011**, *2*, 509–15.
- [25] Kim, K.; Shin, D.; Kim, K. L.; Shin, K. S. *Physical Chemistry Chemical Physics* **2012**, *14*(12), 4095–4100.
- [26] Zhou, X.-S.; Liu, L.; Fortgang, P.; Lefevre, A.-S.; Serra-Muns, A.; Raouafi, N.; Amatore, C.; Mao, B.-W.; Maisonhaute, E.; Schöllhorn, B. *Journal of the American Chemical Society* **2011**, *133*(19), 7509–7516.
- [27] Amatore, C.; Maisonhaute, E. *Analytical Chemistry* **2005**, *77*(15), 303 A–311 A.
- [28] Arnolds, H.; Bonn, M. *Surface Science Reports* **2010**, *65*(2), 45 – 66.
- [29] Kolasinski, K. *Surface science*; John Wiley & Sons, Ltd: Malaysia, third ed., 2013.
- [30] Hakkinen, H. *Chem. Soc. Rev.* **2008**, *37*, 1847–1859.
- [31] Nankawa, T.; Suzuki, Y.; Ozaki, T.; Francis, A. J.; Ohnuki, T. *Journal of Nuclear Science and Technology* **2008**, *45*(3), 251–256.
- [32] Wan, L.-J.; Noda, H.; Hara, Y.; Osawa, M. *Journal of Electroanalytical Chemistry* **2000**, *489*(1-2), 68–75.
- [33] Eberle, F.; Kayser, M.; Kolb, D. M.; Saitner, M.; Boyen, H.-G.; Dörlieslaeger, M.; Mayer, D.; Wirth, A. *Langmuir* **2010**, *26*(7), 4738–4742.

- [34] Nuzzo, R. G.; Allara, D. L. *Journal of the American Chemical Society* **1983**, *105*(13), 4481–4483.
- [35] Love, J. C.; Estroff, L. A.; Kriebel, J. K.; Nuzzo, R. G.; Whitesides, G. M. *Chemical Reviews* **2005**, *105*(4), 1103–1170.
- [36] Finklea, H. O.; Robinson, L. R.; Blackburn, A.; Richter, B.; Allara, D.; Bright, T. *Langmuir* **1986**, *2*(2), 239–244.
- [37] Dubois, L. H.; Nuzzo, R. G. *Annual Review of Physical Chemistry* **1992**, *43*(1), 437–463.
- [38] Bain, C. D.; Whitesides, G. M. *Angewandte Chemie International Edition in English* **1989**, *28*(4), 506–512.
- [39] Bain, C. D.; Whitesides, G. M. *Journal of the American Chemical Society* **1989**, *111*(18), 7164–7175.
- [40] Porter, M. D.; Bright, T. B.; Allara, D. L.; Chidsey, C. E. D. *Journal of the American Chemical Society* **1987**, *109*(12), 3559–3568.
- [41] Rajalingam, K. Reactions at an organic surface Master's thesis, Ruhr-Universität Bochum, **2008**.
- [42] Manolova, M.; Ivanova, V.; Kolb, D. M.; Boyen, H. G.; Ziemann, P.; Büttner, M.; Romanyuk, A.; Oelhafen, P. *Surface Science* **2005**, *590*(23), 146–153.
- [43] Manolova, M.; Kayser, M.; Kolb, D. M.; Boyen, H. G.; Ziemann, P.; Mayer, D.; Wirth, A. *Electrochimica Acta* **2007**, *52*(8), 2740–2745.
- [44] Kucera, J.; Groß, A. *Physical Chemistry Chemical Physics* **2010**, *12*(17), 4423–4430.
- [45] Saitner, M.; Eberle, F.; Baccus, J.; Döller, M.; Wagner, P.; Kolb, D. M.; Boyen, H.-G. *The Journal of Physical Chemistry C* **2012**, *116*(41), 21810–21815.
- [46] Poppenberg, J.; Richter, S.; Darlatt, E.; Traulsen, C. H. H.; Min, H.; Unger, W. E. S.; Schalley, C. A. *Surface Science* **2012**, *606*(34), 367–377.
- [47] Ivanova, V.; Baunach, T.; Kolb, D. M. *Electrochimica Acta* **2005**, *50*(21), 4283–4288.
- [48] Kucera, J.; Groß, A. *Physical Chemistry Chemical Physics* **2012**, *14*(7), 2353–2361.
- [49] Linear Sweep and Cyclic Voltammetry: The Principles. Teaching Notes, University of Cambridge, Electrochemical and Micro Engineering group <http://www.ceb.cam.ac.uk/research/groups/rg-eme/teaching-notes/linear-sweep-and-cyclic-voltammetry-the-principles>.
- [50] Yoshimoto, S.; Kim, Y.-G.; Sato, K.; Inukai, J.; Itaya, K. *Phys. Chem. Chem. Phys.* **2012**, *14*, 2286–2291.
- [51] Burke, L. D.; Nugent, P. F. *Gold Bulletin* **1997**, *30*(2), 43–53.
- [52] Krishnan, R. S.; Shankar, R. K. *Journal of Raman Spectroscopy* **1981**, *10*(1), 1–8.
- [53] Raman, C.; Shankar, R. *Nature* **1921**, *121*, 501–502.
- [54] Aroca, R. *Surface-Enhanced Vibrational Spectroscopy*; Wiley, 2006.

- [55] Fleischmann, M.; Hendra, P. J.; McQuillan, A. J. *Chemical Physics Letters* **1974**, *26*(2), 163–166.
- [56] Nie, S.; Emory, S. R. *Science* **1997**, *275*(5303), 1102.
- [57] Kneipp, K.; Wang, Y.; Kneipp, H.; Perelman, L. T.; Itzkan, I.; Dasari, R. R.; Feld, M. S. *Physical Review Letters* **1997**, *78*(9), 1667–1670.
- [58] Le Ru, E.; Etchegoin, P. *Principles of Surface-Enhanced Raman Spectroscopy and related plasmonic effects*; Elsevier, first ed., 2009.
- [59] Kelly, K. L.; Coronado, E.; Zhao, L. L.; Schatz, G. C. *The Journal of Physical Chemistry B* **2003**, *107*(3), 668–677.
- [60] Creighton, J. A. *Surface Science* **1983**, *124*(1), 209–219.
- [61] Lombardi, J. R.; Birke, R. L. *Accounts of Chemical Research* **2009**, *42*(6), 734–742.
- [62] Arnolds, H. *Progress in Surface Science* **2011**, *86*(12), 1 – 40.
- [63] Teodorescu, C. M. *Physical Chemistry Chemical Physics* **2015**, *17*(33), 21302–21314.
- [64] Zayak, A. T.; Hu, Y. S.; Choo, H.; Bokor, J.; Cabrini, S.; Schuck, P. J.; Neaton, J. B. *Phys Rev Lett* **2011**, *106*(8), 083003.
- [65] Shen, Y. R. *The Journal of Physical Chemistry C* **2012**, *116*(29), 15505–15509.
- [66] Stiopkin, I. V.; Jayathilake, H. D.; Bordenyuk, A. N.; Benderskii, A. V. *Journal of the American Chemical Society* **2008**, *130*(7), 2271–2275.
- [67] Raschke, M.; Shen, Y. *Encyclopedia of Modern Optics* **2005**, 184–189.
- [68] Liu, Y.-C.; Wang, C.-C.; Tsai, C.-E. *Electrochemistry Communications* **2005**, *7*(12), 1345–1350.
- [69] Mahajan, S.; Cole, R. M.; Speed, J. D.; Pelfrey, S. H.; Russell, A. E.; Bartlett, P. N.; Barnett, S. M.; Baumberg, J. J. *The Journal of Physical Chemistry C* **2010**, *114*(16), 7242–7250.
- [70] Gao, P.; Weaver, M. J. *The Journal of Physical Chemistry* **1986**, *90*(17), 4057–4063.
- [71] Tian, Z.-Q.; Ren, B.; Wu, D.-Y. *The Journal of Physical Chemistry B* **2002**, *106*(37), 9463–9483.
- [72] Li, X.; Gewirth, A. A. *Journal of the American Chemical Society* **2003**, *125*(23), 7086–7099.
- [73] Yang, D. F.; Wilde, C. P.; Morin, M. *Langmuir* **1996**, *12*(26), 6570–6577.
- [74] Li, J. F.; Huang, Y. F.; Ding, Y.; Yang, Z. L.; Li, S. B.; Zhou, X. S.; Fan, F. R.; Zhang, W.; Zhou, Z. Y.; Wu, D. Y.; Ren, B.; Wang, Z. L.; Tian, Z. Q. *Nature* **2010**, *464*(7287), 392–395.
- [75] Lu, Y.; Yin, Y.; Li, Z.-Y.; Xia, Y. *Nano Letters* **2002**, *2*(7), 785–788.
- [76] Li, J. F.; Tian, X. D.; Li, S. B.; Anema, J. R.; Yang, Z. L.; Ding, Y.; Wu, Y. F.; Zeng, Y. M.; Chen, Q. Z.; Ren, B.; Wang, Z. L.; Tian, Z. Q. *Nat Protoc* **2013**, *8*(1), 52–65.

- [77] Ramirez, E. A.; Cortes, E.; Rubert, A. A.; Carro, P.; Benitez, G.; Vela, M. E.; Salvarezza, R. C. *Langmuir* **2012**, *28*(17), 6839–47.
- [78] Manolova, M.; Boyen, H.-G.; Kucera, J.; Groß, A.; Romanyuk, A.; Oelhafen, P.; Ivanova, V.; Kolb, D. M. *Advanced Materials* **2009**, *21*(3), 320–324.
- [79] Guerrini, L.; Rodriguez-Loureiro, I.; Correa-Duarte, M. A.; Lee, Y. H.; Ling, X. Y.; Garcia de Abajo, F. J.; Alvarez-Puebla, R. A. *Nanoscale* **2014**, *6*(14), 8368–75.
- [80] Taniguchi, I.; Yoshimoto, S.; Yoshida, M.; Kobayashi, S.-i.; Miyawaki, T.; Aono, Y.; Sunatsuki, Y.; Taira, H. *Electrochimica Acta* **2000**, *45*(18), 2843–2853.
- [81] Ozoemena, K. I.; Nyokong, T. *Electrochimica Acta* **2006**, *51*(13), 2669–2677.
- [82] Diogenes, I. C. N.; Nart, F. C.; Moreira, I. S. *Inorganic Chemistry* **1999**, *38*(8), 1646–1647.
- [83] Eberle, F.; Saitner, M.; Boyen, H.-G.; Kucera, J.; Groß, A.; Romanyuk, A.; Oelhafen, P.; DOLieslaeger, M.; Manolova, M.; Kolb, D. *Angewandte Chemie International Edition* **2010**, *49*(2), 341–345.
- [84] Muglali, M. I.; Liu, J.; Bashir, A.; Borissov, D.; Xu, M.; Wang, Y.; Wöll, C.; Rohwerder, M. *Physical Chemistry Chemical Physics* **2012**, *14*(14), 4703–4712.
- [85] Langerock, S.; Mnard, H.; Rowntree, P.; Heerman, L. *Langmuir* **2005**, *21*(11), 5124–5133.
- [86] Jensen, R.; Sherin, J.; Emory, R. S. *Applied Spectroscopy* **2007**, *61*(8), 832–838.
- [87] Birke, R. L.; Lombardi, J. R. *Journal of Optics* **2015**, *17*(11), 114004.
- [88] Wan, L.-J.; Hara, Y.; Noda, H.; Osawa, M. *The Journal of Physical Chemistry B* **1998**, *102*(31), 5943–5946.
- [89] Kucera, J.; Groß, A. *Langmuir* **2008**, *24*(24), 13985–13992.
- [90] Koslowski, B.; Tschetschetkin, A.; Maurer, N.; Ziemann, P.; Kucera, J.; Groß, A. *The Journal of Physical Chemistry C* **2013**, *117*(39), 20060–20067.
- [91] Zhou, W.; Baunach, T.; Ivanova, V.; Kolb, D. *Langmuir* **2004**, *20*(11), 4590–4595.
- [92] Lamp, B. D.; Hobara, D.; Porter, M. D.; Niki, K.; Cotton, T. M. *Langmuir* **1997**, *13*(4), 736–741.
- [93] Yoshimoto, S.; Sawaguchi, T.; Mizutani, F.; Taniguchi, I. *Electrochemistry Communications* **2000**, *2*(1), 39–43.
- [94] Jin, Q.; Rodriguez, J. A.; Li, C. Z.; Darici, Y.; Tao, N. J. *Surface Science* **1999**, *425*(1), 101–111.
- [95] Baunach, T.; Ivanova, V.; Scherson, D. A.; Kolb, D. M. *Langmuir* **2004**, *20*(7), 2797–2802.
- [96] Widrig, C. A.; Chung, C.; Porter, M. D. *Journal of Electroanalytical Chemistry and Interfacial Electrochemistry* **1991**, *310*(1), 335 – 359.
- [97] Sawaguchi, T.; Mizutani, F.; Taniguchi, I. *Langmuir* **1998**, *14*(13), 3565–3569.

- [98] Carron, K. T.; Hurley, L. G. *the Journal of Physical Chemistry* **1991**, *95*(24), 9979–9984.
- [99] Zhang, L.; Bai, Y.; Shang, Z.; Zhang, Y.; Mo, Y. *Journal of Raman Spectroscopy* **2007**, *38*(9), 1106–1111.
- [100] Baldwin, J. A.; Vlkov, B.; Andrews, M. P.; Butler, I. S. *Langmuir* **1997**, *13*(14), 3744–3751.
- [101] Jung, H. S.; Kim, K.; Kim, M. S. *Journal of Molecular Structure* **1997**, *407*(2), 139–147.
- [102] Do, W. H.; Lee, C. J.; Kim, D. Y.; Jung, M. J. *Journal of Industrial and Engineering Chemistry* **2012**, *18*(6), 2141–2146.
- [103] Hassan, N.; Holze, R. *Journal of Chemical Sciences* **2009**, *121*(5), 693–701.
- [104] Guo, H.; Ding, L.; Mo, Y. *Journal of Molecular Structure* **2011**, *991*(1-3), 103–107.
- [105] Wang, Z.; Rothberg, L. J. *The Journal of Physical Chemistry B* **2005**, *109*(8), 3387–3391.
- [106] Yu, HZ.; Xia, N.; Liu, Z. *Anal Chem* **1999**, *71*(7), 1354–1358.
- [107] Bron, M.; Holze, R. *Journal of Solid State Electrochemistry* **2015**, *19*(9), 2673–2682.
- [108] Liu, J.; Stratmann, L.; Krakert, S.; Kind, M.; Olbrich, F.; Terfort, A.; Wöll, C. *Journal of Electron Spectroscopy and Related Phenomena* **2009**, *172*(1-3), 120–127.
- [109] Pradhan, M.; Chowdhury, J.; Sarkar, S.; Sinha, A. K.; Pal, T. *The Journal of Physical Chemistry C* **2012**, *116*(45), 24301–24313.
- [110] Corio, P.; Andrade, G. F. S.; Digenes, I. C. N.; Moreira, I. S.; Nart, F. C.; Temperini, M. L. A. *Journal of Electroanalytical Chemistry* **2002**, *520*(1-2), 40–46.
- [111] Sueoka, T.; Inukai, J.; Ito, M. *Journal of Electron Spectroscopy and Related Phenomena* **1993**, *64/65*, 363–370.
- [112] Hu, J.; Zhao, B.; Xu, W.; Li, B.; Fan, Y. *Spectrochimica Acta Part A: Molecular and Biomolecular Spectroscopy* **2002**, *58*(13), 2827–2834.
- [113] Gardner, A. M.; Wright, T. G. *J Chem Phys* **2011**, *135*(11), 114305.
- [114] Wilson, E. B. *May* **1934**, *45*, 706–714.
- [115] Sellers, H.; Ulman, A.; Shnidman, Y.; Eilers, J. E. *Journal of the American Chemical Society* **1993**, *115*(21), 9389–9401.
- [116] Diaz-Morales, O.; Calle-Vallejo, F.; de Munck, C.; Koper, M. T. M. *Chemical Science* **2013**, *4*(6), 2334.
- [117] Zhumaev, U.; Rudnev, A. V.; Li, J.-F.; Kuzume, A.; Vu, T.-H.; Wandlowski, T. *Electrochimica Acta* **2013**, *112*, 853–863.
- [118] Gui, J. Y.; Lu, F.; Stern, D. A.; Hubbard, A. T. *Journal of Electroanalytical Chemistry and Interfacial Electrochemistry* **1990**, *292*(1), 245–262.

- [119] Singh, P.; Deckert, V. *Chem Commun (Camb)* **2014**, 50(76), 11204–7.
- [120] Zheng, X.-S.; Hu, P.; Zhong, J.-H.; Zong, C.; Wang, X.; Liu, B.-J.; Ren, B. *The Journal of Physical Chemistry C* **2014**, 118(7), 3750–3757.
- [121] Xiao-Wei, C.; Wen-Hua, L.; Xin-Ran, L.; Rong, W.; Xia-Qin, W. *Acta Physico-Chimico Sinica* **2011**, 27(7), 1600–1608.
- [122] Bryant, M.; Crooks, R. *Langmuir* **1993**, 9(2), 385–387.
- [123] Albert, A.; Barlin, G. B. *J. Chem. Soc.* **1959**, pages 2384–2396.
- [124] Beak, P.; Fry, F. S.; Lee, J.; Steele, F. *Journal of the American Chemical Society* **1976**, 98(1), 171–179.
- [125] Berg, E. R.; Freeman, S. A.; Green, D. D.; Ulness, D. J. *The Journal of Physical Chemistry A* **2006**, 110(50), 13434–13446.
- [126] de F. Paulo, T.; Abrua, H. D.; Digenes, I. C. N. *Langmuir* **2012**, 28(51), 17825–17831.
- [127] Liu, J.; Schupbach, B.; Bashir, A.; Shekhah, O.; Nefedov, A.; Kind, M.; Terfort, A.; Wöll, C. *Physical Chemistry Chemical Physics* **2010**, 12(17), 4459–4472.
- [128] Bartels, L. *Nat Chem* **2010**, 2(2), 87–95.
- [129] Smith, E. L.; Alves, C. A.; Anderegg, J. W.; Porter, M. D.; Siperko, L. M. *Langmuir* **1992**, 8(11), 2707–2714.
- [130] Jung, D. R.; Czanderna, A. W. *Critical Reviews in Solid State and Materials Sciences* **1994**, 19(1), 1–54.
- [131] Jung, D. R.; Czanderna, A. W.; Herdt, G. C. *Journal of Vacuum Science & Technology A* **1996**, 14(3).
- [132] Herdt, G. C.; Czanderna, A. W. *Journal of Vacuum Science & Technology A* **1999**, 17(6).
- [133] Nishizawa, M.; Sunagawa, T.; Yoneyama, H. *Langmuir* **1997**, 13(20), 5215–5217.
- [134] Hagenström, H.; Schneeweiss, M. A.; Kolb, D. M. *Langmuir* **1999**, 15(22), 7802–7809.
- [135] Hagenström, H.; Schneeweiss, M.; Kolb, D. *Electrochimica Acta* **1999**, 45(7), 1141 – 1145.
- [136] Gilbert, S. E.; Cavalleri, O.; Kern, K. *The Journal of Physical Chemistry* **1996**, 100(30), 12123–12130.
- [137] Zamborini, F. P.; Campbell, J. K.; Crooks, R. M. *Langmuir* **1998**, 14(3), 640–647.
- [138] Oyamatsu, D.; Kuwabata, S.; Yoneyama, H. *Journal of Electroanalytical Chemistry* **1999**, 473(12), 59 – 67.
- [139] Sun, L.; Crooks, R. M. *Journal of The Electrochemical Society* **1991**, 138(8), L23–L25.
- [140] Schneeweiss, M.; Hagenström, H.; Esplandi, M.; Kolb, D. *Applied Physics A* **1999**, 69(5), 537–551.
- [141] Esplandi, M. J.; Hagenström, H.; Kolb, D. M. *Langmuir* **2001**, 17(3), 828–838.

- [142] Baunach, T.; Kolb, D. *Analytical and Bioanalytical Chemistry* **2002**, *373*(8), 743–748.
- [143] Chesneau, F.; Zharnikov, M. *The Journal of Physical Chemistry C* **2014**, *118*(24), 12980–12988.
- [144] Keith, J. A.; Jacob, T. *Chemistry* **2010**, *16*(41), 12381–6.
- [145] Silien, C.; Lahaye, D.; Caffio, M.; Schaub, R.; Champness, N. R.; Buck, M. *Langmuir* **2011**, *27*(6), 2567–2574.
- [146] Muglali, M. I.; Bashir, A.; Birkner, A.; Rohwerder, M. *Journal of Materials Chemistry* **2012**, *22*(29), 14337–14340.
- [147] Baunach, T.; Ivanova, V.; Kolb, D. .; Boyen, H. G.; Ziemann, P.; Büttner, M.; Oelhafen, P. *Advanced Materials* **2004**, *16*(22), 2024–2028.
- [148] Shekhah, O.; Busse, C.; Bashir, A.; Turcu, F.; Yin, X.; Cyganik, P.; Birkner, A.; Schuhmann, W.; Woll, C. *Physical Chemistry Chemical Physics* **2006**, *8*(29), 3375–3378.
- [149] Boyen, H. G.; Ziemann, P.; Wiedwald, U.; Ivanova, V.; Kolb, D. M.; Sakong, S.; Groß, A.; Romanyuk, A.; Büttner, M.; Oelhafen, P. *Nat Mater* **2006**, *5*(5), 394–9.
- [150] Keith, J. A.; Jacob, T. *Electrochimica Acta* **2010**, *55*(27), 8258–8262.
- [151] Kucera, J.; Groß, A. *Beilstein Journal of Nanotechnology* **2011**, *2*, 384–393.
- [152] Adams, B. D.; Chen, A. *Materials Today* **2011**, *14*(6), 282 – 289.
- [153] Tsutsui, M.; Taniguchi, M.; Shoji, K.; Yokota, K.; Kawai, T. *Nanoscale* **2009**, *1*, 164–170.
- [154] Kushmerick, J. G.; Lazorcik, J.; Patterson, C. H.; Shashidhar, R.; Seferos, D. S.; Bazan, G. C. *Nano Letters* **2004**, *4*(4), 639–642.
- [155] Jun, Y.; Zhu, X.-Y. *Journal of the American Chemical Society* **2004**, *126*(41), 13224–13225.
- [156] Scott, A.; Hacker, C. A.; Janes, D. B. *The Journal of Physical Chemistry C* **2008**, *112*(36), 14021–14026.
- [157] Mahmoud, A. M.; Bergren, A. J.; McCreery, R. L. *Analytical Chemistry* **2009**, *81*(16), 6972–6980.
- [158] Nowak, A. M.; McCreery, R. L. *Journal of the American Chemical Society* **2004**, *126*(50), 16621–16631.
- [159] Asanuma, H.; Noguchi, H.; Huang, Y.; Uosaki, K.; Yu, H.-Z. *The Journal of Physical Chemistry C* **2009**, *113*(50), 21139–21146.
- [160] Cui, L.; Liu, B.; Vonlanthen, D.; Mayor, M.; Fu, Y.; Li, J.-F.; Wandlowski, T. *Journal of the American Chemical Society* **2011**, *133*(19), 7332–7335.
- [161] Matsuhita, R.; Horikawa, M.; Naitoh, Y.; Nakamura, H.; Kiguchi, M. *The Journal of Physical Chemistry C* **2013**, *117*(4), 1791–1795.
- [162] Ikeda, K.; Fujimoto, N.; Uosaki, K. *The Journal of Physical Chemistry C* **2014**, *118*(37), 21550–21557.

- [163] Dasari, R.; Zamborini, F. P. *Analytical Chemistry* **2016**, *88*(1), 675–681.
- [164] Li, Y.; Zolotavin, P.; Doak, P.; Kronik, L.; Neaton, J. B.; Natelson, D. *Nano Letters* **2016**, *16*(2), 1104–1109.
- [165] Khlebtsov, B.; Khanadeev, V.; Khlebtsov, N. *Nano Research* **2016**, *9*(8), 2303–2318.
- [166] Marqus-Gonzalez, S.; Matsushita, R.; Kiguchi, M. *Journal of Optics* **2015**, *17*(11), 114001.
- [167] Huang, Y. F.; Yin, N. N.; Wang, X.; Wu, D. Y.; Ren, B.; Tian, Z. Q. *Chemistry* **2010**, *16*(5), 1449–53.
- [168] Baldwin, J.; Schhler, N.; Butler, I. S.; Andrews, M. P. *Langmuir* **1996**, *12*(26), 6389–6398.
- [169] Li, J.-F.; Ding, S.-Y.; Yang, Z.-L.; Bai, M.-L.; Anema, J. R.; Wang, X.; Wang, A.; Wu, D.-Y.; Ren, B.; Hou, S.-M.; Wandlowski, T.; Tian, Z.-Q. *Journal of the American Chemical Society* **2011**, *133*(40), 15922–15925.
- [170] Li, J. F.; Li, S. B.; Anema, J. R.; Yang, Z. L.; Huang, Y. F.; Ding, Y.; Wu, Y. F.; Zhou, X. S.; Wu, D. Y.; Ren, B.; Wang, Z. L.; Tian, Z. Q. *Appl Spectrosc* **2011**, *65*(6), 620–626.
- [171] Gao, J.; Guo, L.; Wu, J.; Feng, J.; Wang, S.; Lai, F.; Xie, J.; Tian, Z. *Journal of Raman Spectroscopy* **2014**, *45*(8), 619–626.
- [172] Kibler, L.; Kleinert, M.; Randler, R.; Kolb, D. *Surface Science* **1999**, *443*(12), 19 – 30.
- [173] Brankovic, S.; McBreen, J.; Adi, R. *Surface Science* **2001**, *479*(13), L363 – L368.
- [174] Tang, J.; Petri, M.; Kibler, L. A.; Kolb, D. M. *Electrochimica Acta* **2005**, *51*(1), 125–132.
- [175] Wu, D.-Y.; Ren, B.; Xu, X.; Liu, G.-K.; Yang, Z.-L.; Tian, Z.-Q. *The Journal of Chemical Physics* **2003**, *119*(3), 1701.
- [176] Shegai, T.; Vaskevich, A.; Rubinstein, I.; Haran, G. *Journal of the American Chemical Society* **2009**, *131*(40), 14390–14398.
- [177] Hammer, B.; Nørskov, J. In *Impact of Surface Science on Catalysis*, Vol. 45 of *Advances in Catalysis*; Academic Press, 2000; pages 71 – 129.
- [178] Lindstrom, C. D.; Zhu, X.-Y. *Chemical Reviews* **2006**, *106*(10), 4281–4300.
- [179] Morton, S. M.; Jensen, L. *Journal of the American Chemical Society* **2009**, *131*(11), 4090–4098.
- [180] Kuznetsov, A. M.; Ulstrup, J. *The Journal of Chemical Physics* **2002**, *116*(5).
- [181] Over, H.; Kim, Y. D.; Seitsonen, A. P.; Wendt, S.; Lundgren, E.; Schmid, M.; Varga, P.; Morgante, A.; Ertl, G. *Science* **2000**, *287*(5457), 1474–1476.
- [182] Reinert, F.; Hüfner, S. *New Journal of Physics* **2005**, *7*(1), 97.
- [183] Ueba, H.; Gumhalter, B. *Progress in Surface Science* **2007**, *82*(46), 193 – 223.

- [184] Brolo, A. G.; Irish, D. E.; Lipkowski, J. *The Journal of Physical Chemistry B* **1997**, *101*(20), 3906–3909.
- [185] Brolo, A. G.; Irish, D. E.; Szymanski, G.; Lipkowski, J. *Langmuir* **1998**, *14*(2), 517–527.
- [186] Stolberg, L.; Lipkowski, J.; Irish, D. *Journal of Electroanalytical Chemistry and Interfacial Electrochemistry* **1991**, *300*(1), 563 – 584.
- [187] Weaver, M. J.; Hupp, J. T.; Barz, F.; Gordon, J. G.; Philpott, M. R. *Journal of Electroanalytical Chemistry and Interfacial Electrochemistry* **1984**, *160*(1), 321 – 333.
- [188] Christensen, P. A.; Hamnett, A.; Blackham, I. *Journal of Electroanalytical Chemistry and Interfacial Electrochemistry* **1991**, *318*(1), 407–410.
- [189] Xie, Y.; Wu, D. Y.; Liu, G. K.; Huang, Z. F.; Ren, B.; Yan, J. W.; Yang, Z. L.; Tian, Z. Q. *Journal of Electroanalytical Chemistry* **2003**, *554-555*, 417–425.
- [190] Chao, Y.; Zhou, Q.; Li, Y.; Yan, Y.; Wu, Y.; Zheng, J. *The Journal of Physical Chemistry C* **2007**, *111*(45), 16990–16995.
- [191] Ingram, J. C.; Pemberton, J. E. *Langmuir* **1992**, *8*(8), 2034–2039.
- [192] Ivarez Puebla, R. A. *The Journal of Physical Chemistry Letters* **2012**, *3*(7), 857–866.
- [193] Fang, Y.; Seong, N.-H.; Dlott, D. D. *Science* **2008**, *321*(5887), 388–392.
- [194] Ikeda, K.; Suzuki, S.; Uosaki, K. *J Am Chem Soc* **2013**, *135*(46), 17387–92.
- [195] Chowdhury, J. *Applied Spectroscopy Reviews* **2015**, *50*(3), 240–260.
- [196] Taniguchi, I.; Iseki, M.; Yamaguchi, H.; Yasukouchi, K. *J. Electroanal Chem* **1985**, *186*, 299–307.
- [197] Bourguignon, B.; Zheng, W.; Carrez, S.; Ouvrard, A.; Fournier, F.; Dubost, H. *Mar* **2009**, *79*, 125433.
- [198] Bordenyuk, A. N.; Weeraman, C.; Yatawara, A.; Jayathilake, H. D.; Stiopkin, I.; Liu, Y.; Benderskii, A. V. *The Journal of Physical Chemistry C* **2007**, *111*(25), 8925–8933.
- [199] Lagutchev, A.; Lozano, A.; Mukherjee, P.; Hambir, S. A.; Dlott, D. D. *Spectrochimica Acta Part A: Molecular and Biomolecular Spectroscopy* **2010**, *75*(4), 1289 – 1296.
- [200] Garcia-Rey, N. *Interaction of a Copper Surface with Light: Plasmons, Electrons & Molecular Vibrations* PhD thesis, University of Liverpool, **2011**.
- [201] Lane, I. M.; Liu, Z.-P.; King, D. A.; Arnolds, H. *The Journal of Physical Chemistry C* **2007**, *111*(38), 14198–14206.
- [202] Birke, R. L.; Lombardi, J. R.; Saidi, W. A.; Norman, P. *The Journal of Physical Chemistry C* **2016**.
- [203] Köntje, C.; Kolb, D. M.; Jerkiewicz, G. *Langmuir* **2013**, *29*(32), 10272–10278.
- [204] Ataka, K.-i.; Osawa, M. *Langmuir* **1998**, *14*(4), 951–959.

- [205] Uchida, H.; Hiei, M.; Watanabe, M. *Journal of Electroanalytical Chemistry* **1998**, 452(1), 97 – 106.
- [206] Magnussen, O. M.; Hagebock, J.; Hotlos, J.; Behm, R. J. *Faraday Discuss.* **1992**, 94, 329–338.
- [207] Mrozek, P.; Han, M.; Sung, Y.-E.; Wieckowski, A. *Surface Science* **1994**, 319(1), 21 – 33.
- [208] Argoubi, W.; Saadaoui, M.; Ben Aoun, S.; Raouafi, N. *Beilstein Journal of Nanotechnology* **2015**, 6, 1840–1852.
- [209] Yoshimoto, S.; Yoshida, M.; Ichi Kobayashi, S.; Nozute, S.; Miyawaki, T.; Hashimoto, Y.; Taniguchi, I. *Journal of Electroanalytical Chemistry* **1999**, 473(12), 85 – 92.
- [210] Hassan, N.; Holze, R. *Russian Journal of Electrochemistry* **2012**, 48(4), 401–411.
- [211] Vericat, C.; Andreasen, G.; Vela, M. E.; Salvarezza, R. C. *The Journal of Physical Chemistry B* **2000**, 104(2), 302–307.